UNIVERSITÉ DU LUXEMBOURG

PhD-FSTM-2022-086
The Faculty of Science, Technology and Medicine

DISSERTATION

Defence held on 27/06/2022 in Luxembourg

to obtain the degree of

DOCTEUR DE L'UNIVERSITÉ DU LUXEMBOURG

EN *PHYSIQUE*

by

Evandro MARTIN LANZONI
Born on 28 June 1988 in Itapira/SP, (Brazil)

GRAIN BOUNDARIES AND POTASSIUM POST-DEPOSITION TREATMENTS IN CHALCOPYRITE SOLAR CELLS

Dissertation defence committee

Dr Alex Redinger, dissertation supervisor
Professor, Université du Luxembourg

Dr Daniel Abou-Ras
Priv. Doz., Helmholtz-Zentrum Berlin Für Materialien und Energie GmbH

Dr Andreas Michels, Chairman
Professor, Université du Luxembourg

Dr Harry Mönig
Priv. Doz., Physikalisches Institut Westfälische Wilhelms-Universität Münster, CeNTech

Dr Susanne Siebentritt, Vice Chairman
Professor, Université du Luxembourg

Contents

List of Figures

List of Tables

Acronyms and Symbols

List of acronyms

CISe $CuInSe_2$

CGSe $CuGaSe_2$

CIGSe $Cu(In,Ga)Se_2$

CIGS $Cu(In,Ga)(S,Se)_2$

CGI Cu/(Ga+In) ratio

Cu-rich Cu/(Ga+In) ratio above 1

Cu-poor Cu/(Ga+In) ratio below 1

GGI Ga/(Ga+In) ratio

GB grain boundary

OVC ordered vacancy compound

PDT post-deposition treatments

PCE power conversion efficiency

FF fill factor

SPM scanning probe microscopy

STM scanning tunneling microscopy

STS scanning tunneling spectroscopy

CITS current imaging tunneling spectroscopy

AFM atomic force microscopy

EFM electrostatic force microscopy

KPFM Kelvin probe force microscopy

AM-KPFM amplitude modulation KPFM

FM-KPFM frequency modulation KPFM

CPD contact potential difference

DOS density of states

1D-WKB 1D model from Wentzel-Kramers-Brillouin

UHV ultra-high vacuum

MOVPE metal-organic vapor phase epitaxy

SEM scanning electron microscopy

EDX energy-dispersive X-ray spectroscopy

EBSD electron backscatter diffraction

CL cathodoluminescence

TEM transmission electron microscopy

XPS X-ray photoelectron spectroscopy

SIMS secondary-ion mass spectrometry

HIM-SIMS helium ion microscope-based secondary-ion mass spectrometry

PL photoluminescence

APT atom probe tomography

FWHM full width at half maximum

RMS root mean square

Abstract

Over the last years, alkali post-deposition treatments (PDT) have been attributed as the main driver for the continuous improvements in the power conversion efficiency (PCE) of Cu(In,Ga)Se_2 (CIGSe) solar cells. All the alkali elements have shown beneficial optoelectronic effects, ranging from sodium to cesium, with many reports linking the improvements to grain boundary (GB) passivation. The most common process for alkali incorporation into the CIGS absorber is based on the thermal evaporation of alkali fluorides in a selenium atmosphere. Besides the demonstrated improvements in performance, disentangling the individual contributions of the PDTs on the GB, surface, and bulk is very challenging because of the many concurring chemical reactions and diffusion processes.

This thesis aims to investigate how pure metallic potassium interacts with CIGSe epitaxially grown on GaAs (100) and multi-crystalline GaAs. Surface sensitive Kelvin probe force microscopy (KPFM) and X-ray photoelectron spectroscopy (XPS) measurements are used to, in-situ, analyze changes in workfunction and compositional changes before and after each deposition step. Inert gas transfer systems and ultra-high vacuum (UHV) are used to keep the pristine surface properties of the CIGSe.

An in-depth understanding of how different KPFM operation modes and environments influence the measured workfunction is discussed in detail in this thesis. It is shown that AM-KPFM, the most common KPFM operation mode, leads to misinterpretations of the measured workfunction at GBs on rough samples. Frequency modulation KPFM (FM-KPFM), on the other hand, turns out to be the most suitable KPFM mode to investigate GB band bending.

Pure metallic potassium evaporation on CIGSe epitaxially grown on GaAs (100) leads to diffusion of K from the surface down to the CIGS/GaAs interface even in the absence of GBs. Evaporation of metallic K is performed using a metallic dispenser, in

which the evaporation rate can be controlled to deposit a few monolayers of K. The deposition is done in UHV, and an annealing step is used to diffuse K from the surface to the bulk.

Pure metallic potassium is also evaporated on CIGSe epitaxially grown on multicrystalline GaAs substrate, where well-defined GBs are present. Negligible workfunction changes at the GB were observed. XPS shows a strong Cu depletion after K deposition followed by annealing. Interestingly, the amount of K on the absorber surface after the K-deposition and subsequent annealing is almost equal to the amount of Cu that diffused into the bulk, suggesting a 1:1 exchange mechanism and no $KInSe_2$ secondary phase.

Introduction

Polycrystalline Cu(In,Ga)(S,Se)$_2$ (CIGS) thin-film solar cells can be considered one of the best alternatives to the well-established silicon-based devices [1], [2]. Typical CIGS solar cells are usually deposited on low-cost glass substrates, flexible polyamide, or steel foils, producing polycrystalline absorbers full of grain boundary (GB)s [2]–[4]. Surprisingly, the power conversion efficiency (PCE) of polycrystalline CIGS solar cells consistently outperformed the single-crystalline counterpart [5]. Many studies attribute it to some intrinsic properties of the GBs in CIGS absorbers that reduce or even neutralize internal barriers [6]–[10]. Additionally, PDT has been identified as the main driver for continuous improvements of the PCE of CIGS solar cells [11]–[17]. However, the number of parameters that are influenced during PDT is complex which makes it hard to disentangle the actual contribution of each involved element and process [16].

This thesis aims to analyze CIGSe absorbers with a reduced number of variables in order to develop a proper understanding of the interaction mechanism of alkali elements with the CIGSe. To do so, CIGSe thin films will be epitaxially grown on different types of GaAs substrates. After that, pure metallic elements will be post-deposited on its surface. The entire process will be done without air exposure to preserve the pristine conditions of the absorbers.

In **Chapter 1**, the reader will find the background information and the state of the art of chalcopyrite CIGS solar cells. A review of the GB properties and some of the most relevant theoretical and experimental literature regarding their consequences on solar cell devices will be presented. In addition, an introduction to the most recent passivation strategies for the GB in CIGS will be discussed. The chapter ends with a review of scanning probe microscopy (SPM) techniques, the primary characterization technique applied throughout this thesis to analyze the GB properties.

In **Chapter 2** the materials and methodologies used in the thesis will be described.

Chapter 3 will dive into the limitations and differences between the two main KPFM operation modes: amplitude modulation KPFM (AM-KPFM) and frequency modulation KPFM (FM-KPFM). Usually, AM-KPFM in the air is the most used operation mode for measuring workfunctions; however, FM-KPFM in UHV is reportedly the most precise. A systematic comparative study will be presented to elucidate the influence of environment and operation conditions on the real workfunction values measured at GBs in solar cells.

In **Chapter 4**, the single-crystalline CISe sample will be studied. It is essential to first understand the electrical properties of the sample in its simplest case, without any GB, alkali elements, or even contamination, before moving moving to a more complex system. This chapter will detail the criteria for choosing the most appropriate and reliable CIGS sample for subsequent investigations.

Chapter 5 discuss the characterization of well-defined GBs employing the CIGSe epitaxially grown on multi-crystalline GaAs substrates. This sample has macroscopic grains, each with a different surface orientation. The target of the experiments in this chapter is to investigate the well-defined GBs of grains with different crystallographic orientations. This approach has several advantages for GB characterization, where individual GBs can be measured multiple times at a micrometer scale before and after PDT.

In **Chapter 6**, the CIGSe samples epitaxially grown on GaAs (100) and multi-crystalline GaAs will be studied after alkali PDT. The most common mechanism for alkali incorporation into the CIGS absorbers is based on the thermal evaporation of alkali fluorides in a selenium atmosphere. This chapter presents how pure metallic potassium element reacts with the CIGSe surface and bulk. First, results in the absence of GBs, the case of the single-crystalline CIGSe grown on GaAs (100), will be shown. The chapter ends with the analysis of K in the presence of GBs, the case of CIGSe epitaxially grown on multi-crystalline GaAs substrate.

Finally, **Chapter 7** summarizes the findings, concludes, and gives a brief outlook.

Chapter 1

Background and state of the art

This chapter provides the background information and the current state of the art about the relevant physical mechanisms and theories describing the grain boundary (GB) and alkali post-deposition treatments (PDT) in polycrystalline chalcopyrite Cu(In,Ga)(S,Se)$_2$ (CIGS) solar cells. Firstly, a historical overview is presented, emphasizing thin-film solar cells. The main physical properties of the CIGS material are then introduced. Afterward, a review of the GB properties with some of the most relevant theoretical and experimental results regarding their consequence on solar cell devices is presented. The passivation strategy of GBs in CIGS based on alkali elements is introduced. The chapter ends with a review of SPM techniques, the primary characterization technique applied in this thesis to access the GB properties.

1.1 The brief historical context of solar cells

The first observation of a photovoltaic effect was made by Becquerel in 1839 [18]. His experiment consisted of a platinum electrode immersed in an electrolyte that produced an electrical current in the presence of light. Nearly forty years later, Adams and Day investigated the first solid-state photovoltaic device, where photocurrent was demonstrated in a sample made of selenium. The next significant step in solar cells came with Fritts, in 1883 [20] by compressing a layer of selenium between two metallic plates. It was the first "thin-film" solar cell in history, even though a commercial application was impossible due to high costs and low efficiency [20]. In the following years, no remarkable developments in the photovoltaic field were achieved, except by

Einstein explaining the quantum theory of the photoelectric effect during his "miraculous year" [21]. Attention returned to the photovoltaic field only a couple of years later, with the observation of the photovoltaic effect in copper — copper oxide thin-film structures [22] and developments of the Schottky barrier devices [23]. Intensified research in selenium, lead sulfide, and thallium sulfide was achieved in the same period [24]. Simultaneously, developments in silicon-based devices were growing, driven by the discovery of well-defined barriers on silicon ingots, which later originated the terminology n-type and p-type and the p-n junction [25]. Shockley published the p-n junction theory in its full detail in 1949 [26], which later, in 1954, led to the development of the single-crystalline silicon solar cell with an efficiency of 6% [27]. In the same year, Reynolds *et al.* [28] reported the photovoltaic effect in cadmium sulfide heterojunction with PCE of about 6% too. Motivated by applications in space, other promising semiconductor materials for solar cell application were also tested. GaAs, for example, first exceeded 6% efficiency in 1956 but rapidly became the most efficient single-junction solar cell [29]. From there on, new materials and technologies appeared, bringing a fast growth of the solar cell PCEs [30].

Over the last years, photovoltaic modules have been considered essential devices for powering satellites in space, but the production cost was the main drawback for terrestrial demands [24]. This is where thin-film solar cells appear, with the premise of using only small portions of expensive semiconductor materials that could reduce production costs. The Cu_xS/CdS can be considered the beginning of the CIGS thin-film solar cells development, where indium was first introduced into the matrix to make it more stable and form the new compound CuInS [3] . Subsequently, gallium and selenium were also incorporated to change the bandgap of the absorber.

Silicon technology has always dominated the shared market of solar cells, representing $> 90\%$ of the global market [31]. On the other hand, thin-film technologies appeared as an alternative to silicon by producing cheap and sufficiently competitive solar cells [32]. However, the current decrease in the price of silicon solar cells requires the thin-film technologies to be cost-effective, have high performance, and be stable over prolonged usage, which still makes the thin-film a worthwhile technology [33]–[35].

1.2 State of the Art of Thin Film Solar Cells

The very basic idea of a solar cell working principle is to convert the sunlight energy into electricity. Visible light can have sufficient energy to remove electrons from the ground state of an atom and bring them to their excited state, but these excited electrons can quickly release their energy going back to the ground state. In the case of semiconductor materials, electrons (for a p-type semiconductor) and holes (for an n-type semiconductor) will be generated upon illumination, provided that the energy of the incident light is equal to or greater than the semiconductor bandgap. If the excess of electrons and holes are not extracted, they will easily recombine; consequently, no current or power will be generated. However, in photovoltaic devices such as CIGS, an asymmetry in the band diagram is created to extract the charge carriers. A p-n junction is commonly used to create asymmetry in CIGS solar cells. The junction can be either a homojunction, where the doping within one material is changed (e.g., Si solar cells), or a heterojunction, where two different semiconductors are combined (e.g., CIGS). In the presence of sunlight, the p-n junction produces electron-hole pairs that, due to the built-in electric field of the junction, pull the excited electrons to an electrode producing a potential difference. Thus, a current is generated by connecting the electrodes to an external circuit [2], [4], [36].

The most efficient solar cells are usually made of expensive and sometimes rare inorganic materials, which turned out to be one of the main drawbacks to the vast implementation of solar cells as energy generation over the last years [24], [30], [34], [37]. That is why thin films are of great interest, where the amount of expensive materials could be reduced. However, a few parameters need to be considered for an efficient single-junction solar cell. Firstly, the semiconductor bandgap needs to be in a specific range, which is well defined by the Shockley-Queisser theory [26], [35]. This theory is based on the balance between absorption and emission of light and describes the maximum achievable PCE for a solar cell according to its bandgap. A semiconductor bandgap is ideal for a single-junction solar cell application if it ranges between $1 - 1.6$ eV [3]. Another critical parameter is related to the optoelectronic properties of the material, which combines high quantum yield for the excited carriers and high solar optical absorption in the wavelength region of $350 - 1000$ nm. Together, these two parameters can describe how much light will be absorbed and how much

of this light will generate carriers in the semiconductor [3]. Long diffusion length and low recombination velocity are also very important since it describes how much of the generated carrier will be collected and transformed in power [3]. Multiple semiconductor materials are generally eligible, but only a few are sufficiently attractive. Thin-film solar cell devices can be manufactured if these constraints are fulfilled, and the primary material is available for thin-film production.

Thin films are materials created by random nucleation and growth processes of individually reacting atomic species on a substrate [38]. As their thickness range varies extensively, from a few nanometers to tens of micrometers, thin films are best defined in terms of production processes rather than by their thickness. Several methods can produce thin-film materials, such as sputtering, evaporation, deposition from the liquid phase, printing, etc [3], [39]. The physical, chemical, structural, and metallurgical properties of thin films depend on many deposition parameters and may also be thickness-dependent [38].

It is well known that silicon is the principal material in the photovoltaic market [31]. The silicon solar cell can be processed whether in crystalline or amorphous form. Silicon has an indirect bandgap (Eg = 1.12 eV), which is close to the ideal for reaching high PCE as described by Shockley [26]. Due to the indirect bandgap, silicon has a relatively low absorption coefficient, which needs relatively thicker material to absorb incoming light, usually between 100 μm to 200 μm. Nonetheless, a significant research and development effort has allowed the development of thin-film solar cells based on crystalline Si, where optical enhancement occupies a substantial part of it [31]. However, their PCEs are still far beyond their single-crystalline counter part [30].

The record PCE for a single-junction solar cell has been achieved using GaAs [30]. GaAs has a direct bandgap with a high optical absorption coefficient, allowing relatively small thickness for the absorber ($\approx 2\,\mu$m) [31]. Although compound materials made of III–V elements of the periodic table (e.g., GaAs, InP, and their derived alloys) are ideal for photovoltaic applications due to their direct bandgap character, they are far too expensive for large-scale commercial applications. Nevertheless, complex multijunction solar cells made of III–V elements are the most efficient and reliable devices for space applications[37]. The high cost of III-V solar cells is due to the precursors and the deposition methods [3]. Additionally, polycrystalline GaAs suffer from high

recombination at GBs, with simulations showing that grain sizes smaller than 50 μm can not deliver efficiencies in the range of 20%, which limits the use of cheap substrates [40], [41].

Hybrid organic-inorganic perovskite solar cells have recently attracted much attention from the photovoltaic research community. With only a few years of research, perovskite devices achieved PCE very close to Si single-crystalline solar cells, currently 25.7% against 26.1% for the silicon counterpart [30]. These thin-film materials have the general composition ABX_3, where A, B, and X are, respectively, the organic cation (commonly methylammonium, CH_3NH_3), the inorganic cation (usually Pb), and the halide (typically I or Br). Perovskite has the advantage of tunable bandgap depending on halide and inorganic cation [31]. The manufacturing costs are low, allowing a solution-based process that can be easily extended to mass production. Despite their excellent performance, perovskite solar cells degrade quickly, within days [31], which is the main drawback for commercial applications. Perovskite material will be used in this thesis as a proof of concept for the GB characterization via SPM.

Together with Perovskite, the chalcogenides compound materials, CdTe and CIGS, are the thin-film solar cell technologies surpassing the barrier of 22% for PCE [32]. Apart from the easy processability and low-cost materials and depositions [1], it is possible to highlight two additional essential properties of chalcogenides compounds: the low recombination activity at the GB and the tunable bandgap [1], [39]. For the former, the external and internal (grain boundaries, interfaces) surfaces are assumed to be well passivated and are characterized due to the low recombination velocity for excess carriers. The low recombination activity at the grain boundaries allows high efficiencies for the solar cell device even when the material is polycrystalline with grain sizes of only a few μm. As the polycrystallinity is not a big issue, it allows multiple substrates to be used (e.g., steel foil, glass), which is also compatible with low-cost deposition techniques, as there is no need for epitaxial growth or high temperatures to obtain large grain sizes. The second property allows tailoring the bandgap; for instance, by substituting Se by S or Ga by In, the number of possible material combinations with a large bandgap range can be achieved. Although commercial activities are still limited, they already indicated competitive payback time compared to the highly mature Si-wafer-based photovoltaic technology [32]. CIGS solar cell absorber

is the primary material to be investigated in this thesis. In the following, a more comprehensive review of the main properties of CIGS material will be presented.

1.3 $Cu(In,Ga)(Se,S)_2$ solar cells

The first synthesis of a CIGS solar cell was a single-crystalline p-type CISe combined with an n-type CdS layer that dates from 1970. This experiment was the first evidence that chalcopyrites could be commercially used as a solar cell device [42]. Since then, several types of research with the goal of improving the optical, electrical, and crystallographical properties of the CIGS was proposed. Attentions to the intermixing of elements in the form of $Cu(In_{1-x}Ga_x)(Se_{1-x}S_x)_2$ (x = 0 to 1), resulted in one of the main characteristics of the CIGS materials, which is the tunable properties. Additionally, the Cu/(Ga+In) ratio (CGI) can also be changed, giving origin to the nomenclature Cu/(Ga+In) ratio below 1 (Cu-poor) or Cu/(Ga+In) ratio above 1 (Cu-rich). Further intermixing is possible, e.g., exchanging Cu with Ag has also been investigated [43].

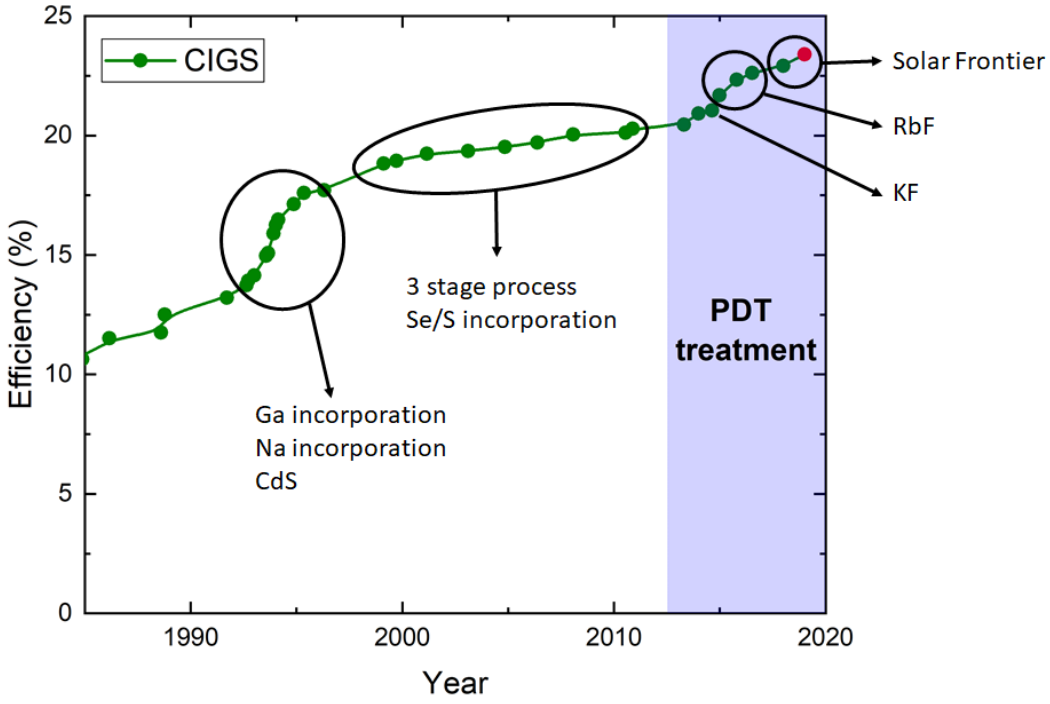

Figure 1.1: CIGS solar cell efficiency over the years.

Regarding its PCE, the CIGS-based solar cells had three highlighted moments in their development. The first one is associated with the Ga and Na incorporation into the absorber. This period is highlighted in Figure 1.1 in the middle of the

90s. From 2000 to 2010, developments in the so-called 3-stage processes also helped improve PCE. Finally, another significant increase came from introducing alkali post-deposition treatments in the last couple of years.

Compounds from chalcopyrites materials usually exhibit tetragonal, with a space group of I-42d [2]. The lattice is a body-centered tetragonal (space group I-42d) with four atoms per unit cell in the form of $CuBC_2$, with B = Ga, In and C = Se, S. Each A and B-atoms are tetrahedrally coordinated to four C-atoms, while each C-atom is tetrahedrally coordinated to two A-atoms and two B-atoms in an ordered manner.

The lattice constant ratio c/a in the chalcopyrite structure generally differs from the ideal value for the tetragonal structure of (c/a = 2). The quantity $[2 - (c/a)]$ measures the tetragonal distortion and is associated with the different strengths of the Cu–Se and the In–Se or Ga–Se bonds [2]. It results in a structure similar to the one shown in Figure 1.2.

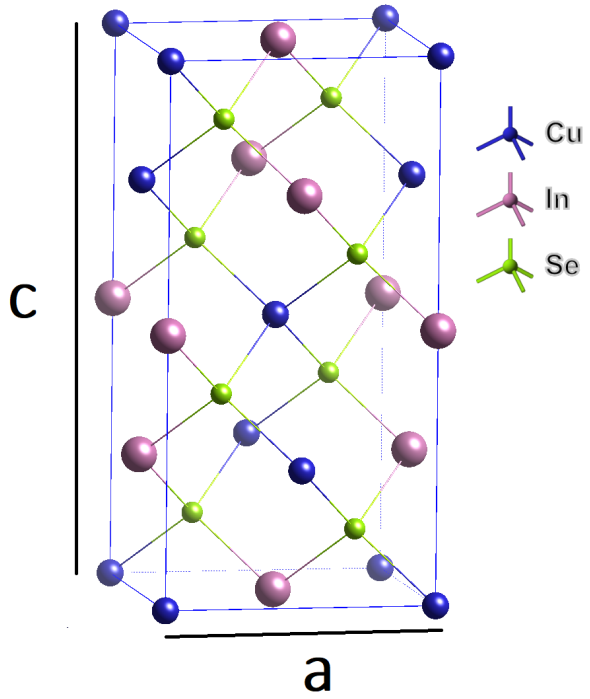

Figure 1.2: Crystal structure of CISe material.

It has been shown via X-ray photoelectron spectroscopy (XPS) that slight Cu-poor $CuInSe_2$ absorbers have a composition close to $CuIn_3Se_5$ on their surface, called the ordered vacancy compound (OVC) phase [44]. Herberholz *et al.* [45] proposed that Cu-poor formation at the surface is due to band bending induced by surface charges that drive Cu into the bulk via electromigration. They also proposed that this deple-

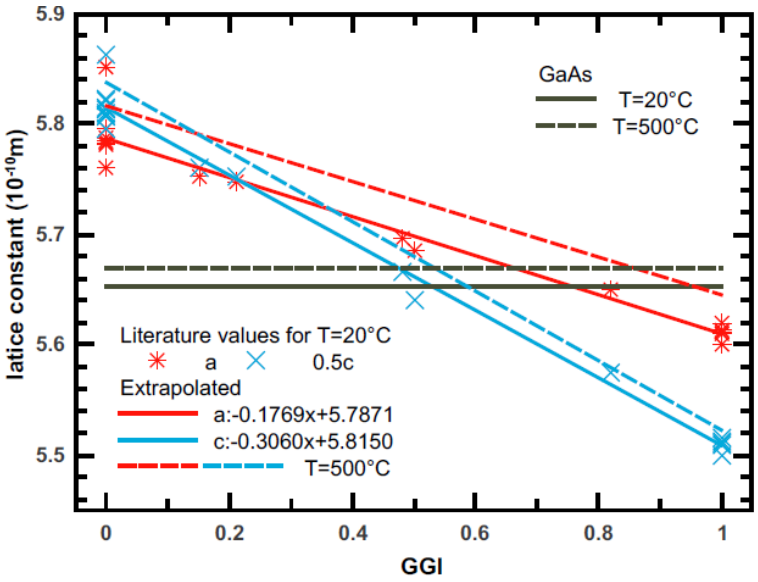

Figure 1.3: Plot showing the linear dependence of the CIGS lattice parameter with respect to the GGI. At CGI close to 0.5, the lattice mismatch is optimal for epitaxial growth. Reprinted from Regesch [49]

tion would self-limit when the composition is that of $CuIn_3Se_5$; otherwise, structural changes would be necessary.

Over the years, CIGS thin-film absorbers have been mainly grown on glass substrates, originating polycrystalline materials with PCE up to 23.4% [46]. Only recently, single-crystalline CIGSe reached PCE of 20% [5]. However, single-crystalline CIGS was extremely important for understanding the elementary material's optoelectronic and crystallographic properties [47], [48]. One way of preparing single-crystalline CIGS is by epitaxially growing on a GaAs substrate. GaAs substrate is usually chosen due to a minor lattice mismatch with CIGS. Regesch [49] observed a linear relation of the lattice parameter of CIGS with respect to the Ga/(Ga+In) ratio (GGI). Figure 1.3 depicts this relation, showing that GGI close to 0.5 should minimize lattice mismatch with GaAs at the growth temperature.

1.4 Grain boundaries in CIGS

It was shown in the previous section that CIGS absorbers are usually grown on glass, and consequently, polycrystalline films with many GBs are formed. For many semiconductor materials, it is well established that GBs are detrimental to the electronic

and optical properties of the studied material [50]–[55]. It happens for the two most efficient materials for single-junction solar cells, Si and GaAs [50], [53], [54]. Consequently, their solar cells' PCE is typically reduced in the presence of GBs [30]. The main reason is the increase in recombination at the GBs [40], [41], [50], [51]. Conversely, polycrystalline CIGS solar cells reached excellent PCEs, currently at 23.4%, while the single-crystalline counterpart only recently reached the 20% [30]. Therefore, it is usually assumed in the community that GBs either exhibit benign electronic properties or even support the charge collection process [10], [56]–[60]. However, despite intensive research on this phenomenon, the optoelectronic properties of GBs in CIGS thin films remain at the heart of controversial discussions [6], [9], [61]–[64]. Indeed, the controversial discussions in the literature underline the importance of a better understanding of the electronic activity of GBs in CIGS.

The primary consequence of a GB in a crystalline structure is the interruption of its crystalline periodicity. It is well-established that such interruption results in dangling or strained bonds that often lead to energy states in the bandgap with a possible appearance of charges at the GBs [9]. However, in the case of Cu-chalcopyrite-based solar cells, the large variety of preparation methods and the wide range of possible alloy compositions lead to very different grain sizes and surface morphologies.

A few theoretical models are proposed in the literature to explain the behavior of the GB to the electric properties of the CIGS absorber. Rau *et al.* [9] reviewed four available simulation approaches and tried correlating them with some available experimental data. The analyzed models are:

Crystallography: This model assumes that most of the GBs present in the CIGS absorbers arise from twin boundaries. In twin boundaries, no strained or dangling bonds are formed, which does not produce a potential barrier at the GB [58], [65].

Intrinsic passivation: This model assumes that no electronic defects are formed by relaxing the defect structures. It is the case for all kinds of GBs, even the ones with a high density of structural defects. [66]

Extrinsic GB passivation: The beneficial effect of post-deposition treatments are considered in this model. It assumes that the passivation of electrically active GBs has beneficial effects on device performance. Such passivation strategies range from oxygenation of GBs to post-deposition treatments of alkali elements. [11], [67], [68],

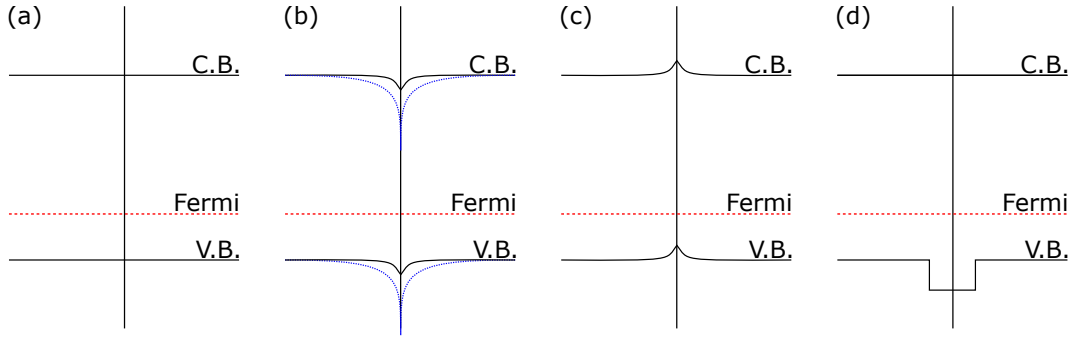

Figure 1.4: Band diagram at GB: (a) no barrier, (b) downward band bending, (c) upward band bending (d) lowering the valence band.

Band Structure: This model assumes a neutral barrier at the GBs, resulting from a Cu-poor composition of the region adjacent to the GB [6], [7], which would lower the valence band locally.

In the end, these theories would lead to a change in the band diagram at the GB, as represented in Figure 1.4.

Figure 1.4 (a) shows the band diagram at the GB for the condition where no barrier is assumed. It would be the case for the twin boundaries, where no dangling or strained bonds are assumed. Figure 1.4 (b) represents the downward band bending at the GB. One could argue that downward band bending at GBs helps the current collection by reducing recombination since only the majority carriers would be repelled [39], with the minority carrier being attracted and guided through this GB channel until the junction. However, numerical simulations showed that a beneficial effect on the device performance is expected only when a type inversion happens. It requires a significant band bending as shown in Figure 1.4 (b) (blue line), and considerable open-circuit voltage losses in the devices are expected [9], [59], [69]. Taretto *et al.* [69] also showed that upward band bending (Figure 1.4 (c)) would, in certain situations, enhances the short circuit current, but no beneficial effect on the cell efficiency was observed. Lastly, the case of valence offset (Figure 1.4 (d)) predicts that the offset barrier could potentially reduce the GB recombination by impeding holes from reaching the GBs. However, it requires a valence band offset region of at least 3 nm wide [9].

In summary, simulations suggest that charges at the GBs reduce the solar cell performance mainly because of losses in open-circuit voltage (V_{OC}) accompanied by a reduction in fill factor (FF) [9], [69]. A few conditions could occasionally reduce the

recombination at GBs, but none of the simulations suggests a beneficial effect of the GBs in CIGS absorbers.

Along with simulations, a few experimental techniques with high spatial resolution have been used frequently by the community to measure the influence of GBs on solar cell performance locally. Examples of techniques applied to this field are scanning electron microscopy (SEM), transmission electron microscopy (TEM) [70]–[73], atom probe tomography (APT) [74]–[76], photoluminescence (PL) [77], [78], and scanning probe microscopy (SPM) [79], [80], such as scanning near-field optical microscopy (SNOM) [81], scanning tunneling microscopy (STM) [82], [83], and Kelvin probe force microscopy (KPFM) [60], [84]–[86]. Highlighted results from literature using the abovementioned techniques on GBs will be shown.

Abou-Ras *et al.* [8] combined several electron microscopy techniques to investigate the GB types in CISe thin films. The authors showed that the density of non-radiative recombination at non-twin GBs is much larger than the one found at twin GBs. Figure 1.5 shows the cathodoluminescence (CL) and EBSD maps acquired at the same region of the CISe absorber. From EBSD, they could identify the twin boundaries, marked in red on the EBSD map, and correlate them with the CL contrast. They also observed via TEM that the mean inner potential wells are lower for the twin boundaries, and they correlated it to a possible reduction in the recombination velocity at GB, which is less pronounced in the twin boundaries.

APT is usually used to quantify the elements at the GB. Schwarz *et al.* [75] showed the APT measurements on $CuInS_2$ absorbers, depicted in Figure 1.6. In this experiment, different GB types were investigated, called here random boundaries (RHAGBs), and two twin boundaries, $\Sigma 9$ and $\Sigma 3$. A twin boundary is a particular class of boundary where the crystallographic orientation on one side mirrors the other side of the crystal, with the Σ number designating the angle formed between them. Lower values of Σ mean that small misorientations are happening, also called "small-angle twin boundaries", with $\Sigma 1$ denoted as perfect crystal or no boundary at all. Larger values of Σ denote a higher angle between the two sides of the crystal. Schwarz *et al.* observed chemical fluctuations of the matrix elements at the RHAGBs and $\Sigma 9$ boundaries, followed by co-segregation of impurities. Their Cu-poor $CuInS_2$ samples exhibited Cu depletion and In enrichment as well as segregation of Na, K, and O at the RHAGBs

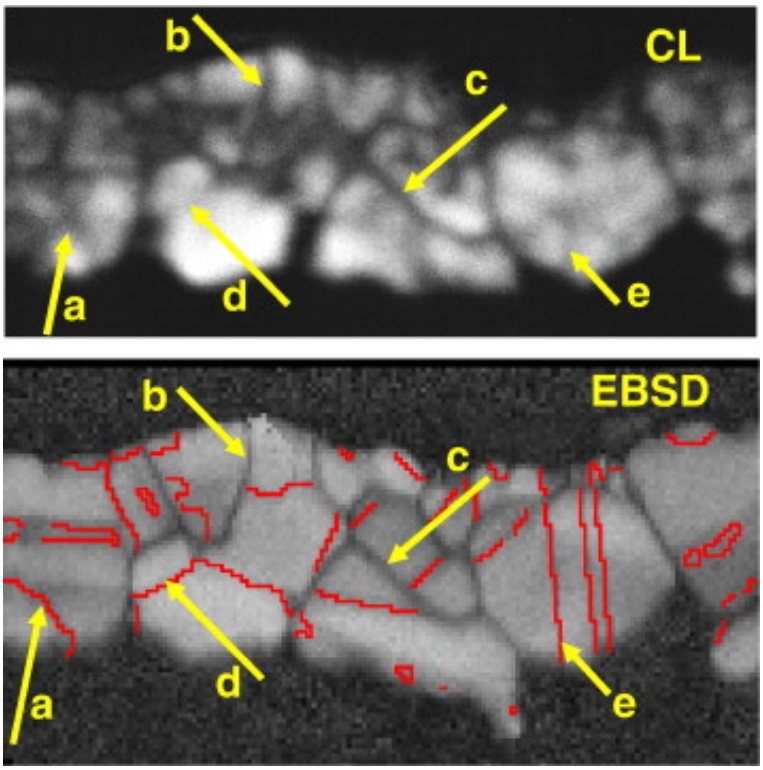

Figure 1.5: Electron microscopy techniques applied to GBs. CL and EBSD maps acquired in the same spot of a CISe sample. Twin boundaries are marked in red in the EBSD map showing a higher density of non-radiative recombination at non-twin boundaries than the one found in the twin boundaries. Figure reprinted from Abou-Ras *et al.*, ©(2009) Thin Solid Films - Elsevier

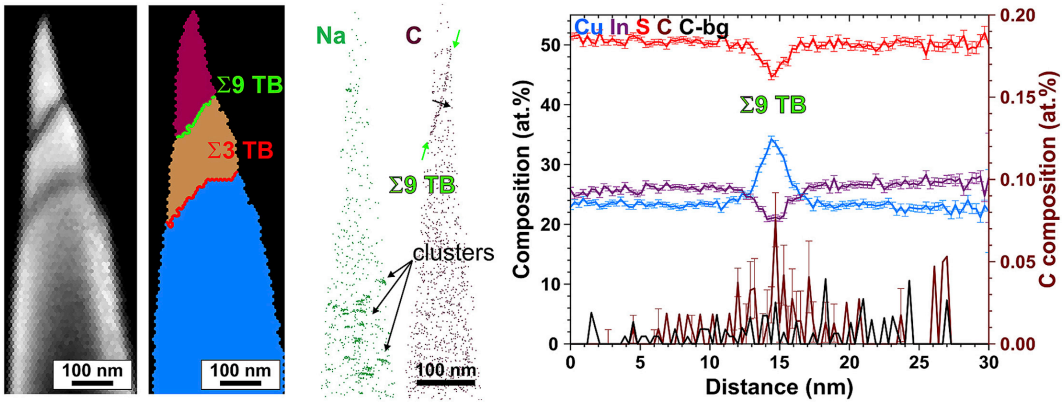

Figure 1.6: Typical APT applied to GBs. Cu enrichment of the Σ9 twin boundary on Cu-rich $CuInS_2$ sample. Figure reprinted from Schwarz *et al.*, ©(2020) Nano Energy - Elsevier

and Σ9 boundaries. In contrast, their Cu-rich $CuInS_2$ samples showed Cu enrichment with In and S depletion as well as segregation of Na and C. All the investigated Σ3 did not show any fluctuation in the elemental composition. APT data from Keller *et al.* [76] also showed that, within the same absorber, the Cu depletion or enrichment could occur depending on the location of the GB, if closer or far away from the back contact.

Both APT and electron microscopy techniques showed that different morphologies and the consequent appearance of different types of GBs could be observed in the CIGS materials. They also showed that the composition might vary at the GBs with the appearance of distinct electrical properties depending on the GB type and absorber compositions.

Combining different SPM techniques is also a powerful way to access the electrical properties of the GBs. Mönig *et al.* [64] used STM to access the local density of states (DOS) at the GBs of a KCN etched CIGSe absorber [64]. In STM, the DOS can be written as $\approx dI/dU$ when U is in the close vicinity of the Fermi energy level.

Figure 1.7 shows the dI/dU spectra acquired on the grain and at the GB and the respective numerically calculated dI/dU spectra. Figure 1.7 (a) shows the average dI/dU spectra recorded on the grain (gray dotted curve), adjacent to GB (red dashed curve), and at GB (blue solid curve). The physical locations from where the dI/dU were collected are marked in the inset current imaging tunneling spectroscopy (CITS) map. Figure 1.7 (b) shows the schematic energy level diagram at the GB with three

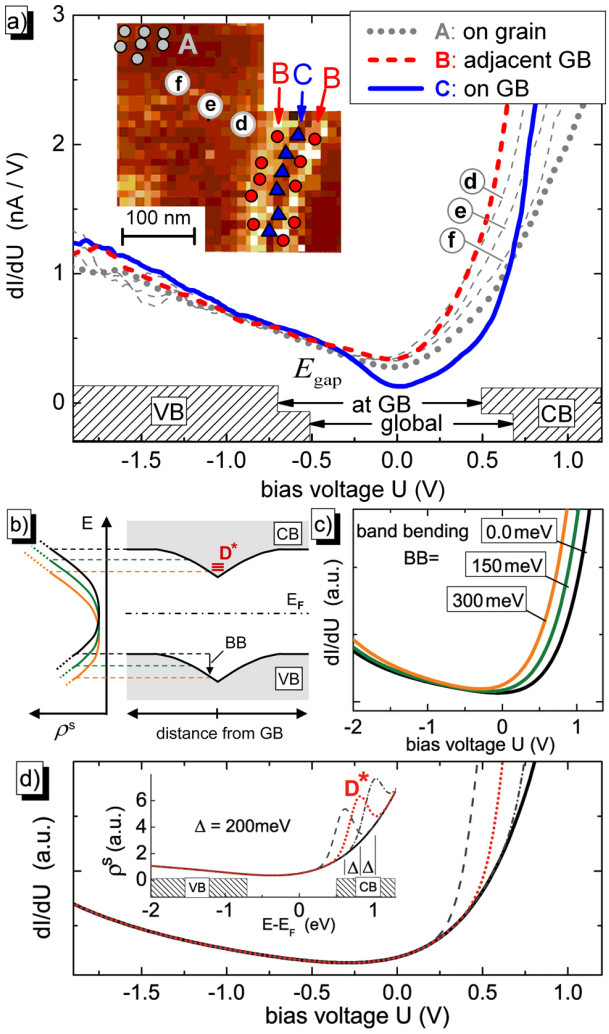

Figure 1.7: STM applied to GB. Typical dI/dU information from GBs in CIGSe samples. (a) shows the average dI/dU spectra recorded on the grain (gray dotted curve), adjacent to GB (red dashed curve), and at the GB (blue solid curve). The inset CITS map depicts the locations from where the dI/dU were collected. Figure 1.7 (b) shows the schematic energy level diagram at the GB with the dI/dU spectra collected in the regions d, e, and f. (c) Numerical calculation of the dI/dU spectra evidencing a band bending caused by defect level D* at the GB. (d) Numerically calculated dI/dU spectra with and without defect level D*. Figure reprinted from Mönig *et al.*, ©(2010) Physical Review Letters - APS [64]

dI/dU spectra collected in the regions d, e, and f. They showed that a defect level D* at the GB could be well justified by the observed band bending in the dI/dU spectra. A numerical calculation of the dI/dU spectra for band bending = 0, 150, and 300 meV was done to prove their assumption. Figure 1.7 (c) shows the shift in the calculated dI/dU spectra for positive bias voltages, which is attributed to the sample workfunction dependence in the tunneling current. They concluded that a downward band bending is present at the GB of their CIGSe absorber. Figure 1.7 (d) shows the numerical calculations of the dI/dU with and without a defect level D*. The authors proposed that a high density of defect levels resonate with the bottom end of the conduction band, which does not extend into the bandgap.

Along with STM, KPFM (sometimes called SKFM or KFM) is also commonly applied to investigate GB band bending. In principle, the GB band bending can be directly accessed via KPFM by measuring the change in surface potential between the GB and the surrounding. That is because the acquired surface potential map can be immediately converted into a workfunction map (difference between the vacuum level and Fermi level). The complete theory of the KPFM will be shown in section 1.7.

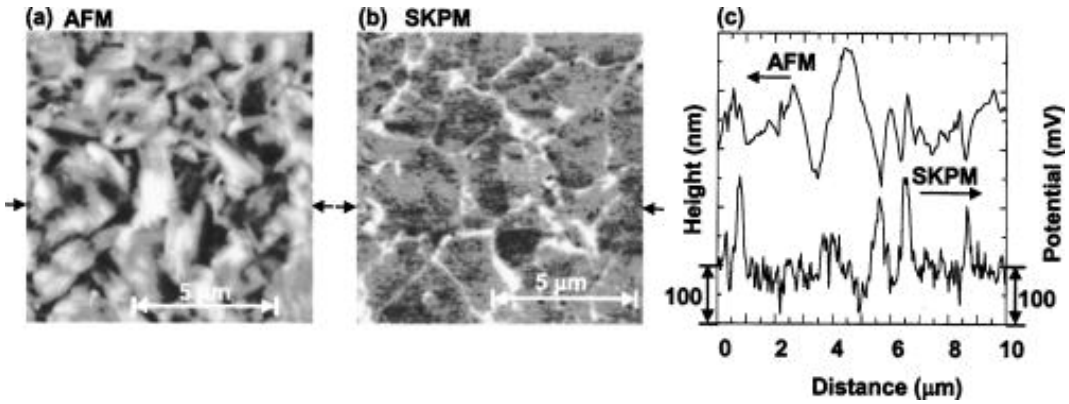

Figure 1.8: Typical KPFM applied to GB of polycrystalline CIGS. (a) topography and (b) surface potential maps acquired simultaneously at the sample surface. (c) shows how topography and surface potential changes correlate at GB. Figure reprinted from Jiang *et al.*, ©(2004) Applied Physics Letters - AIP [87]

Figure 1.8 shows a typical KPFM image, where a workfunction contrast is observed right at the GB. Figure 1.8 (a) shows the topographic image and (b) the surface potential map (written SKPM in the figure). In the KPFM, the topography and the surface potential maps are usually acquired simultaneously, and a physical correlation

of the images can be easily drawn. By extracting line profiles from both images (Figure 1.8 (c)), the authors showed that changes in the surface potential are directly linked to the GB region. Jiang *et al.* proposed the existence of a local built-in potential at the GB with positive charges, which causes a downward band bending.

Well-defined GBs from epitaxially grown ($CuGaSe_2$ (CGSe)) were also investigated via KPFM. Siebentritt *et al.* [58] investigated the $\Sigma 3$ twin boundary of $CuGaSe_2$ that was epitaxially grown on GaAs twin wafer. Figure 1.9 (a) depicts the topography and (b) the workfunction maps acquired at the GB region. The topography shows some trenches at the sample surface on the left-hand side of the image, which is attributed to the preferential growth direction of GaAs (100). On the right-hand side, a formation of the (112) facet is observed. Figure 1.9 (b) shows a slight difference in workfunction close to the GB region but no dip or dump higher than the noise level of the KPFM setup ($\approx 5\,mV$) was observed. Therefore, the authors concluded that a neutral barrier is formed at $\Sigma 3$ twin boundaries in $CuGaSe_2$.

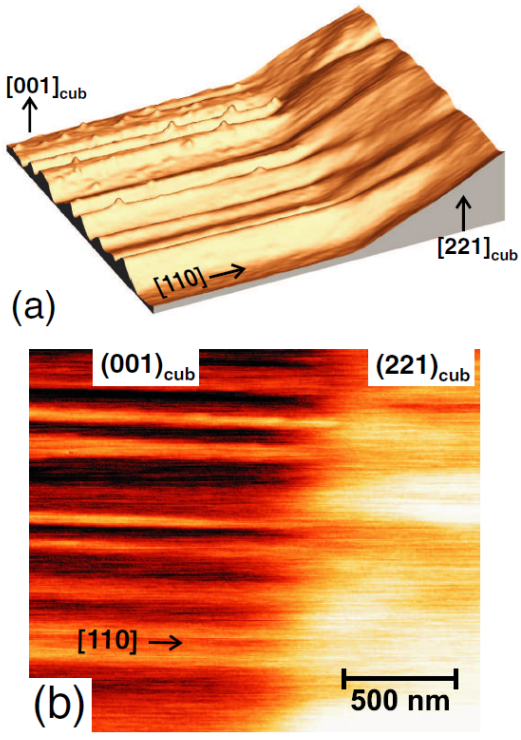

Figure 1.9: KPFM applied to twin boundary $\Sigma 3$. (a) topography and (b) surface potential maps of a CIGS absorber. Figure reprinted from Siebentritt *et al.*, ©(2006) Physical Review Letters - APS [58]

1.5 Alkali post-deposition treatments

Simulations and experimental results suggest that defects and compositional changes at the GB induce charge accumulation at the GBs, which could be harmful, or in the best-case scenario, neutral to the CIGS solar cell device performance. Over the last years, alkali PDTs have been identified as the main driver for the continuous improvements in the PCE of CIGS solar cells by passivating the GBs [11], [88]–[90]. Ranging from sodium to cesium, all the alkali elements have shown beneficial optoelectronic effects [15], [17], [46], [91]. In the following, an overview of the main observations in this field will be presented.

The alkali metals are the six chemical elements from Group 1 (Ia) of the periodic table, namely, Li, Na, K, Rb, Cs, and Fr. Sodium and potassium represent 2.6 and 2.4 percent of Earth's crust, making them the sixth and seventh-most abundant elements in the Earth's crust, respectively. Alkali metals are usually bonded to other elements in nature because they are very reactive. Additionally, they have high thermal and electrical conductivity, ductility, and malleability. One of the main electronic characteristics of the alkali atoms is the single electron in its outermost shell. Because of it, their atomic radius is usually very large, with only one weakly bound electron in the outer s orbital. As a result, the alkali metals tend to form positive ions (cations) when they react with nonmetals [92].

The first notable results of improvement in the electrical performance of CIGS in the presence of alkali elements were made by Stolt *et al.* and Holz *et al.* [93], [94]. Stolt *et al.* [93] compared the growth of CIGS absorbers on soda-lime glass (SLG), borosilicate, sapphire, and alumina substrates. They observed that the CIGS solar cells grown on soda-lime glass had a better device performance. They linked it to a higher concentration of Na inside the bulk and a stronger (112) texturing [93]. At that time, they could not disentangle which effect was responsible for the solar cell improvement. Holz *et al.* [94], on the other hand, showed that low doses of Na increased the electrical conductivity of the CIGS device. Several studies confirmed that the incorporation of Na into the CIGS absorber improved the device performance, and some theories to explain this observation were proposed [11], [67], [95]–[97]. For example, Heske *et al.* [96] showed the formation of two different species on the surface of the CIGSe grown on soda-lime glass. These two species reduced the presence of Se

native oxide on the surface, induced a band bending, and reduced the surface dipole. Kronik *et al.* [67] showed the chemical effects of oxygenation of Cu(In,Ga)Se2 (CIGS), which involved passivation of Se deficiencies and Cu depletion. The authors showed that Na promotes oxygenation of the CIGSe, which promotes the creation of Cd-Cu interface donors and the possible removal of O-Se interface acceptors.

After this first boom of good results related to sodium, new alkali elements were also incorporated into the CIGS solar cells. The terminology adopted by Siebentritt *et al.* [17] will be used here, in which "light alkalis" are referred to as the elements Li and Na, and "heavy alkalis" to the elements K, Rb, and Cs.

Potassium fluoride (KF) was the first heavy alkali element incorporated into CIGS [12], [13]. Back there, the incorporation of alkali was already a synonym for high V_{OC} and FF of the device [14], [98], [99]. It also became clear that the CIGSe surface composition changes due to PDTs, with a pronounced Cu-depletion and suggesting an ion-exchange mechanism between K (from PDT) and Na (from the substrate) [12]. Furthermore, a high bandgap secondary phase was theoretically predicted [100] and sometimes observed at the absorber surface [101]–[103]. One important consequence of changing the surface composition is the possibility of reducing the CdS buffer layer thickness, which reduces parasitic absorption, improving the short-circuit current density.

With new incorporation methods being reported, many contradictions in the effect of the alkali elements also appeared. The review paper from Muzzillo [16] from 2017 summarized quite well all these contradictions. One of them is related to the chemistry at the surface. Chirilă *et al.* [12] showed that the KF PDT led to a Cu- and Ga-depletion at the surface. Indeed, several other studies corroborate their observations of Ga depletion [102], [104]–[107] and Cu depletion [14], [98], [99], [108]–[110]. Contrary, there are data in the literature showing no Cu depletion at the surface [13], [14], [111], [112]. Similarly, the formation of K-In-Ga-Se [104], [113], K-In-Se [43], [98], [102], [105], [112], In-Se [105], [112], elemental Se [112] is highly debated. More recently, Siebentritt *et al.* [17] showed that independent of the absorber or the used alkali material, the chemical changes on the surface appear to be similar, while the electronic properties differ. The authors proposed that changes at the surface are not the only effect of the alkali PDT, whereas bulk recombination due to PDT should have an even stronger

contribution to the device performance.

Things get even more complicated when discussing the effect of alkali elements in CIGS absorbers in the presence of GBs. As previously shown, many open questions and discrepancies in the literature regarding the GB only are still unsolved. Nevertheless, some concepts are widely accepted in the community, such as the segregation of alkali elements at the GBs.

Figure 1.10 depicts an exemplary APT measurement, showing the accumulation of alkalis at the GB of the CIGSe absorber. Siebentritt *et al.* [17] investigated changes in the GBs composition with (RbF) and without alkali PDTs. The CIGSe sample without alkali PDT had Na and K inside the bulk.

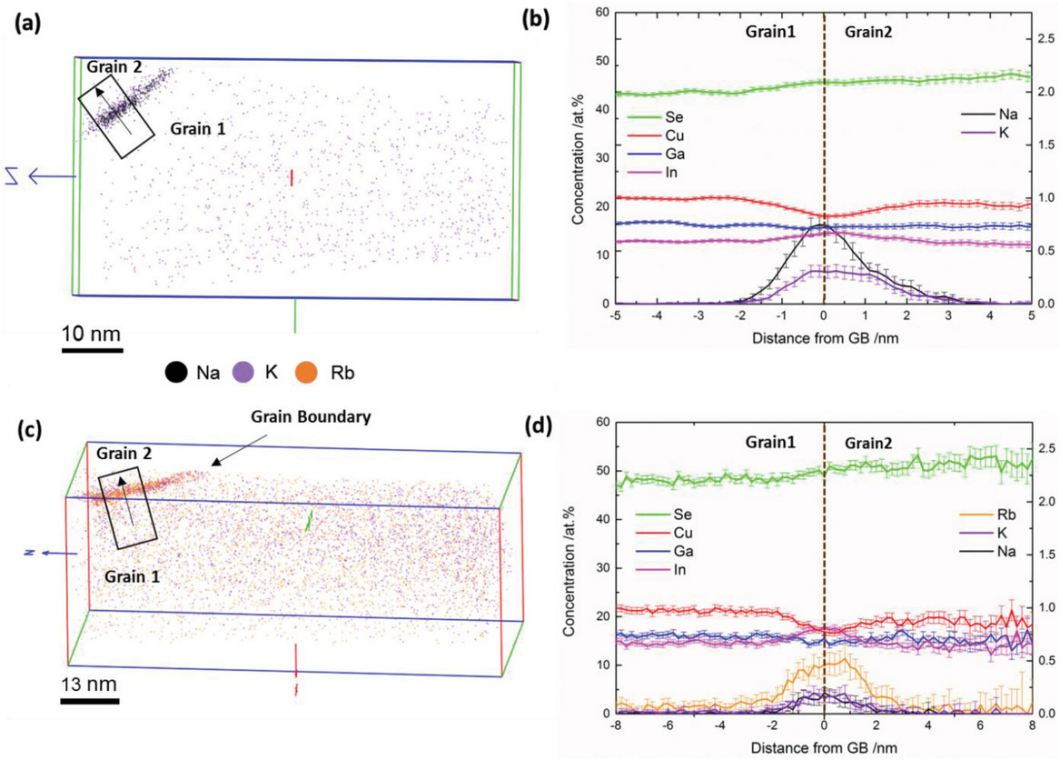

Figure 1.10: APT of the alkali-treated CIGS sample. Typical alkali accumulation at the GB of CIGS absorbers. Figure reprinted from Siebentritt *et al.*, ©(2020) Advanced Energy Materials - Wiley-VCH GmbH.

Figure 1.10 depicts the 3D reconstruction of both samples (a-c) and their equivalent relative concentration across the GB region. Na was found in higher concentrations than K at the GB in the sample without PDT (Figure 1.10 (a,b)). Interestingly, after the RbF PDT, larger amounts of Rb were found at the GB, with a significant increase in the Na content inside the grain interior. They also showed, in both cases, a Cu

depletion and In enrichment at the GB. A similar accumulation of alkali elements at grain boundaries was also observed via TEM and X-ray fluorescence investigations for similar absorbers [114], [115].

KPFM is constantly used to check the GB passivation after alkali treatments. A typical KPFM image showing the GBs of a CIGS absorber after KF PDT is presented in Figure 1.11. Figure 1.11 (a) and (c) depict the surface potential maps of the sample with and without KF PDT, while Figure 1.11 (b) and (d) depict the simultaneously acquired topography maps.

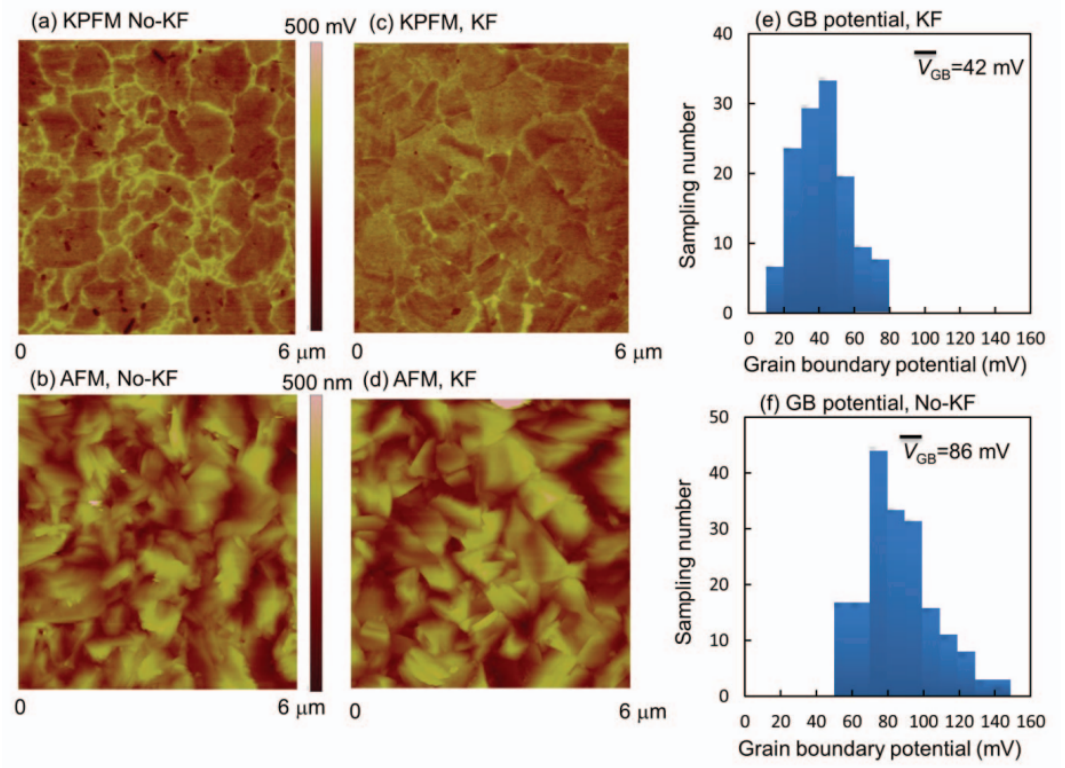

Figure 1.11: KPFM applied to GB. Typical KPFM image from GB characterization of alkali-treated CIGSe sample. (a, b) surface potential and topography maps of the non-KF-treated sample. (c,d) surface potential and topography maps of the KF-treated sample. (e,f) surface potential distribution of the non-KF- and KF-treated samples. Figure reprinted from Jiang *et al.*, ©(2016) Proceedings of 43rd Photovoltaic Specialists Conference - PVSC - IEEE.

The sample not treated with KF showed a stronger surface potential contrast at the GB, whereas a massive reduction is seen for the KF-treated sample. The histograms (Figure 1.11 (e) and (f)) show that the average workfunction reduction was in the

order of 44 mV, which was attributed to the passivation of the GBs.

Indeed, combining the accumulation of alkalis at the GB, local changes in work-function, and higher V_{OC} of the device, suggest an efficient GB passivation on CIGSe absorbers. But recently, Abou-Ras *et al.* [117] questioned the passivation effect by showing no improvements in the GB recombination velocities. Ramírez *et al.* [118] also showed an astonishing result when they presented an improved quasi-Fermi level splitting of up to 30 meV for KF PDT on CIGSe single crystals absorbers (e.g., no grain boundaries). Their results showed a strong dependence on the Cu-content. The improvements in quasi-Fermi level splitting after PDTs were attributed to changes in absorber doping.

Similar to the GB discussion, the interplay between the alkali metals and the polycrystalline CIGS absorbers is extremely complex, and many different observations were reported. The fact is, besides all the discrepancies in the literature data, the CIGS solar cells gained another upgrade in efficiency after introducing the alkali elements, as shown in Figure 1.1. However, a better understanding of the real effect of alkali elements on CIGSe materials is still needed, which could improve the efficiency of CIGS solar cells even further.

1.6 Open questions that will be answered in this thesis

This chapter presented an overview of some published results relevant to this thesis. It was shown that many efforts in the CIGS thin-film were made, highlighting this technology as one of the most important alternatives to the well-established silicon solar cells. However, besides the enormous developments over the years of research, many contradictions related to the nanoscale properties of this material after alkali deposition are still a drawback for further improvements. The reason is the multitude of parameters that can change when adding alkali elements into an already complex material such as CIGS. In this thesis, new insights on how pure metallic potassium interacts with CIGSe epitaxially grown on GaAs substrates will be presented. The goal of using a presumed "simplified" model is to answer the following open questions that are still not clarified in the community.

- Is KPFM a proper technique to study GBs?
- Are downward or upward band bending detectable via KPFM?
- Is it possible to simplify the alkali deposition in order to analyze the contribution of pure alkali elements into the CIGS absorber?
- What are the mechanisms for the alkali diffusion into the CIGSe absorber?
- Does the alkali material diffuse into the grain interior?
- What is the impact of pure alkali elements on the GBs of CIGSe absorbers?

At this point, the reader might ask why the first two open questions are explicitly related to the KPFM techniques. The reason is that one of the starting points for all the discussions related to GB band bending in polycrystalline solar cells is related to KPFM data. Although KPFM is a very established characterization technique, a few limitations are not considered when measuring the GBs. In this thesis, a methodology for proper KPFM characterization at GB will be present in Chapter 3. Therefore, the background theory related to the SPM techniques will be presented to introduce the reader to the topic.

1.7 Scanning Probe Microscopy (SPM)

Scanning probe microscopy (SPM) is a family of versatile techniques to image a sample surface with nanometer lateral resolution. The development of SPM dates back to 1981, when Binnig *et al.* [119] observed the tunneling effect through a controllable vacuum gap for the first time. For this experiment, they used a sharp tungsten (W) probe mounted in a very precise piezoelectric z stage. They measured the tunneling current, while keeping the distance between the probe and a platinum sample constant. In 1982, the same authors combined the tunneling effect with piezoelectric materials' precise movement in the x, y, and z directions to give birth to scanning tunneling microscopy (STM) [120]. It was the first time in history that individual atoms were measured in real space. This experiment awarded Binnig and Rohrer the Nobel Prize in physics in 1986.

STM is, until nowadays, one of the most powerful nanoscale imaging techniques for (semi-)conductive materials or very thin insulator materials. However, it has some limitations, such as; the need for special preparation for UHV, the tunneling current requires an electrical circuit between probe and sample, and insulators with more than a few nm thick cannot be measured. In 1985, Binnig *et al.* [121] proposed atomic force microscopy (AFM) to overcome these issues. Their solution consisted of using an STM as a probe to detect movements of a metallic cantilever placed in close vicinity to a sample surface. The idea was that the interatomic forces between the metallic cantilever and the sample surface would bend the cantilever and consequently change the measured tunneling current. This experiment allowed forces in the order of 10^{-18} N to be measured on insulator materials under ambient conditions [121]. The development of AFM triggered a series of new opportunities for measuring different kinds of physical properties, such as electric [122]–[125], magnetic [126]–[128], and optic [129]. Nowadays, more than 30 SPM-based techniques are commercially available, which goes far beyond only the topography acquisition of a specific material. In the following, the elementary theoretical background of the main SPM-based techniques used in this project will be presented.

1.7.1 Scanning Tunneling Microscopy (STM)

The basic principle of all SPM-based techniques consists of placing a sharp probe near or even in contact with the sample surface and measuring some physical properties. In the case of STM, the measured property is the tunneling current.

In classical physics, considering an electron with energy E inside a potential barrier $U(z)$, this electron will never escape if $E < U(z)$. However, there is a non-zero probability for this electron to go through the barrier in quantum physics; it is called the "tunnel effect." As demonstrated by Davisson *et al.*, in 1927 [130], electrons can be described as waves, confirming the wave-particle duality theory from De Broglie. By describing the electron as a wavefunction $\psi(z)$, it needs to satisfy Schrödinger's equation.

$$-\frac{\hbar^2}{2m}\frac{d^2}{dz^2}\psi(z) + U(z)\psi(z) = E\psi(z) \tag{1.1}$$

Solving it for the classically allowed region, meaning $E > U(z)$, results in the fol-

lowing solution.

$$\psi(z) = \psi(0)e^{\pm i\kappa z} \tag{1.2}$$

where the wave vector κ is defined as:

$$\kappa = \frac{\sqrt{2m(E-U)}}{\hbar} \tag{1.3}$$

It shows that in the classically allowed region ($E > U(z)$), the electron can either move with constant momentum $p = \hbar k$ or move with constant velocity $v = p/m$.

Solving Equation 1.1 for the classically forbidden region ($E < U(z)$) results in the following solution:

$$\psi(z) = \psi(0)e^{-\kappa z} \tag{1.4}$$

with the wave vector,

$$\kappa = \frac{\sqrt{2m(U-E)}}{\hbar} \tag{1.5}$$

which gives the probability density to find the electron in the classically forbidden region $|\psi(0)|^2 e^{-2kz} \neq 0$. It is illustrated in Figure 1.12 (a), where $\psi(z)$ propagates from one metal to the other through the vacuum barrier U.

Assuming the case of a metallic probe and sample separated by a distance z under vacuum, and defining the vacuum barrier as the energy required to remove an electron from the sample surface and place it in the vacuum (called the workfunction Φ). For simplicity, it will also be assumed that the sample's and probe's workfunction are equal, with Fermi and vacuum levels aligned. When the probe is near the sample surface, electrons from one side could tunnel to the other side and vice versa. However, as long as the probe and sample are in the same electrical potential, in other words, their Fermi levels are aligned, even if the electrons can tunnel, they will not do because there are no empty states on either side. By applying a bias voltage V, there will be a change in the population of the energy level near the Fermi level, and consequently, it will induce a constant tunneling current. Applying a positive bias to the probe will lead to electrons tunneling from the sample to the probe, as seen in Figure 1.12 (b). While negative bias will promote electrons to tunnel from the probe to the sample.

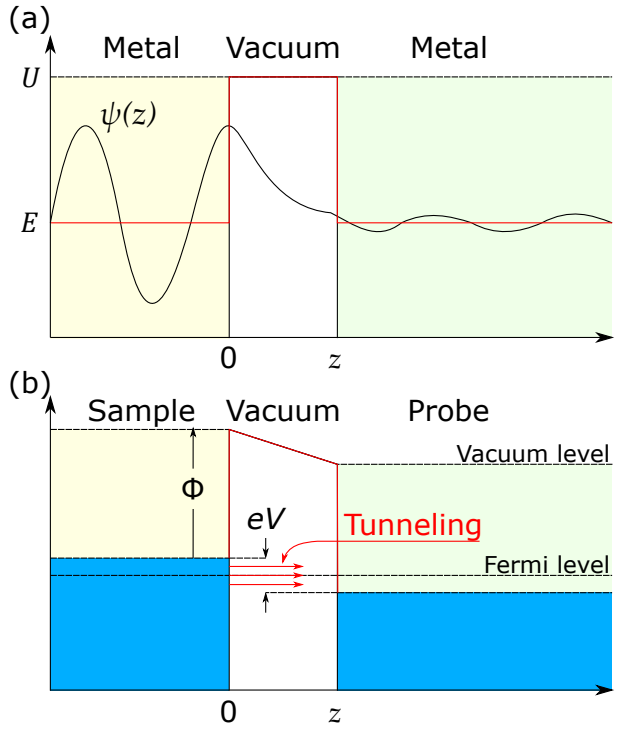

Figure 1.12: Tunneling effect and STM principles: (a) Metal-Vacuum-Metal model that there is a probability of the wavefunction to tunnel through a vacuum gap. (b) Sample-Vacuum-probe model for the STM working principle. Electrons can tunnel through the vacuum gap if an energy eV is given to the system.

This condition makes the bias voltage much smaller than the workfunction ($eV \ll \Phi$), meaning $E \approx 0$. It simplifies Equation 1.5 as follows,

$$\kappa' = \frac{\sqrt{2m\Phi}}{\hbar} \tag{1.6}$$

Thus, it defines an essential parameter for the STM, called Transmission coefficient T. It is the ratio of the tunneling current at the probe/sample distance z divided by the tunneling current at the probe/sample distance $z = 0$.

$$T = \frac{I(z)}{I(0)} = \frac{|\psi(z)|^2}{|\psi(0)|^2} = e^{-2\kappa' z} \tag{1.7}$$

Solving Equation 1.6 numerically by using 5 eV for the workfunction results in a decay constant $\kappa' \approx 11.4nm^{-1}$. Substituting κ' into Equation 1.7, the relation between distance and tunneling current appears. A change of 0.1 nm in the probe/sample distance leads to one order of magnitude change in the tunneling current. It results in the control mechanism for the topography measurements in STM. If the probe is

approached against the sample surface and scans it by keeping the current constant, the surface topography can be acquired by moving the probe up and down. This scanning method is called constant current. On the other way around, if the probe and sample positions are kept constant and the current is monitored, the method receives the name of constant height. These are the two main modes for topography acquisition during STM, which is very sensitive to the last atom in the probe apex interacting with the atoms at the sample surface.

In a general theoretical model, the tunneling current in STM is given by

$$I = 32\pi^3\hbar^{-1}e^2V\Psi^2\rho_p(E_F)R^2\kappa^{-4}e^{2\kappa R}\sum|\psi_s(z)|^2\delta(E_s - E_F) \tag{1.8}$$

where $\Psi = \Psi_p + \Psi_s$ is the average workfunction of probe and sample, ρ_p is the density of states (DOS) of the probe at the Fermi level, and $\psi_s(z)$ is the local DOS of the sample surface at a distance z. This model was proposed by Tersoff *et al.* [131] and uses the planar tunneling junction problem treated by Bardeen [132], but now assumes a flat surface and a spherical probe apex, temperature at zero Kelvin, and very low gap voltages between probe and sample (10 mV) [133].

Another model, which is most widely used in simple models of STM, is the one-dimensional 1D model from Wentzel-Kramers-Brillouin (1D-WKB) approximation. Here the tunneling current can be expressed as

$$I(z,V) \cong \frac{A\pi e\hbar^3}{2m^2}\int_0^{eV} T(z,\Phi_{s,p},V,E)\rho_p(E-eV)dE \tag{1.9}$$

which does not depend on $\psi_s(z)$ anymore, differently from the Tersoff and Hamann [131] approach. Instead, it depends on the DOS of probe and sample, ρ_p and ρ_s respectively, and the transmission function $T(z,\Psi_{s,p},V,E)$ that can be written as

$$T(z,\Psi_{s,p},V,E) \cong exp\left[-2(z+R)\frac{2}{3}\sqrt{\frac{2m}{\hbar^2}}\times\left(\frac{(\Phi_p - E + eV)^{3/2} - (\Phi_s - E)^{3/2}}{\Phi_p - \Phi_s + eV}\right)\right] \tag{1.10}$$

where R is the probe radius.

Combining Equation 1.9 and Equation 1.8, and assuming some constraints regarding the temperature, gap voltage, and geometries, one can conclude that the tunneling

current is proportional to the DOS.

$$\frac{dI}{dV} \propto DOS \propto LDOS \tag{1.11}$$

In conclusion, one can measure the LDOS at the sample surface by measuring the current at different gap voltages.

1.7.2 Atomic Force Microscopy

Even though STM has been demonstrated to be one of the most sensitive techniques for atomic resolution, it is not the most versatile option. That is why the AFM was developed, and it became the most known SPM-based technique. Here, a sharp silicon probe located at one of the cantilever's edges will be used instead of the metallic probe. The main advantage of this kind of probe is its reproducibility, with the possibility of producing thousands of probes in a row via lithography processes. The AFM uses the interatomic interactions between the silicon probe and the sample surface for building the sample topography. The Lennard-Jones potential can describe this physical interaction between the probe and the sample.

$$U_{LJ} = 4\epsilon \left[\left(\frac{\sigma_0}{z} \right)^{12} - \left(\frac{\sigma_0}{z} \right)^{6} \right] \tag{1.12}$$

Figure 1.13 (a) depicts the Lennard-Jones potential (black line). Blue and red lines represent the attractive and repulsive contributions, respectively. Depending on which of the two contributions is chosen as feedback, the AFM operation mode will be defined. If the major contribution comes from the repulsive force, the operation mode is called **contact**, while **non-contact** mode happens when the contribution comes mainly from the attractive force. There is a third mode in which the probe oscillates between both repulsive and attractive regimes; it is called **Intermittent contact** mode (sometimes also called tapping mode). Figure 1.13 (b-d) depicts the sketches of the three operation modes. Notice here that in the non-contact (c) and the intermittent contact (d) modes, the probe mechanically oscillates, sometimes receiving the group name of dynamic modes. In contrast there is no oscillation in the contact mode, then called static mode. These sketches also show an essential feature of the AFM, the optical apparatus used for the feedback control. It is composed of a laser (usually red or infrared lights) focused on the backside of the cantilever. The laser is

then reflected and monitored via a four quadrants photo-detector, which can precisely detect changes in the laser positioning due to horizontal movements of the cantilever.

In contact mode, when the probe apex touches the sample surface, a cantilever deflection changes the laser position in the photo-detector. By keeping a constant cantilever deflection, one can control the force between the probe apex and the sample, which is usually in the order of fewer nN. By scanning the sample surface with constant force, each time a topographical feature changes the deflection of the cantilever, the piezoelectric material will compensate for this change by moving up and down the sample or the probe. The piezo movements are then recorded to create the intensity of the pixels that compose the topographic image.

In the early years since the invention of the AFM, the main goal was to prove atomic resolution on insulator materials. Indeed, less than one year after its invention, the first results showing atomic periodicity on highly oriented boron nitride were presented by Albrecht *et al.*, in 1987 [134], using contact mode AFM. However, at that time, they already knew that contact mode AFM was not providing real atomic resolution since no single structure defects were observed. It is attributed to the elastic deformation of the probe apex and the sample due to the attractive force between the surrounding atoms, resulting in a contact area much larger than an atom, in the order of 5 nm. The true atomic resolution image was achieved only in 1993 by Ohnesorge *et al.* [135] when measurements were performed in a liquid environment. The presence of liquids significantly reduces the attractive forces, reducing the probe/sample deformation and letting only the last atoms of the probe apex to interact with the sample. Contact mode is the simplest AFM operation mode, and it can be performed on any sample and environment with impressive resolution.

The other two modes use a mechanical oscillation of the cantilever and monitor changes in its amplitude, phase, and frequency to measure the surface topography. In the intermittent mode, the cantilever is oscillated at its resonance frequency, with a specific amplitude and phase. The resonance frequency can range from fewer kHz up to MHz, depending on the cantilever configuration, and the oscillation amplitude is in the order of tens of nm. By applying a constant oscillation excitation at a frequency slightly lower than the resonance peak, one should expect the cantilever to oscillate at constant amplitude and frequencies. However, topographical features will change the

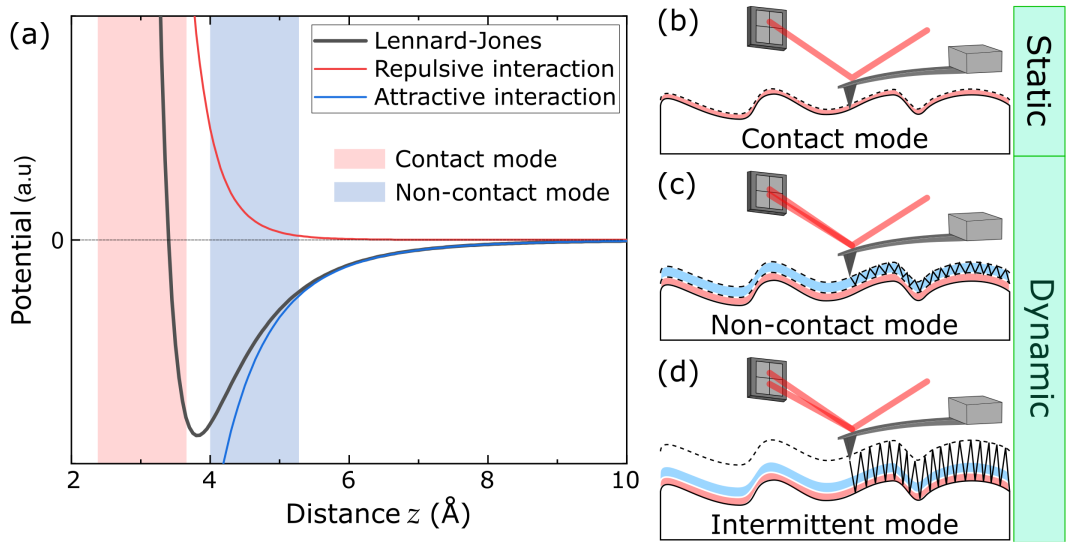

Figure 1.13: Interatomic forces in the AFM: (a) Lennard-Jones potential is used to describe the forces between probe and sample. Schematic for the static operation mode (b) contact, and dynamic operation modes (c) Non-contact and (d) Intermittent.

oscillation amplitude as soon as the sample surface is scanned. Such change can be detected via the photo-detector and analyzed with a lock-in amplifier. The feedback control will then move the sample or the probe up and down to nullify the changes in the oscillation amplitude.

The non-contact mode can be split into two additional categories: Amplitude Modulation (AM) and Frequency Modulation (FM). The difference between them refers to the signal used for the feedback control. The AM uses amplitude signals in a similar way as the intermittent mode. To differentiate the intermittent mode from AM non-contact mode, an understanding of how the cantilever resonance behaves under attractive or repulsive forces is needed [136], [137].

Figure 1.14 (a) shows the cantilever resonance curve, with eigenfrequency f_0, when the probe is far away from the sample surface. Knowing the behavior of the resonance curve under external forces is of fundamental importance for selecting the most stable frequency feedback during the AFM since changes in amplitude (y-axis of the graphs) needs to be monitored. As soon as the probe approaches the surface, a shift towards lower resonance frequencies is observed. This shift is due to the attractive force damping the driving harmonic oscillation of the probe. Further approaches cause the resonance to shift towards higher frequencies, and now the repulsive force is acting.

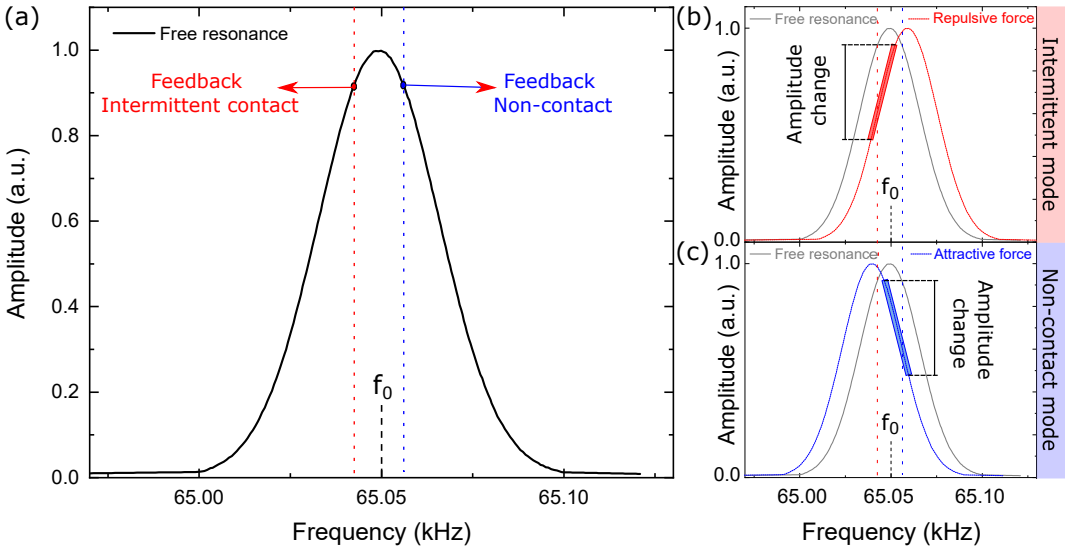

Figure 1.14: Cantilever resonance frequency for the AFM: (a) free resonance (when the probe is far away from the sample surface), (b) shift to higher resonance frequencies due to repulsive forces (intermittent contact), and (c) shift to lower resonance frequencies due to attractive forces (non-contact mode).

On the one hand, choosing a frequency slightly lower than its resonance f_0 is of interest for the AFM feedback when working in intermittent mode, marked in Figure 1.14 (a) as "feedback Intermittent contact." By doing it, when the probe finds a lower feature on the sample surface, meaning increasing the probe/sample distance, the resonance curve will shift to the left, and the amplitude will increase. For higher features, the probe/sample distance decreases, shifting the resonance to the right, which increases the amplitude. In other words, the amplitude change would always be confined in the red square region of the resonance curve, independently of the force direction, as shown in Figure 1.14 (b). Chosen the feedback frequency as f_0 is possible; however, a more substantial shift of the resonance curve is needed to have a significant change in amplitude, which would reduce the AFM signal-to-noise ratio.

On the other hand, slightly higher frequencies at lower amplitudes lead to stable feedback in non-contact mode (Figure 1.14 (c). However, small amplitudes are critical here since attractive forces are limited to short distances, usually lower than 10 nm, where higher amplitudes would make it impossible for the feedback control to track the changes in height.

It is important to notice the dependence of the AFM sensitivity on the quality

factor (Q) of the oscillating cantilever.

$$Q = \frac{f_0}{\Delta f} \tag{1.13}$$

It becomes clear that sharper resonance curves, or higher Q factor, lead to an increase in the AFM sensitivity because it requires smaller changes in the resonance to have the specific change in the amplitude. One way of increasing the Q factor is to operate the AFM under UHV, where Q increases from around 200 up to 40,000. However, the minimal damping in UHV makes it very slow for the AM-AFM to be operated [138]. Equation 1.14 shows the time scale of amplitude changes for the AM-AFM.

$$\tau_{AM} \approx \frac{2Q}{f_0} \tag{1.14}$$

It shows that the higher the Q factor, the slower the response from amplitude. The same is not true for the FM-AFM case [138],

$$\tau_{FM} \approx \frac{1}{f_0} \tag{1.15}$$

Here the time scale does not depend on the Q factor anymore. Therefore, FM-AFM appears as an ideal method to be used under UHV conditions. First, because the higher Q factor provides better sensitivity, and second, AM-AFM feedback would be very slow.

Regardless of the used mode, the AFM technique is proved to be a powerful method for acquiring the topographical information of a sample surface, and it does not matter if the sample is conductive or insulator.

Apart from topography, the AFM provides other channels that can be very useful for data interpretation. In the case of contact mode, the lateral deflection of the cantilever can be used to measure the friction force between probe and sample. The friction force can give a hint at the different material compounds on the surface. For the intermittent and non-contact case, the phase image is another powerful information that can be acquired simultaneously with the topography. The phase image is associated with the oscillation phase of the cantilever, which can be roughly converted in the interaction time between probe and sample. If two different materials with different stiffness or charges are on the surface, the adhesion force between the probe and

Table 1.1: Advantages and disadvantages of the main AFM operation modes

AFM operation modes		
Mode	Advantages	Disadvantages
Contact (Repulsive regime)	- Easiest mode - Can be used under all kinds of environment	- Probe/sample can damage or contaminate more easily
Intermittent contact (repulsive regime) (attractive regime)	- Good signal to noise ratio - Most common mode nowadays	- No atomic resolution - Cannot be operated under UHV
Non-contact (AM) (attractive regime)	- Can be operated under ambient conditions -Prevent probe damages and surface contamination	- Sometimes it is not a true non-contact depending on sample roughness
Non-contact (FM) (attractive regime)	- Highest resolution - Prevent probe damage and surface contamination	- Needs high Q factor for proper operation - Difficult to measure rough samples

the sample will change. Consequently, the phase signal also changes, and estimation of whether different compounds are present on the surface can be done. The phase image will be used once in this thesis in Figure 4.3.

Table 1.1 summarizes the advantages and disadvantages of the main AFM operation modes. Such advantages/disadvantages will be extremely important when deciding which operation mode is more appropriate and convenient to avoid misinterpretation of the data.

1.7.3 Kelvin Probe Force Microscopy

The invention of the AFM brought the possibility of measuring forces over a sample surface locally. In the last section, it was already mentioned that SPMs are not limited to the interatomic forces between probe and sample. Therefore, instead, one can now measure different kinds of physical forces. That is where the electrical AFM-based modes appear. Martin *et al.* [125] showed in 1988 that electrical forces down to 10^{-10} N could be measured using the AFM-based setup. The working principle is based on two main aspects; first, the probe/sample interaction was assumed to act as a parallel plate capacitor. Second, the interatomic forces are predominant only at very short distances between probe and sample, while electric forces are predominant at longer distances [139]. By retracting and keeping a controlled gap distance between probe and sample, they manage to decouple the interatomic from the electric forces. It was the birth of electrostatic force microscopy (EFM) that measured the electrostatic force between the probe and the sample qualitatively. There was a need to measure these properties quantitatively, and a few years later, Nonnenmacher *et al.*, (1991) [124] and Weaver *et al.*, (1991) [140] proposed the KPFM (sometimes called SKPM or KFM), inspired by the 19$^{\text{th}}$ century *Kelvin method* from Lord Kelvin. In the *Kelvin method*, a metallic probe and a sample are considered as a parallel plate capacitor, which produces a current when mechanically vibrated, as given by:

$$i(t) = \omega \Delta C \cos(\omega t) V_{CPD} \tag{1.16}$$

Where ω is the oscillation frequency, ΔC is the change in capacitance, and V_{CPD} is the contact potential difference (CPD) between the plates. By applying a bias voltage V_{DC} to the metallic probe, Equation 1.16 can be rewritten as

$$i(t) = \omega \Delta C \cos(\omega t)(V_{CPD} - V_{DC}) \tag{1.17}$$

When no current $i(t)$ is observed, it means that the applied voltage V_{DC} is equal to the surface potential V_{CPD}.

The KPFM working principle is very similar to the *Kelvin method*, but instead of measuring and nullifying the current, it now nullifies the force between probe and sample. To do so, an AC voltage is applied between the probe and the sample surface, which will generate an oscillating electrostatic force whenever there is a CPD between

them. When the DC bias equals the local V_{CPD}, the net electrostatic force will become zero, and the quantitative CPD map can be recorded.

In the KPFM, the acting force between probe and sample can be written as

$$F = -\frac{1}{2}\frac{\epsilon_0 A}{(z)^2}V^2 = -\frac{1}{2}\frac{\partial C}{\partial z}V^2 \tag{1.18}$$

where the derivative of the capacitance $\frac{\partial C}{\partial z}$ can be written as a function of permittivity constant ϵ_0 the area A and the distance z between probe and sample. The voltage V is composed of the contact potential V_{CPD} the bias V_{DC} and a modulation voltage V_{AC}.

The acting electric force between probe and sample can be written as

$$F = -\frac{1}{2}\frac{\partial C}{\partial z}\left[(V_{CPD} \pm V_{DC}) + V_{AC}sin(\omega_e t)\right]^2 \tag{1.19}$$

It leads to three force contributions. The first one depends on the DC bias only.

$$F_{DC} = -\frac{\partial C}{\partial z}\left[\frac{1}{2}(V_{CPD} \pm V_{DC})^2\right] \tag{1.20}$$

The second depends on the AC bias.

$$F_{\omega_e} = -\frac{\partial C}{\partial z}(V_{CPD} \pm V_{DC})V_{AC}sin(\omega_e t) \tag{1.21}$$

Moreover, a third one depends on the second harmonic of the electrical oscillation, a constant V_{AC}, and $\frac{\partial C}{\partial z}$. Meaning that any change in the local capacitance at the surface can be qualitatively detected.

$$F_{2\omega_e} = -\frac{\partial C}{\partial z}\frac{1}{4}V_{AC}^2\left[cos(2\omega_e t) - 1\right] \tag{1.22}$$

From equations 1.20, 1.21, and 1.22, F_{DC} and F_{ω_e} go to zero when $V_{DC} = V_{CPD}$. A piece of additional information that can be taken during the KPFM is related to the $F_{2\omega_e}$ component. $F_{2\omega_e}$ is not affected by the V_{CPD} and V_{DC}, and qualitative information on the sample's capacitance can be measured at the second harmonic of the electrical signal [141].

However, the main goal during KPFM remains to nullify F_{ω_e} and measure the V_{CPD}. When considering a clean surface and UHV environment, the V_{CPD} is proportional to the workfunction [142]. Now, depending on whether the V_{DC} is applied to

the probe or the sample, the workfunction can be directly or inversely proportional to the CPD. In this thesis, the workfunction will be permanently treated as directly proportional to the measured CPD, which means that higher CPD values lead to higher workfunction and vice-versa. Equation 1.23 can be used to correlate the measured CPD with the workfunction.

$$CPD = \frac{(\Phi_s - \Phi_p)}{e} \tag{1.23}$$

Where Φ_s is the workfunction of the sample, Φ_p is the workfunction of the probe, and e is the elementary charge.

Figure 1.15 depicts the main parts of the KPFM setup. The probe mechanically oscillates at its resonance frequency f_0, and at the same time, an electrical oscillation is applied at ω_e. Independent lock-in amplifiers set at the respective excitation frequencies (f_0, ω_e) read the deflected signal to split electrical from topographical contributions and then build topographic and surface potential maps.

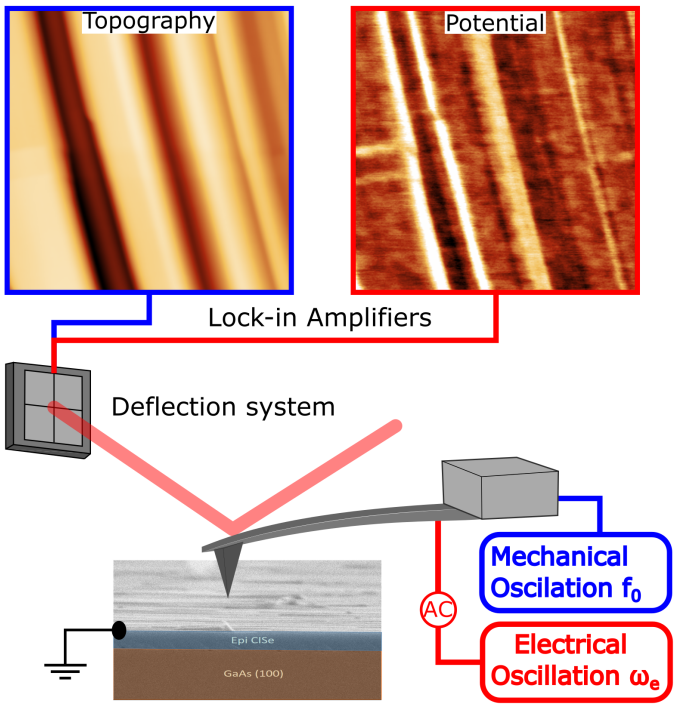

Figure 1.15: Simplified KPFM schematic. A sharp probe is placed close to the sample surface and is mechanically and electrically excited. A deflection system based on a laser deflection measures changes in the cantilever oscillation to produce the topography and surface potential maps.

Similar to the AFM, there are several KPFM operation modes [143], which are again based on measuring the force by means of amplitude, called AM-KPFM, or frequency, called FM-KPFM. There are several ways of doing AM-KPFM, which depend on the chosen AC frequency. The discussion here will be limited to the three main modes: **AM lift mode**, **AM off res**, and **AM 2 EM** [143].

The simplest mode is the AM lift mode, also called double pass KPFM. In this mode, the topography is first acquired in one of the AFM dynamic modes, then the probe is lifted by a controlled gap, and an AC voltage is applied at the same probe resonance frequency for the KPFM [144]. This mode has some advantages, the first one because it is robust and effortless to implement with most commercial SPMs offering it as a standard tool. Secondly, using the first eigenmode f_0 makes the AM lift the best KPFM mode regarding signal-to-noise ratio. However, the acquisition time is doubled since every line needs to be scanned twice, and the larger distance between probe and sample reduces the lateral resolution.

AM off res is a bit more complex, and a second lock-in amplifier is needed [124]. In this case, the AC voltage is applied at a frequency $\omega_e < f_0$ allowing the topography and the surface potential to be acquired simultaneously. The signal decoupling is made exclusively via the lock-in amplifiers operating at f_0 for topography and ω_e for the KPFM. AM off res is a kind of old-fashioned technique because when it was developed, there was a maximum operating frequency of the lock-in amplifiers limiting the technique. AM 2 EM is considered the more reliable AM-KPFM mode, but it is still not primarily used by the community. In this case, the AC voltage is applied at the second harmonic of the probe's resonance frequency f_1, which is $6.3 \times f_0$. The main advantage of AM 2 EM is the signal-to-noise ratio that is considerably improved.

AM modes are usually the most used KPFM techniques, but they are also known to be more prone to artifacts such as cross-coupling of stray capacitance into the measured KPFM signal [145]. Furthermore, Wagner *et al.* [146] showed that for the most common probe geometries in the market, the large surface area of the cantilever contributes more significantly to the measured signal than the probe apex itself, limiting the lateral resolution.

These are the reasons for the development of the FM-KPFM, which is now sensitive to the gradient of the electric force and not to the force itself, as demonstrated

by Colchero *et al.* [145]. It is known from Dürig *et al.* [147] that force gradient is proportional to the frequency shift of the AFM cantilever's free resonance, which is given by:

$$\omega_e^{'} = \sqrt{\frac{k - \partial F(z)/\partial z}{m_{eff}}} \approx \omega_e \left(1 - \frac{1}{2k}\frac{\partial F(z)}{\partial z}\right) \tag{1.24}$$

$F(z)$ being the electric force, m_{eff} the effective mass, and k the force constant of the probe. This model shows that by measuring the frequency shift of the probe, the electrostatic force gradient due to V_{AC} will be consequently measured. However, it is only valid in the case of small oscillation amplitudes of the probe [145]. Therefore, in FM-KPFM, a small amplitude oscillation of the probe is kept constant, and a resonance frequency shift (Δf) is measured. Once again, several ways of acquiring the FM-KPFM data are proposed in the literature, but this thesis focus on only two of them, namely **Sideband FM-KPFM** and **Heterodyne FM-KPFM**.

In the sideband FM-KPFM, the AC voltage is applied at $\omega_e < f_0$, generating sidebands at the eigenmode frequency $f_0 \pm \omega_e$ that are then used as feedback for the KPFM. A schematic of the sidebands generated during a typical FM-KPFM measurement is shown in Figure 1.16.

In this mode, ωe is chosen such that it is high enough to not overlap with f_0 and consequently be affected by topographic information, but also not too high to avoid a decrease in the signal-to-noise ratio. One limitation of the FM-KPFM is related to the scan speed, which is usually limited by the detection bandwidth $\approx f_0/2Q$. Increasing f_0 can increase the scan speed, but most SPM electronics cannot operate in higher frequencies (MHz).

To overcome this issue, the heterodyne FM-KPFM was proposed, where the AC frequency is the difference between the second harmonic and the first eigenmode resonance of the probe $\omega_e = f_1 - f_0$ [149]. By doing it, the sidebands are now sitting close to the second harmonic, leading to an amplified signal without risking dragging topographic information from f_0 and an improved signal-to-noise ratio at a higher scan speed.

Both FM-KPFM modes have proved similar and reliable workfunction measurements. The main difference between them is the acquisition time; however, a comparison between AM-KPFM and FM-KPFM showed that AM-KPFM does not provide

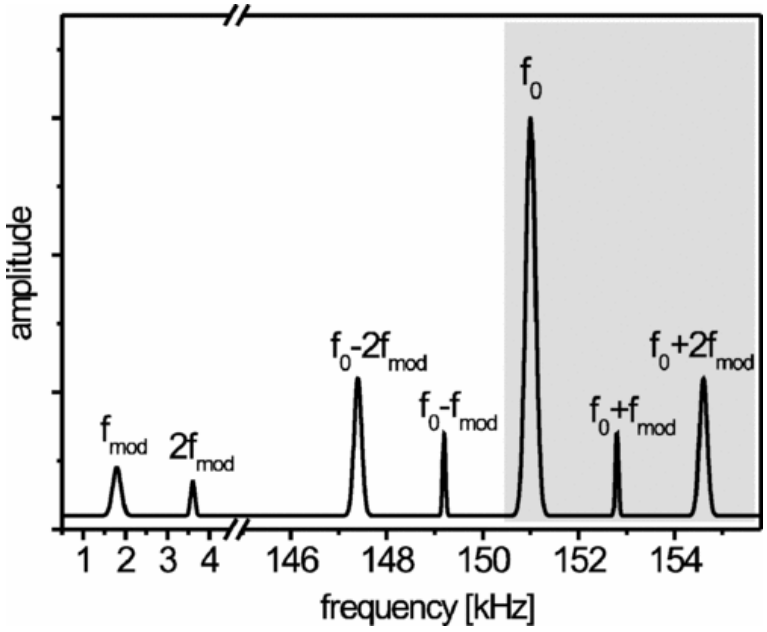

Figure 1.16: Schematic of the FM-KPFM Sidebands. An AC voltage is applied at f_{mod} producing sidebands at the main resonance frequency f−0. During FM-KPFM f−0 ± f_{mod} is measured. Figure reprinted from Zerweck *et al.*, ©(2005) Physical review B - APS.

reliable results [143]. Differences between these modes are generally attributed to the higher lateral sensitivity of the FM-KPFM, where capacitive coupling can be avoided. Even though, due to the more straightforward technical implementation, AM-KPFM lift mode is still one the most frequently used setup under ambient conditions.

Further reading on the theoretical SPM background can be found in the books from Meyer *et al.*, (for STM and AFM)[150], Julian Chen, (for STM and AFM)[151], Bhushan, (for SPM)[152], and Sadewasser *et al.*, (for KPFM)[85].

Table 1.2: Summary of the KPFM techniques

AFM operation modes		
Mode	Applied frequency	Detected frequency
AM-KPFM lift mode	- $\omega_e = f_0$ (50 to 350kHz)	- ω_e *in double pass*
AM-KPFM off res	- $\omega_e < f_0$ (10 to 25kHz)	- ω_e
AM 2 EM	- $\omega_e = f_1$ (300 to 600kHz)	- ω_e *measurement can be limited by the maximum frequency detection of the electronics*
FM-KPFM sideband	- $\omega_e < f_0$ (0.1 to 2kHz)	- $f_0 \pm \omega_e$ *Time acquisition limited by the bandwidth*
FM-KPFM heterodyne	- $\omega_e = f_1 - f_0$ (300 to 1500kHz)	- f_1 *measurement can be limited by the maximum frequency detection of the electronics*

Chapter 2

Materials and Methods

2.1 Sample preparation

The entire set of single-crystal CIGS thin films used in this thesis was grown in collaboration with the laboratory of photovoltaics (LPV) at the University of Luxembourg. Omar Ramírez and Dr. Conrad Spindler, under the supervision of Prof. Dr. Susanne Siebentritt, were responsible for the sample preparation. The films were grown via metal-organic vapor phase epitaxy (MOVPE) on GaAs wafers, which uses chemical reactions of the metal-organic precursors to produce high purity single-crystalline thin films via epitaxial growth. The MOVPE does not need a vacuum to operate, an excellent alternative to standard physical vapor deposition systems.

Figure 2.1 depicts an overview of the processes occurring inside the reactor chamber during growth. The MOVPE system consists of a reactor chamber where a constant gas flux carries the metal-organic precursors. Hydrogen is used as the carrying gas, and a controlled composition can be achieved by adjusting the partial pressure of each metal-organic precursor. When the metal-organic precursors reach the heated reactor chamber, a decomposition process of the gas phase starts, leading to adsorption of the inorganic materials at the surface. As more material reaches the surface, growth takes place. Eventually, due to the high substrate temperature, gas-phase losses of the deposited elements can happen. Usually, the CIGSe samples are grown at 520 °C and 90 mbar. It is essential to use clean, high-quality single-crystal substrates for epitaxial growth, called "epi-ready" substrates. In this thesis, two types of epi-ready substrates were used: the GaAs (100) and the multi-crystalline GaAs substrates (University-

Wafer, Inc.).

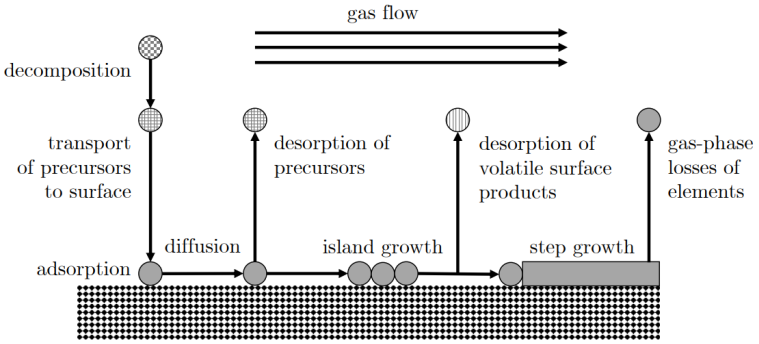

Figure 2.1: MOVPE basic working principle. Figure reprinted from Spindler [153]

Detailed information regarding the samples used in each chapter is shown below.

- Chapter 3

  CIGS: single-crystalline $CuInSe_2$ (CISe) films were grown on (100)-oriented semi-insulating GaAs wafers at 530 °C and 50 mbar. The absorbers were 500 nm to 600 nm thick. Several samples with different Cu/In ratios were prepared and measured via EDX. Additional information regarding the sample properties can be found in [77].

  In Chapter 3, perovskite samples were also used as a proof of concept for the GB characterization via KPFM. Below is a short description of the sample preparation. For more details, see [154]. ***Perovskite***: Methylammonium lead triiodide perovskites ($CH_3NH_3PbI_3$) (MAPI) absorbers were deposited on FTO (fluorine-doped tin oxide) covered glass substrates via co-evaporation carried out in a physical vapor deposition (PVD) chamber embedded in a nitrogen-filled glovebox. A constant temperature of 330 °C was used to evaporate PbI_2, and the temperature of the MAI was kept at 110 °C. The growth was carried out at room temperature.

- Chapter 4

  Single-crystalline Cu-rich $CuInSe_2$ (CISe) films with a thickness of 650 nm grown on (100)-oriented semi-insulating GaAs wafers. A Cu/In ratio of 1.18 was measured by EDX.

- Chapter 5

Single-crystalline Cu-rich Cu(In,Ga)Se_2 (CIGSe) films with a thickness of **200 nm** grown on **semi-insulating multigrain GaAs wafers**. A Cu/(Ga+In) ratio of 0.97 and a Ga/(Ga+In) = 0.34 was deduced by EDX.

- Chapter 6

  Single-crystalline **Cu-rich** Cu(In,Ga)Se_2 (CIGSe) films with a thickness of 500 nm grown on (100)-oriented semi-insulating GaAs wafers. A Cu/(Ga+In) ratio of 1.04 and a Ga/(Ga+In) = 0.42 was deduced by EDX.

  Single-crystalline **Cu-poor** Cu(In,Ga)Se_2 (CIGSe) films with a thickness of 500 nm grown on (100)-oriented semi-insulating GaAs wafers. A Cu/(Ga+In) ratio of 0.97 and a Ga/(Ga+In) = 0.44 was deduced by EDX.

  Cu-rich Cu(In,Ga)Se_2 (CIGSe) films with a thickness of **200nm** epitaxially grown on **multi-crystalline Zn-doped GaAs wafers**. A Cu/(Ga+In) ratio of 0.85 and a Ga/(Ga+In) = 0.30 were deduced by EDX.

  Cu-rich Cu(In,Ga)Se_2 (CIGSe) films with a thickness of **500nm** epitaxially grown **on multi-crystalline Zn-doped GaAs wafers**. A Cu/(Ga+In) ratio of 0.85 and a Ga/(Ga+In) = 0.30 were deduced by EDX.

2.2 Inert-gas transfer system

The samples were introduced into the UHV characterization setup without air exposure via an inert-gas transfer system. The transfer system consists of vacuum parts with special valves that allow the coupling to the glovebox and the UHV characterization setup. A short manipulator was used to transfer the sample from the transfer system to the UHV setup. A picture of the inert-gas transfer system can be seen in Figure 2.2.

2.3 Ultra-high vacuum (UHV) characterization setup

Figure 2.3 shows the UHV setup used for sample characterization and K-deposition as used in this thesis. The system's main parts are highlighted in the picture, where the SPM camber, the XPS chamber, the preparation chamber, the alkali evaporator, and the inert-gas suitcase can be seen. The system has one turbo molecular pump

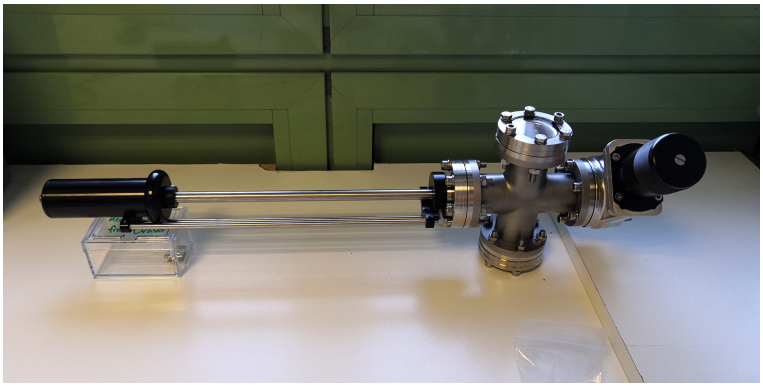

Figure 2.2: Picture of the inert-gas transfer system.

and an ion pump that allows reaching a base pressure of $\approx 1 \times 10^{-10}$ mbar. An anti-chamber is used for transferring samples from the suitcase to the UHV system without venting the preparation chamber. Alkali deposition, sputtering, thermal treatments, and controlled gas injection can be performed in the preparation chamber.

2.3.1 Scanning probe microscopy

UHV VT-AFM system (Scienta Omicron) was used for the SPM characterization. The current setup allows topographies to be measured in STM and AFM modes. Electrical measurements such as scanning tunneling spectroscopy (STS), conductive AFM, and KPFM are also implemented. Measurements at variable temperatures can be done as well. In this thesis, mainly KPFM measurements were performed.

2.3.1.1 Kelvin probe force microscopy

As shown in subsection 1.7.3 several KPFM modes exist. In the current UHV setup, two main modes are available, the FM-KPFM sideband and AM-KPFM 2 EM. Reminder: two independent lock-in amplifiers are used during KPFM, one for topography and another for electrostatic measurements. Due to the UHV conditions (see Table 1.1, the topography is acquired in frequency modulation (FM), independently of using AM-KPFM or FM-KPFM modes. In other words, one lock-in amplifier uses FM to measure the topography, and another one uses AM or FM to measure the surface potential map.

The Ametek signal recovery 7280 DSP lock-in amplifier was used for processing the KPFM signal. In the following, a description of the used parameters will be presented.

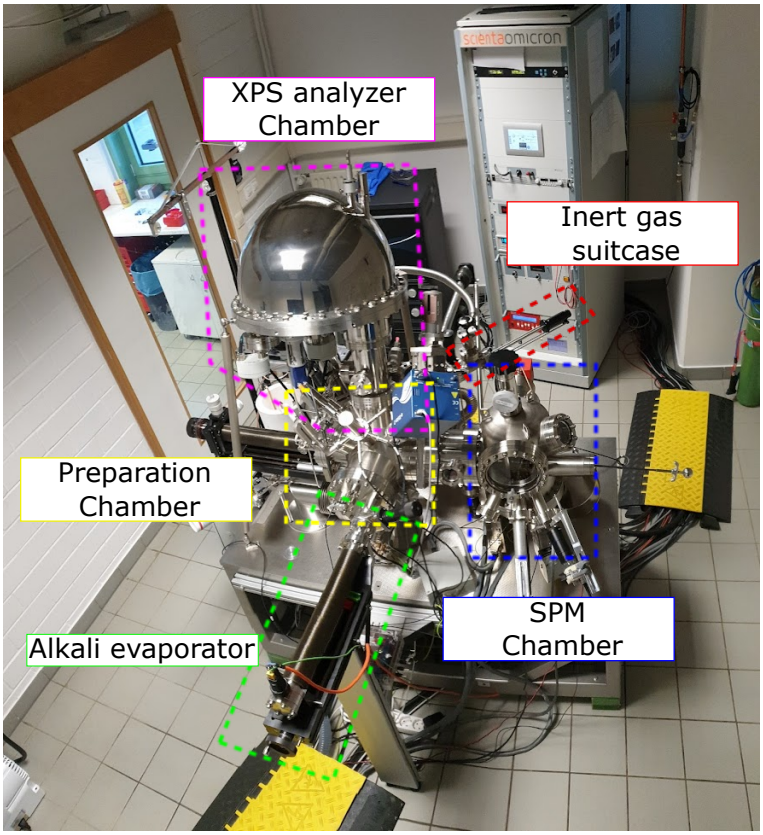

Figure 2.3: UHV characterization setup used in this thesis.

FM-KPFM sideband Typical lock-in amplifier settings:

- applied AC voltage range from 0.2 V to 0.4 V
- resonance frequency ranging from 1 to 1.5 kHz
- Time constants of between 1 to 10 ms
- sensitivity between 1 to 10 mV

A full image with 300px × 300px, was acquired in ≈ 1 hour. Increasing resolution and time constants can easily result in a 6 hours measurement. The used probes were PPP-EFM (nanosensors) and 240AC-NA OPUS by MikroMasch with resonance frequencies between 70 kHz and 90 kHz. Both had a Pt/Ir thin film deposited on a Si probe. A slight advantage of the 240AC-NA probe is the width of the cantilever. As the current SPM setup has a fixed laser position and the probe moves during the scan, larger probes help to keep the laser intensity constant.

AM-KPFM 2 EM Typical values used in the lock-in amplifier

- applied AC voltage range from 0.1 V to 0.2 V
- resonance frequency at the 2^{nd} harmonic of the cantilever‘s resonance (between 300 and 600 kHz)
- Time constants of between 1 to 10 ms
- sensitivity between 1 to 10 mV

Like AM-KPFM, images usually take from 1 to 6 hours per frame. The used probes were Pt/Ir PPP-EFM (nanosensors) with resonance frequencies between 70 kHz and 90 kHz

2.3.2 X-ray photoelectron spectroscopy

X-ray photoelectron spectroscopy (XPS) is a surface-sensitive technique that measures photoelectrons ejected from the sample due to an X-ray excitation. The ejected photoelectron contains information regarding the elemental composition at the sample surface. Figure 2.4 depicts the XPS basic working principle. An X-ray source is used to excite electrons from the atoms; for example, in Figure 2.4 (a), it excites electrons from the inner K shell. If the electron gains enough energy, it can escape from the sample surface to the vacuum level (Figure 2.4 (b). The kinetic energy of the electrons that left the surface can be defined as:

$$E_{kin} = h\nu - E_{bind} - \Phi \tag{2.1}$$

Where $h\nu$ is the X-ray energy, E_{bind} is the binding energy of the electron, and Φ is the workfunction of the spectrometer (considering the Fermi level between sample and spectrometer to be aligned). If the kinetic energy is measured, the binding energy can be easily calculated by knowing the spectrometer workfunction and the X-ray energy.

The binding energy of electrons depends on many factors, e.g., the atom and the orbital from which the electron is ejected, the chemical environment, etc., and their tabulated values can be found in many handbooks [156], [157].

Additionally, when one electron is removed from a core level of an atom, another electron with higher energy could fill this vacancy and release a photon. This photon can be either emitted in the form of fluorescence or excite another electron, called

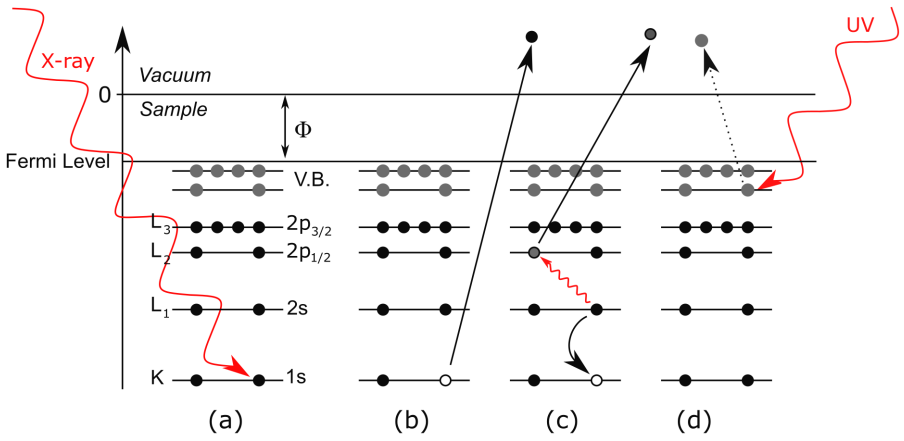

Figure 2.4: XPS basic principles. Figure reprinted from [155]

Auger electrons Figure 2.4 (c). Once again, if enough energy is provided to the second electron, it has a probability of escaping the sample surface and being detected by the analyzer.

The kinetic energy of the photoelectrons pretty much depends on the X-ray energy, whereas the Auger electrons are always emitted with the same kinetic energy. That is the reason why different X-ray sources help to "move" Auger peaks (in the binding energy plot) to regions where they do not overlap with the binding energy of photoelectrons. Switching from the Al X-ray source (1486.6 eV) to the Mg X-ray source (1253.3 eV), the Auger lines will relatively move by 233 eV in the binding energy plot.

The spectral lineshape of the core hole with a lifetime τ is a Lorentzian function with a certain full width at half maximum (FWHM), the so-called intrinsic or natural linewidth. Gaussian lineshapes with FWHM rely on user settings, which are associated with instrumental response, x-ray line-shape, and thermal broadening. The combination of intrinsic and instrumental effects results in the experimentally observed linewidth [155]. Nonetheless, most of the data discussed in the results chapters are limited by the Gaussian lineshape.

The main instrumentation parts of the XPS are the X-ray source, the kinetic energy analyzer, and the detection system.

Many kinds of X-ray sources exist, but the most common ones in laboratory systems are based on high-energy electrons bombarding a metallic target that will then emit X-rays. One limitation of this kind of source is the energy loss via heating, limiting

X-ray power [155]. Another issue is related to the broadening of the X-ray and the appearance of satellite peaks (minor resonance lines in the X-ray spectrum). This issue can be overcome by using monochromatic sources, where a quartz crystal filters the X-ray source leading to a sharper spectral emission. Part of the analyzed data in this thesis was measured with a monochromatic source.

The kinetic energy analyzer aims to separate electrons by their kinetic energy, and hemispherical sector analyzers are usually a good candidate for that. It consists of two concentrically metallic hemispheres with radii $R_{inner} = R_1$ and $R_{outer} = R_2$. A potential difference ΔV is applied between the inner and outer hemisphere, and this electrostatic field guides the trajectory of the incoming electrons. A dispersion of the electrons will exist due to different bending of their trajectory inside the analyzer, which pretty much depends on the electron energy. Higher-energy electrons deflect less than lower-energy electrons in the same electric field. To physically limit the size of the hemispherical analyzer, electrons have to be retarded (or accelerated) to a preset kinetic energy, called the pass energy E_p. It allows only energy within the pass energy to enter into the analyzer. Decreasing the pass energy increases the energy resolution but reduces the number of electrons that will reach the detector per unit of time. Typical values for pass energy in XPS range between 20 eV to 200 eV.

After crossing the hemispherical analyzer, the electrons reach the detector. Usually, the detector alone cannot detect the small number of particles arriving, and there is a need for amplification of the signal. Different detection systems with their amplification exist, and each of them has specific advantages and disadvantages. The two most used detection systems in XPS are the 2d microchannel plate and the channeltron.

In a channeltron detector, the incident particles are multiplied due to several secondary electron emission processes, generating an electron avalanche registered by the electronics [155]. High count rates are the main advantage of this detector; consequently, faster measurements or lower X-ray power are required. The 2d microchannel plate is a 2-dimensional electron multiplier that is often used with a phosphorous screen and a CCD camera. Particles hit the microchannel plate, generating an electron avalanche. These electrons are then accelerated towards a phosphorous screen that emits a spotlight detected by the CCD camera. In addition to the microchannel plate, the 2d delayline detector can be added, which besides the 2d information, also

provides the impact time of each particle for an accurate counts per second measurement. The 2d microchannel plate has a lower count rate than the channeltron detector; however, it is much more robust and provides two-dimensional information [155].

During this thesis, two XPS experimental setups were used. One of them is a commercial UHV system from SPECS equipped with a PHOIBOS 100 hemispherical analyzer and a delayline detector. A monochromated Al K α x-ray source with a photon energy of 1486.74 eV was used. Results obtained with this machine are limited to section 6.2, where collaboration with researchers from Westfälische Wilhelms-Universität and the Center for Nanotechnology (CeNTech) at Münster in Germany was done. The measurements were done by Amala Elizabeth under the supervision of Dr. Harry Mönig.

The second XPS experimental setup is a commercial UHV system from Prevac, where the EA-15 energy analyzer chamber was assembled into the Scienta Omicron UHV preparation chamber. The Prevac XPS system has a 2d microchannel plate and a twin anode achromatic X-ray source. The twin anodes allow emissions at 1253.6 eV for the Mg K α and 1486.6 eV for the Al K α. A comparison between both sources applied to CIGSe, where potassium was deposited on the surface, can be found in Appendix A.2.

2.3.3 Alkali deposition

Metallic evaporation of potassium was performed under UHV by heating an alkali metal dispenser, ensuring very pure alkali thin films [96]. The homemade evaporator consists of a filament dispenser (supplier: SAES group) containing K_2CrO_4, that releases K when heated at $\approx 600°$ (5.3 A). The evaporator is mounted on a manipulator that can travel 30 cm toward the sample surface. During depositions, the filament was kept at ≈ 2 cm from the sample surface. A straight aperture is positioned in front of the filament to guide the evaporation flux, as shown in Figure 2.5.

A voltage is applied to the filament, and the measured current can be adjusted to precisely control the evaporation rate. Additionally, a thermocouple is mounted close to the filament, displaying temperature changes during deposition. Initial tests of the evaporator were made on gold surfaces, where two trials to optimize the evaporation procedure were done. KPFM was used to in-situ monitor changes in workfunction

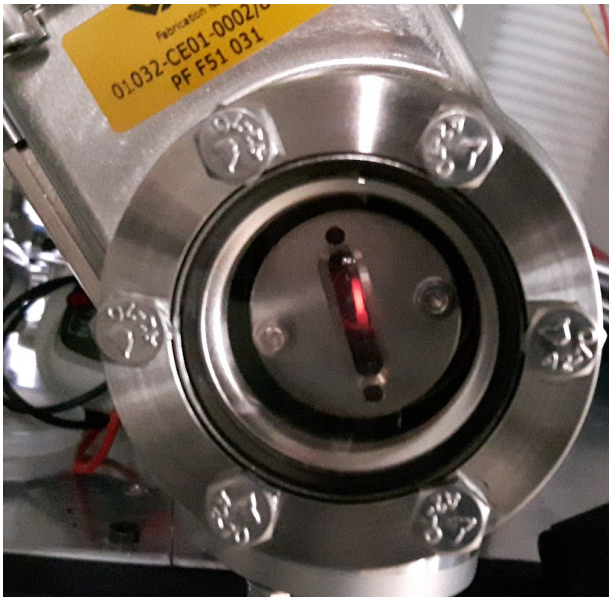

Figure 2.5: Alkali evaporator under commissioning, showing the filament (red-ish) and the straight aperture in front of it.

after evaporation. Table 2.1 shows the first trial on gold, where the workfunction slowly reduced as the set current and evaporation time increased. In this trial, the filament was heated up (from 3A to target current) within 15 seconds, and from there on, the deposition started.

The deposition at 10.0 A for 2 minutes resulted in a massive change in workfunction that is close to the expected workfunction of K. However, much more than a few nanometers of K was deposited. Indeed, Figure 2.6 shows that, even by eye, a well-defined contrast (brighter square) is observed where K was deposited.

Table 2.1: Trials for the K evaporation on Gold surface.

Evaporator trials	
Deposition procedure	Work function
No evaporation (Gold)	5.100 eV
7.0A for 30 seconds	5.037 eV
7.0A for 2 minutes	5.000 eV
7.5A for 2 minutes	4.965 eV
8.0A for 2 minutes	4.900 eV
10.0A for 2 minutes	2.961 eV

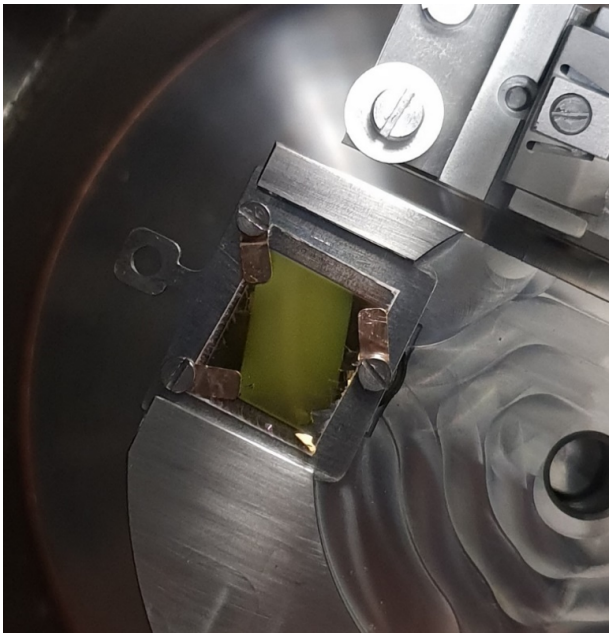

Figure 2.6: Potassium deposition on gold for the trial 10.0A for 2 minutes.

In a second trial, the emission stability was also taken into account by waiting for the thermal equilibrium of the filament. A slow increase of the temperature (5 min/A) until reaching 5.5A, then evaporation at 8A for 10 minutes was done. Using this procedure, the workfunction changed from 5.1 eV to $\approx$ 3.0 eV. Nevertheless, no visible changes in the gold substrate were observed, indicating that only very few nanometers were deposited on the surface. More detail on the film thickness will be discussed in Chapter 6.

Therefore, the entire set of K-deposited samples in this thesis follow the description below. The slow increase of the current (5 min/A) until reaching 5.5A, then the current was set to 8 A for 10 minutes. Subsequently, the sample was annealed for 30 minutes at 200 °C under UHV conditions. A standard resistive PBN-heater controlled with a TDK-lambda power supply was used for the annealing. With an output power of 9 W, 15 minutes are needed to reach a sample holder temperature of 200 °C, which gives an average ramp rate of 11 °/min. A stable temperature over 30 minutes of annealing was achieved by reducing the output power to 8 W.

2.4 KPFM under air/Nitrogen conditions

Topography and KPFM analyses under ambient or nitrogen conditions were carried out in a Bruker Multimode V, using a PPP-NCHR Nanosensors cantilever. The SPM is placed inside a glovebox where the environment can be controlled, and air exposure is avoided by using a sealed sample box for transferring samples. In this setup, the topography is always acquired in amplitude modulation, but it is possible to choose between intermittent contact mode or non-contact mode operation depending on which side of the resonance curve was used as feedback (see Figure 1.14). Several ways of measuring KPFM are possible in this setup, but only three modes were used in this thesis: AM-KPFM lift-mode, AM-KPFM 2 EM, and FM-KPFM sideband (see Table 1.2 for more details). Similar to the UHV case, the used probes were PPP-EFM (nanosensors) and 240AC-NA OPUS by MikroMasch with resonance frequencies between 70 kHz and 90 kHz. Both had a Pt/Ir thin film deposited on the Si probe. AM-KPFM lift-mode is a default technique for the current setup, and no additional features are needed for operation. In this mode, the topography is acquired in the first pass, and the surface potential information is acquired in the second pass by retracting the probe a few nanometers away from the sample. The distance between probe and sample is always kept constant by using the previously measured topography contour. However, for AM-KPFM EM and FM-KPFM sideband, an additional lock-in amplifier is required. In this thesis, the MFLI 500 kHz / 5 MHz lock-in amplifier from Zurich Instruments was used, which allows topography and surface potential to be measured simultaneously in a single pass. In the following, the parameters used for operation are presented.

AM-KPFM lift-mode

- applied AC voltage 5 V
- resonance frequency is the same as the cantilever‘s resonance (between 70 and 90 kHz)
- lock-in phase 120 °
- lift-height between 5 to 100 nm

- scan rate between 0.1 Hz - 0.5 Hz depending on the image size

AM-KPFM 2 EM

- applied AC voltage range from 1 V to 4 V
- resonance frequency at the 2^{nd} harmonic of the cantilever's resonance (between 300 and 600 kHz)
- target bandwidth $\approx$ 1000 Hz
- scan rate between 0.1 Hz - 0.5 Hz depending on the image size

FM-KPFM sideband

- applied AC voltage range from 1 V to 4 V
- resonance frequency ranging from 1 to 1.5 kHz
- target bandwidth $\approx$ 10 Hz
- scan rate 0.1 Hz

2.5 Other characterization techniques

2.5.1 Scanning electron microscopy (SEM)

Scanning electron microscopy (SEM) was usually applied to measure large areas of the samples at 5kV in a JSM-6010LV Jeol apparatus. Calibrated energy-dispersive X-ray spectroscopy (EDX) was performed in collaboration with the laboratory of photovoltaics (LPV) at the University of Luxembourg.

2.5.2 Secondary-ion mass spectroscopy (SIMS)

Secondary-ion mass spectrometry (SIMS) was carried out in collaboration with Luxembourg Institute of Science & Technology - LIST using a Cameca SC-Ultra apparatus. Sputtering was done with Cs^+ ions with an energy of 1 keV at a 10 nA beam current. The measurements were done by Brahime El Adib and Dr. Nathalie Valle. Details can be found in [158].

2.5.3 Helium Ion Microscope-based Secondary-ion Mass Spectrometry

Helium ion microscope-based secondary-ion mass spectrometry (HIM-SIMS) was carried out in collaboration with Luxembourg Institute of Science & Technology - LIST using a Zeiss ORION helium ion microscope (HIM) with a dedicated SIMS detector added to it. This setup makes use of the impinging He^+ and Ne^+ ions, promoting a collision cascade, which sputters the atoms from the surface. Some of the sputtered atoms can spontaneously ionize, called secondary-ions, which can be in a magnetic sector according to their mass/charge ratio. The main advantage is locally measuring the elements present on the sample (surface and bulk) with a lateral resolution of $\approx$ 20 nm, and $\approx$ 10 nm in depth [159].

In this thesis, HIM-SIMS was used to investigate how potassium diffuses into the CIGSe bulk. Ne^+ ions were used to generate secondary-ions from the sample surface. The setup detected the secondary-ions in two steps, first in positive mode (electropositive ions) and then in negative mode (electronegative ions). In the current setup, up to four mass channels can be detected simultaneously. Potassium, copper, gallium, and indium are measured in the positive mode, while oxygen, carbon, and selenium are measured in the negative mode. Measurements were done by Dr. Jean-Nicolas Audinot.

2.5.4 Photoluminescence

Photoluminescence imaging was carried out in a custom-built setup that allowed for homogeneous illumination of samples up to an area of $1\times1\,cm^2$ with a pulsed 532 nm laser, equivalent to one sun illumination conditions. The emitted PL signal was collected via an InGaAs-based camera with a high quantum efficiency in the near-infrared. A long-pass filter was used to remove the luminescence originating from the underlying GaAs wafer. The samples were placed inside a sealed box with a glass cover from where the light entered. The sealed box was filled with nitrogen to avoid air exposure.

2.6 Calculation of the cantilever contribution to AM-KPFM

Two Python scripts were written to calculate the contribution of the capacitive coupling between the probe and the sample surface. In the first one, a calculation of the individual contribution of each part comprising the probe (cantilever, cone, and apex), as proposed by Wagner *et al.* [146] (see equations 3.2 3.3, and 3.4 and Figure 3.10) was calculated. The second script was based on Equation 3.8 and used each pixel of the topography image as an input for the Δh.

The following parameters were used: Distance between the probe apex and the sample $z = 50\,\text{nm}$ that is equal to the lift height used in the measured image. The potential difference between probe and sample U_{ts} was assumed to be $0.15\,\text{V}$, with the air permittivity $\epsilon_0 = 8.85 \times 10^{-12}\,\text{Fm}^{-1}$. The geometrical probe characteristics were taken from PPP-EFM NanoSensors, where the cantilever length and width are equal to $225\,\text{nm}$ and $28\,\text{nm}$, respectively. The cone height H = $12.5\,\text{nm}$. A random noise function was introduced to mimic the noise level of the KPFM.

Chapter 3

How different KPFM operation modes and environments impact the GB investigation?

Before starting, it is worth emphasizing that most of the results that will be presented in this chapter are published under the following article Lanzoni *et al.* [160].

As mentioned in Chapter 1, high-performance polycrystalline thin-film solar cells are very promising technologies as an alternative to silicon-based solar cell devices. Many efforts have been applied to make such thin films more efficient and cheaper. To reduce their manufacturing costs, most thin films are deposited on cheap substrates, i.e., glass, which leads to polycrystallinity with typical grain sizes ranging from tens of nanometers to a few micrometers. Consequently, an especially debated topic appears, called GBs.

Also, Chapter 1, showed that many open questions related to the beneficial or detrimental effect of the GB on solar cell performance are not unanimous in the community. It is known that the interruption in the crystal periodicity can lead to the appearance of defect states that eventually produce charges at the GBs [9], [10]. Especially here, SPM-based techniques have been largely applied to measure changes in the optoelectronic properties at the GBs [84]–[86], [88], [89], [161], [162]. This is because KPFM measures very precisely and locally the workfunction (difference between the vacuum and Fermi levels) at the sample surface. If defects produce localized charges at the GBs, one could expect a downward or upward band bending, which results in

a bending of the vacuum level right at the GB. Therefore, KPFM is the perfect tool to locally measure such kind of band bending, becoming an ideal technique to study the electronic property of GBs. Indeed, quite a few results in the literature associate variations in PCE of polycrystalline solar cells with charge accumulation at the GBs.

Figure 3.1 shows a plot of the PCE vs. the CPD between the grain and GB, using data from the literature. To simplify the data visualization, all the measurements were converted so that the KPFM bias was applied to the sample. It is necessary in order to make the CPD directly proportional to the workfunction, meaning that negative values for the CPD differences are assumed to produce a downward band bending and vice-versa. In Figure 3.1, the solid symbols represent the air-exposed measurements, while the empty symbols represent the samples measured under UHV or inert gas conditions. From the graph, a preferential trend for downward band bending for both compounds, CIGSe and $CH_3NH_3PbI_3$ MAPI absorbers, is observed. Additionally, there exists stronger confinement of the CPD data inside the range of -150 mV to 150 mV, with UHV/glovebox data presenting stronger band bending. However, no clear correlation between PCE and GB band bending can be observed, and whether a certain GB band bending is beneficial or detrimental for high-efficiency devices from Figure 3.1 cannot be answered. This result could be expected since losses in solar cell performance are not only limited to GBs, and could be linked, for example, to bad extraction layer for the carriers, issues with diffusion length, and high recombination velocity ([3], [4], [35]). Therefore, it is essential to notice that the available data has many undefined factors that could interfere with the measured CPD via KPFM.

This chapter will focus on two of the above-mentioned factors, namely, the environmental conditions and the KPFM operation modes. A very detailed and systematic study to elucidate how these two factors can lead to misinterpretation of the measured CPD will be presented in the following. Usually, AM-KPFM in the air is the most used operation mode reported in the literature for measuring workfunctions in solar cells; however, FM-KPFM in UHV is reportedly in the SPM community to be the most precise method (see section 1.7). That is the reason why these two setups were selected to be extensively studied. The chapter starts by showing a comparative study between AM-KPFM and FM-KPFM on a standard sample made of Au patterns on Si substrate. In the following, a single-crystalline CISe epitaxially growth on

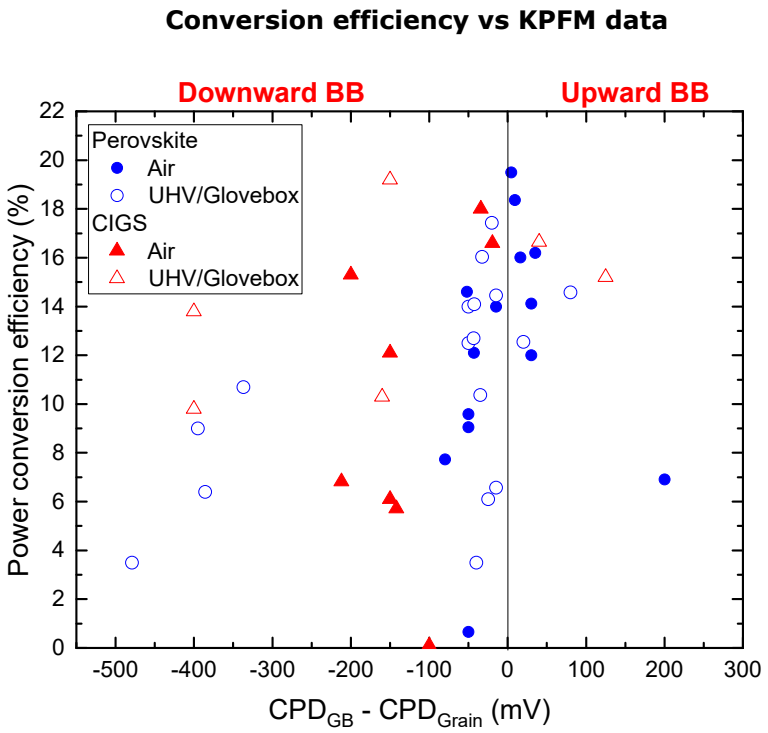

Figure 3.1: Contact potential difference CPD_{GB} - CPD_{Grain} for $CH_3NH_3PbI_3$ and CIGSe absorbers as a function of the reported PCE. Figure adapted from Lanzoni *et al.*, p. 2021 [160]

GaAs(100) will be investigated. The sample is ideal for fundamental studies because less complex structures are comprised on the surface. On top of that, this sample has no PDT or air exposures that could change its electronic properties. Moreover, the learned knowledge is applied to polycrystalline methylammonium lead triiodide perovskites ($CH_3NH_3PbI_3$) (MAPI) grown on ITO substrates. Finally, simulations of the probe/sample interaction at the GB are presented.

3.1 Gold on Si standard sample

In subsection 1.7.3, the theoretical background of the KPFM working principles was discussed. It was shown that KPFM could work in different operation modes, namely AM-KPFM and FM-KPFM. Besides the fact that the resolution of both modes is proven to be different from each other [143], [145], [148], one should expect the measured workfunction to be the same. In the end, this is what, in theory, should occur. To verify this claim, the two main KPFM operation modes and environmental condi-

tions will be compared in the following. KPFM of a commercial standard sample made of gold patterns on Si is shown in Figure 3.2. Figure 3.2 (a,c) shows the topography and the surface potential maps of the sample acquired in AM-KPFM under ambient conditions, and Figure 3.2 (b,d) depicts the maps obtained in FM-KPFM under UHV conditions.

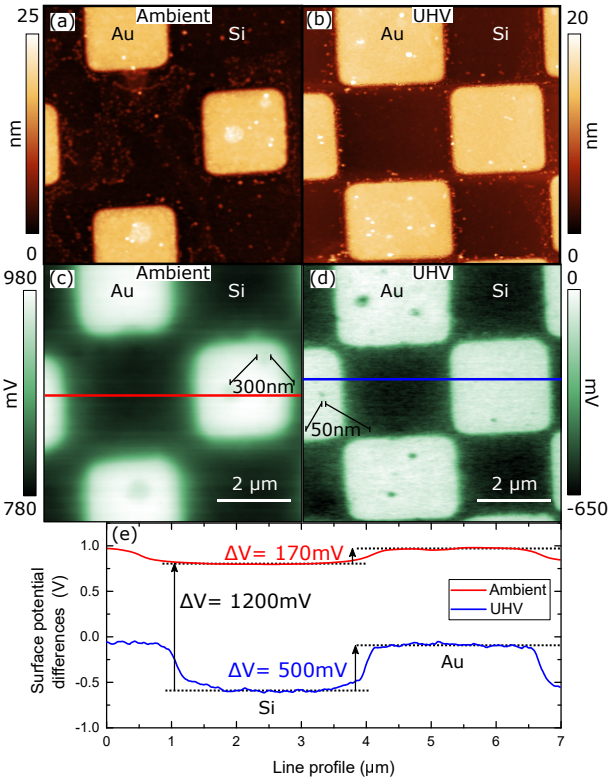

Figure 3.2: KPFM operation mode applied to Gold on Si standard sample: topography and surface potential maps acquired in AM-KPFM under ambient conditions (a,c) and in FM-KPFM under UHV (b,d). (e) Line profiles extracted from the surface potential maps under ambient (red) and UHV conditions (blue). Figure reproduced with permission from Lanzoni *et al.*, ©(2021) Nano Energy - Elsevier [160].

From the topographic images in Figure 3.2 (a,b), the bright regions refer to the gold patterns, which have heights in the order of 20 nm. The surface potential images Figure 3.2 (c,d) show a higher workfunction value for the gold than the surrounding Si, which agrees with their expected workfunction values (5.3 eV for gold and 4.85 eV for Si with SiO_2 native layer, or $\approx$ 450 meV difference between them [163]). The measurement acquired in FM-KPFM under UHV provides better lateral resolution than the measurement obtained in AM-KPFM under ambient conditions, as highlighted by the

larger number of features visible in Figure 3.2 (d) than Figure 3.2 (c). Features with 300 nm are barely seen in the surface potential map acquired in AM-KPFM under ambient conditions, while the FM-KPFM under UHV shows well-defined features down to sizes of 50 nm. Indeed, the line profiles (Figure 3.2 (e)) show that the lateral resolution improved, and the CPD differences between gold and Si are not matching. The expected workfunction differences between gold and native SiO_2 on top of Si are in the order of 450 meV, which is very close to the measured value in the FM-KPFM under the UHV case (500 mV), but far away from the value measured value in the AM-KPFM under ambient conditions (170 mV). Additionally, a massive shift of 1200 mV in the background level of the CPD is observed between both measurements.

Several can be the reasons for the observed differences within these results, such as, measurements performed in different areas of the samples, different KPFM probes, a dielectric contribution from the water layer on the sample surface [164]–[166], the stray capacitance coming from the cantilever contribution [145], and so on. However, the only takeaway message from these data is that the most used KPFM mode, the AM-KPFM under ambient conditions, does not provide the same result as the claimed more precise FM-KPFM mode under UHV, as already demonstrated by many authors [85], [143], [145], [148], [167].

AM-KPFM and FM-KPFM were also performed under UHV at the exact position of the gold pattern sample and using the same KPFM probe to eliminate the environmental contributions. These measurements are depicted in Figure 3.3, where again, the brightest regions represent the gold patterns, and the darkest regions represent the Si substrate. Similar to the measurements carried out under ambient conditions, the AM-KPFM (Figure 3.3 (b)) measurement shows lower lateral resolution compared to the FM-KPFM (Figure 3.3 (d)). It is possible to see from the images that the surface potential in the AM-KPFM does not have the same well-defined contour between Si and the Au patterns. Once again, features down to 50 nm are easily visible on FM-KPFM, while AM-KPFM barely resolves features with 300 nm size.

Figure 3.3 (e) depicts the surface potential line profiles extracted from the same region of the sample using AM-KPFM (red) and FM-KPFM (blue). A very smooth line profile is observed for the AM-KPFM, which is in accordance with its reported lowest lateral resolution [85], [143], [145], [148], [167]. However, the measured value

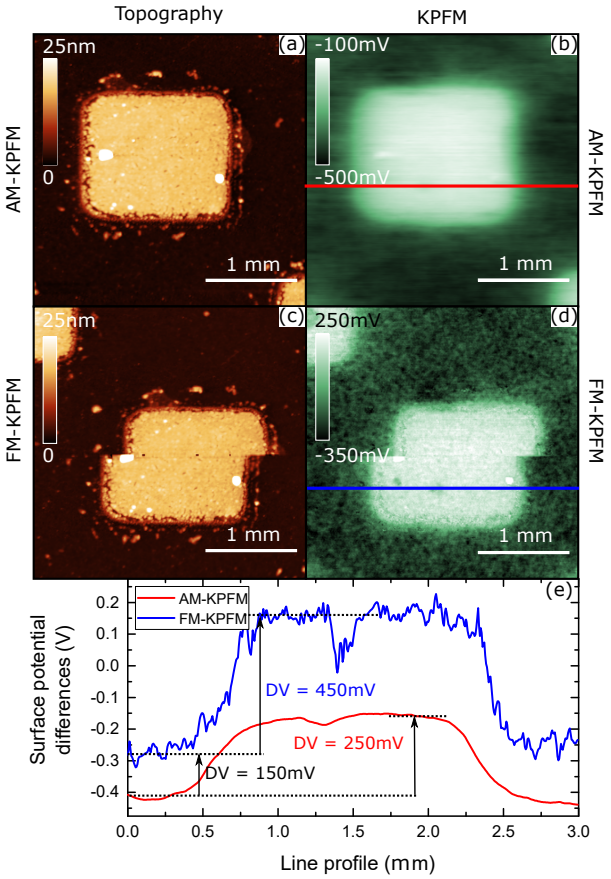

Figure 3.3: KPFM operation mode applied to Gold on Si standard sample under UHV: Topography and surface potential maps measured in the same region using AM-KPFM (a,c) and FM-KPFM (b,d). (e) Line profiles extracted from the surface potential maps in AM-KPFM (red) and FM-KPFM (blue). Figure reproduced with permission from Lanzoni *et al.*, ©(2021) Nano Energy - Elsevier [160].

is roughly half of the one measured with FM-KPFM mode (250 mV compared to the 450 mV).

From Figure 3.2 and Figure 3.3, independent of the environmental conditions, AM-KPFM and FM-KPFM measurements clearly produce different results even when the environment and working conditions are unchanged, with FM-KPFM offering better lateral resolution and workfunction values much closer to the tabulated workfunction values. Additionally, ambient conditions can massively shift the workfunction measured via KPFM.

3.2 KPFM measurements on single-crystalline CISe

In the following, KPFM measurements on the single-crystalline CISe grown on GaAs(100) will be shown. Figure 3.4 shows the morphology of the single-crystalline CISe sample measured via (a) AFM and (b) SEM microscopes. This sample has a very particular morphology, where a preferential growth direction leads to a formation of trenches parallel to the [011] direction. It turns out that this sample is very convenient for the current investigation of possible KPFM artifacts due to these well-aligned topographical structures. Additionally, the observed differences of around 100 nm between the apex and the valley of the trenches can be of particularly interesting for the solar cells application, where the GBs height ranges from a few to hundreds of nanometers.

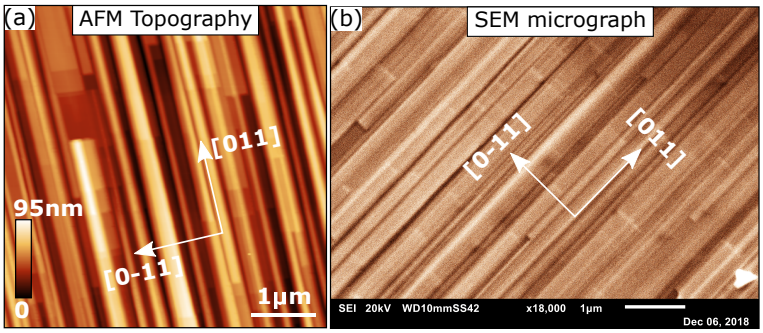

Figure 3.4: AFM and SEM images of the single-crystalline CISe sample showing the faceting at the surface.

In analogy to the standard sample case, ambient AM-KPFM (Figure 3.5 (a,b)) and UHV FM-KPFM (Figure 3.5 (c,d)) were also acquired. Figure 3.5 depicts the topography (a-c) and the surface potential (b-d). The images were not acquired in the identical positions of the sample, but one can see that both topographies present similar structures with trenches parallel to the [011] direction. Such textured growth in CISe materials is well known for the epitaxially grown sample, which is attributed to the most favorable formation of the polar {112} facets [48], [168]. Besides no considerable changes in the topography, the surface potential maps are very different. In the UHV FM-KPFM case (Figure 3.5 (b)), changes in the workfunction up to 300 mV and parallel to the [011] direction are visible, while in the ambient AM-KPFM, no contrast is observed at all. There are several reasons for this observation, but the first obvious one is that both measurements were carried out under different environmental conditions. The measurements under ambient conditions should be influenced by

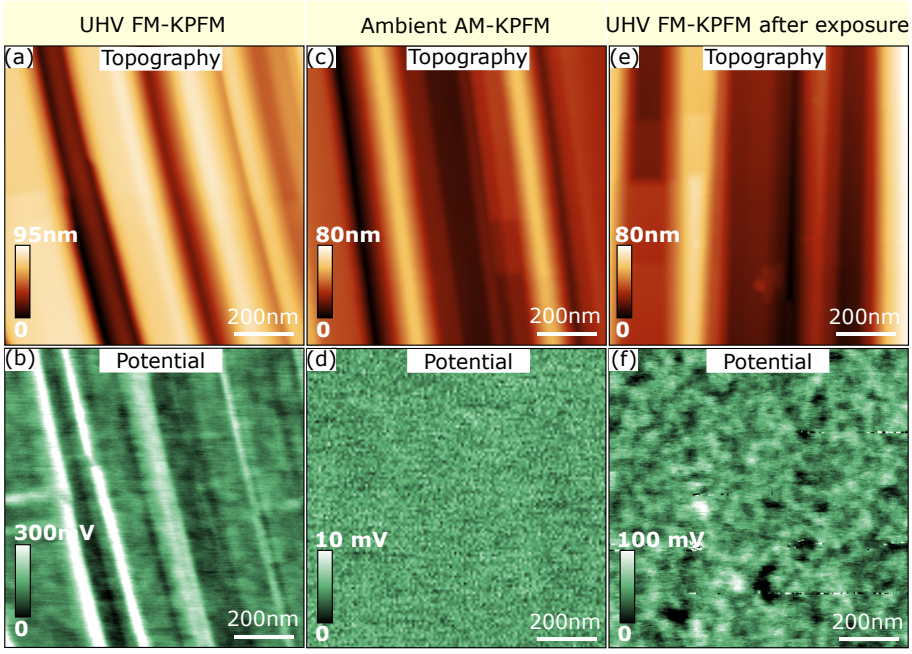

Figure 3.5: The role of environmental conditions on KPFM. (a) FM-KPFM under UHV, (b) AM-KPFM in air, (c) FM-KPFM under UHV after air exposure.

a water layer or even an oxide layer that can homogenize the surface workfunction [164]–[166].

The current setup uses the AM-KPFM lift mode. It means that the separation between the van der Waals force and the electrostatic force is done by retracting the probe a few nanometers from the surface. At a certain height, the main contribution for the total acting force between probe and sample will be solely from the electrostatic contribution. In the presented ambient AM-KPFM measurement, the used lift height was 100 nm. Therefore, one could argue that the absence of surface potential contrast is related to the long distance between probe and sample. To check it, the sample was measured by changing the lift height every 25 pixels of the image. The result is depicted in Figure 3.6, where a surface potential contrast can be observed for small heights and continually vanishes as soon as the height increases. This result suggests that small lift heights would be beneficial to measure the surface workfunction via AM-KPFM. However, as the probe approaches the sample surface, the van der Waals force increases. In other words, more significant is the contribution of topographical artifacts into the KPFM signal [139]. Indeed, the visible contrast for the small lift heights pretty much follows the topography profiles. Note here the differences between the UHV FM-KPFM (Figure 3.5 (b)) case and the current result. On the one hand,

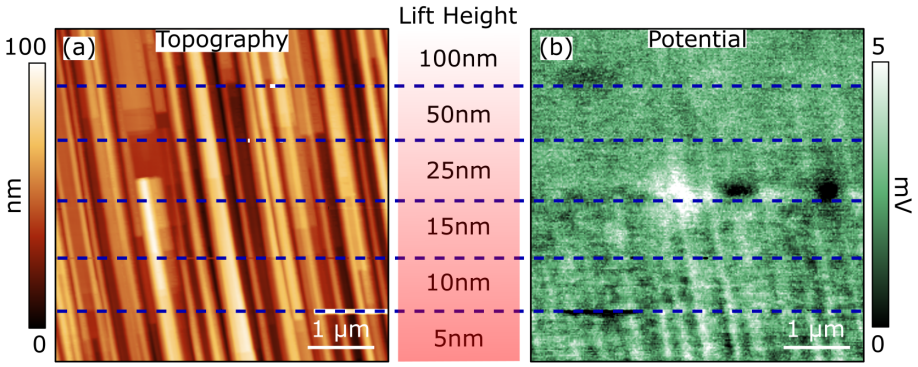

Figure 3.6: AM-KPFM under ambient conditions and changing the lift height every 25 pixels of the image.

the measured FM-KPFM surface potential signal does not necessarily follow the ups and downs of the topography. Specific facets on the sample surface present higher or lower workfunctions. A further discussion regarding the facet-dependent workfunction contrast in the single crystal CIGSe will be presented in Chapter 4. On the other hand, the strength of the signal is also very different, with 300 mV for the FM-KPFM and only 5 mV for the AM-KPFM.

Once again, the AM-KPFM in air and FM-KPFM under UHV conditions yielded different results, similar to the previously observed standard sample study. However, different lift heights in the AM-KPFM mode (Figure 3.6) showed some contrast in the surface potential image, which followed the ups and downs of the topography. The origin of these surface potential contrasts will be discussed in the following sections.

3.3 KPFM measurements on Perovskite absorbers

In the following, results of KPFM applied to GBs of a polycrystalline perovskite absorber will be shown. Similar to the previous section, the sample was measured under UHV FM-KPFM, ambient AM-KPFM, and UHV FM-KPFM after air exposure. The results are depicted in Figure 3.7. The displayed 2μ m $\times$ 2μm images were not acquired at the exact same spot of the sample; however, they were acquired within an area of $\approx 100\mu$ m $\times$ 100μm. Therefore any observed changes should not come from a possible sample heterogeneity. The sample was first measured under UHV using FM-KPFM mode in its pristine state Figure 3.7 (a,d). Transferring from the glovebox

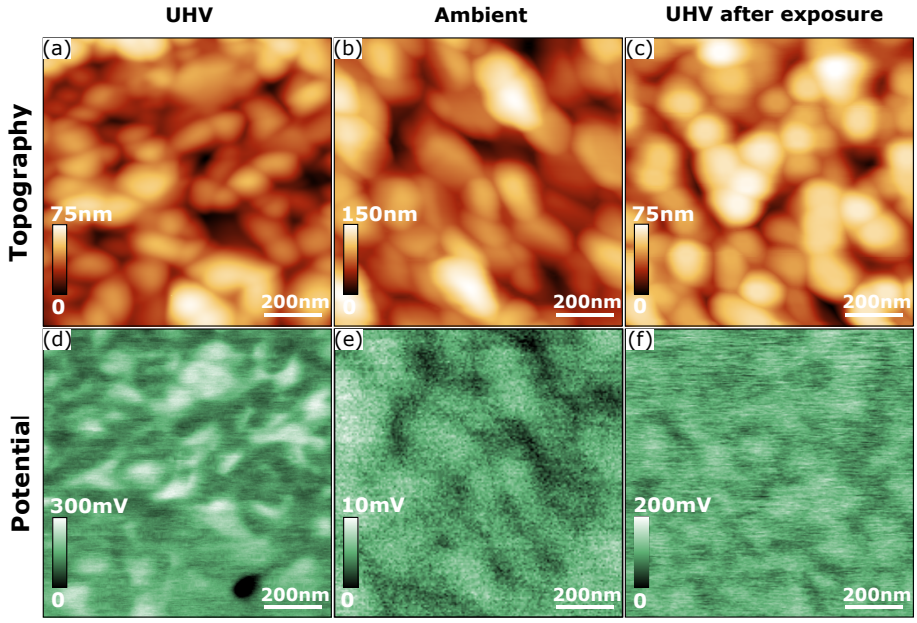

Figure 3.7: Topography (a-c) Surface potential maps (d-f) measured under UHV (FM-KPFM), ambient (AM-KPFM), and UHV (FM-KPFM) after exposing it to air. Figure reproduced with permission from Lanzoni *et al.*, ©(2021) Nano Energy - Elsevier.

to the UHV setup without air exposure was done via the inert gas transfer system. The non-exposed sample, Figure 3.7 (d), shows fluctuations in surface potential of $\approx$ 300 mV. More detailed statistics regarding the region from where this contrast is coming from will be shown in Figure 3.8. The sample was then measured in the ambient AM-KPFM setup, being exposed to air and ambient light for two consecutive days (Figure 3.7 (b,e)). A slight difference in the grain sizes was observed after exposing the samples to air and ambient light, but its origin will not be discussed here as it is not in the scope of this thesis. AM-KPFM under ambient conditions, Figure 3.7 (e), shows a slightly lower contrast, in the order of 10 mV, right at the GBs. Subsequently, the samples were transferred back to the UHV FM-KPFM setup (Figure 3.7 (c,f)). UHV FM-KPFM now shows larger contrasts, partially linked to the GBs, that differ from the pristine sample. As an important note, the observed value of 10 mV for the measurements in AM-KPFM under ambient conditions, although tiny, agrees well with Figure 3.1, where most of the measurements under air and using AM-KPFM operation mode present CPD changes at the GBs ranging from 0 to $\pm$50 mV.

To understand the origin of the observed signal for the non-exposed sample measured under UHV and using FM-KPFM (Figure 3.7 (d)), a few line profiles across the

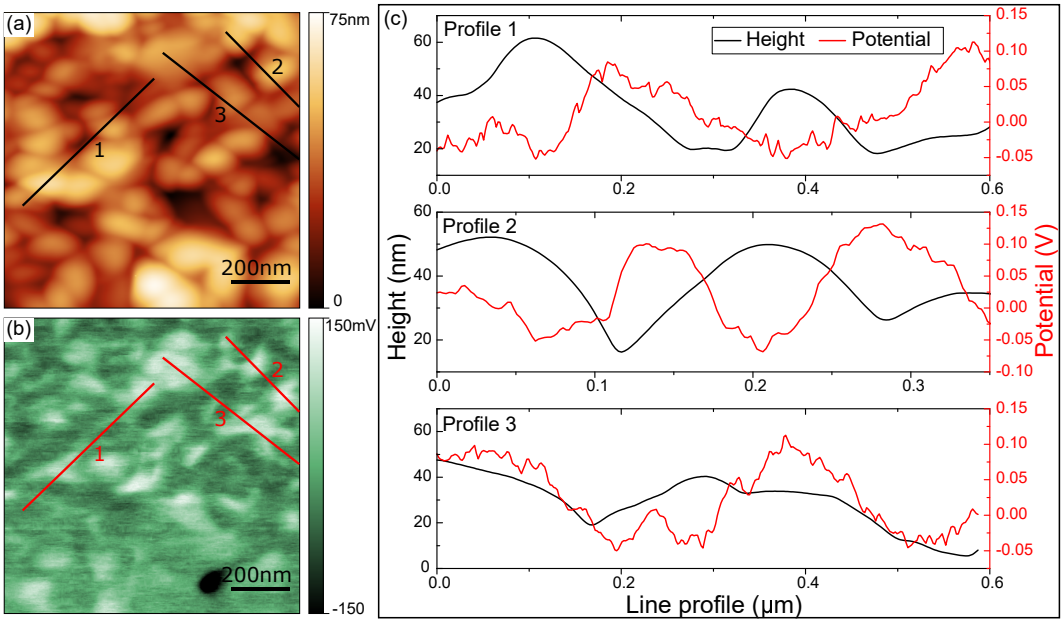

Figure 3.8: Perovskite facet contrast. (a, b) topography and workfunction maps of perovskite. (c) line profiles extracted from the marked regions in (a, b) and showing that workfunction contrasts correlate only with the facet, and no GB contrast is observed. Figure reproduced with permission from Lanzoni *et al.*, ©(2021) Nano Energy - Elsevier.

topographic image and at the equivalent position on the surface potential image were extracted.

The results are depicted in Figure 3.8, where (a) shows the topography, (b) the surface potential, and (c) the extracted line profiles. Three line profiles were extracted from the marked regions in (a) and (b); black lines represent the topography, while the red lines refer to the surface potential. By carefully analyzing the line profiles, one can see that the surface potential contrast comes mainly from the different facets of the perovskite grains. It is expected since there should be different chemical surface termination for each facet of the crystal surface, which leads to different workfunction values [169]. As the scope of this work was a deep understanding of how different KPFM operation modes impact the measured results, the origin of the workfunction changes in the perovskite surface will not be discussed. The main takeover message here is that the main observed changes in workfunction for a fresh non-air exposed perovskite, refer to changes in the facet and not at the GBs.

In the same way, line profiles were extracted from the images acquired under am-

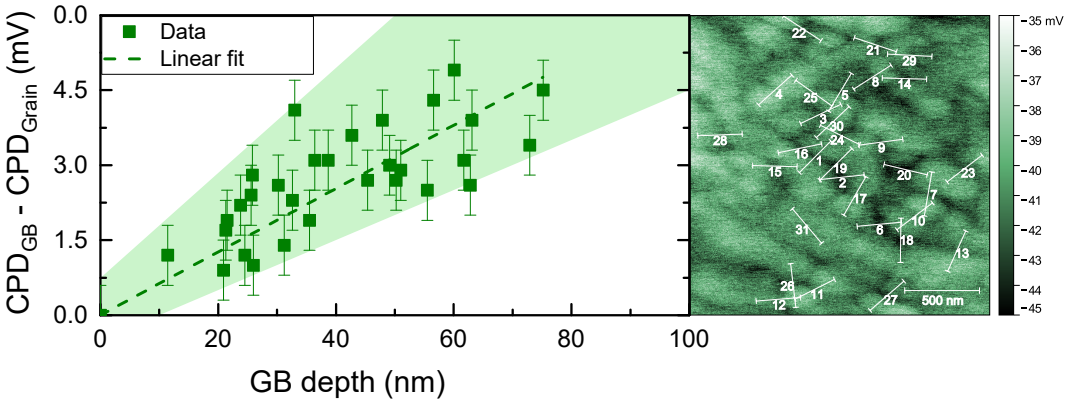

Figure 3.9: CPD vs GB depth in AM-KPFM operation mode. Many line profiles were acquired in the topography and the surface potential maps showing a correlation between the GB depth and the surface potential. This correlation cannot be theoretically explained. Figure reproduced with permission from Lanzoni *et al.*, ©(2021) Nano Energy - Elsevier [160].

bient conditions and using the AM-KPFM operation mode. At this time, the main contribution to the observed contrast in the surface potential image comes from the GB regions. For this reason, 30 GBs line profiles extracted from topography images and their respective surface potential images are analyzed. For each GB, the change in workfunction, $CPD_{GB} - CPD_{Grain}$, is plotted against the change in its depth.

Figure 3.9 depicts this plot and the surface potential map from where line profiles were extracted. Interestingly, a strong linear correlation between the depth and the change in CPD at the GBs (the highlighted green region in the graph) is observed. Such behavior is purely geometrically-related and cannot be explained by distinct electronic properties at the GBs. One should expect that the number of observed charges, consequently the CPD, would be governed by the number of defects and not by the depth of the GBs.

3.4 Splitting forces in AM-KPFM

The results presented in the previous sections showed that by using the same technique but operating it in different modes, one could get different results and, consequently, different interpretations of the data, which could justify the discrepancies observed in the literature concerning the GBs band bendings. FM-KPFM measured

under UHV provided closer results to the tabulated workfunction values, and the same was not observed for AM-KPFM mode under ambient conditions. Also, AM-KPFM mode showed a GB contrast not linked to the GB electronic properties. The origin of the measured contrast at the GB will be discussed in the following.

The total electrostatic force acting between probe and sample can be approximated as the force between two parallel plate capacitors.

$$F_{parallelplate} = -\frac{1}{2}\frac{\partial C}{\partial r}U_{ts}^2 = -\frac{1}{2}\frac{\epsilon_0 A}{(r)^2}U_{ts}^2 \tag{3.1}$$

where $-\frac{1}{2}\frac{\partial C}{\partial r}$ is the derivative of the capacitance over the distance r between the plates, the potential difference between the probe and the sample surface is given as U_{ts}, A is the area of the plates, and ϵ_0 the permittivity.

This electrostatic force can be divided into three contributions: the cantilever, the cone, and the probe apex, as proposed by Wagner *et al.* [146]. Figure 3.10 highlights these three regions in a hypothetical scanning of a positively charged GB. The positive charges at the GB cause a downwards bending of the vacuum level (VL), conduction band (CB), and valence band (VB), leading to workfunction differences between the GB and the surrounding grain.

In analogy to Wagner *et al.* [146], Equation 3.1 can be rewritten to consider the individual contributions from the cantilever (F_{lever}), cone (F_{cone}), and probe apex (F_{apex}), as follow.

$$F_{lever} = -\frac{1}{2}\frac{\epsilon_0 A}{(z+H)^2}U_{ts}^2 \tag{3.2}$$

$$F_{cone} = -\pi\epsilon_0 k^2 U_{ts}^2\left[\ln\frac{H}{z+\tilde{R}} - 1 + \frac{R\cos^2\theta_0/\sin\theta_0}{z+\tilde{R}}\right] \tag{3.3}$$

$$F_{apex} = -\pi\epsilon_0 R U_{ts}^2\left(\frac{1}{z} - \frac{1}{z+\tilde{R}}\right) \tag{3.4}$$

Where H is the cone height, z is the distance between the probe apex and the sample, $k^2 = (\ln\tan\theta_0/2)^{-2}$, $\tilde{R} = R(1-\sin\theta_0)$, R is the apex radius of the probe, θ_0 is the half-open of the cone.

It has been demonstrated that AM-KPFM is sensitive to the electrostatic force, precisely the aforementioned equations 3.2, 3.3, and 3.4, while FM-KPFM is sensitive

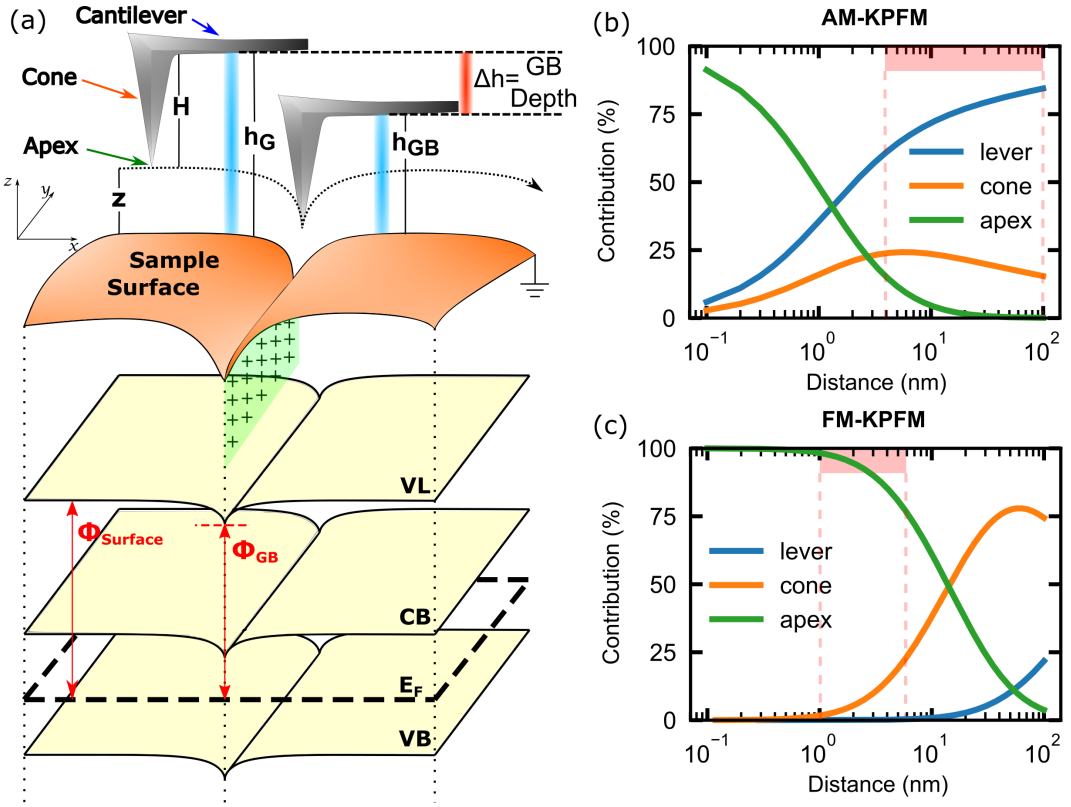

Figure 3.10: Acting forces in KPFM. (a) SPM probe scanning the sample surface at a charged GB. The cantilever, cone, and probe apex are highlighted. When the probe apex enters the GB region, the distance between the cantilever and the sample surface decrease by the GB depth. Positive charges at GB cause a downward band bending of the vacuum level (VL), conduction band (CB), and valence band (VL), and consequently, a workfunction difference will appear. (b) Calculation of the individual contribution of the cantilever, cone, and probe apex to the total measured force in AM-KPFM with respect to the probe/sample distance. Red dashed lines mark the typical range of AM-KPFM operation distance. (c) The same calculation done for the FM-KPFM mode. Figure adapted from Lanzoni *et al.*, ©(2021) Nano Energy - Elsevier [160].

to the gradient of the electrostatic force, the derivative of equations 3.2, 3.3, and 3.4 [144], [148], [167].

The calculated individual electrostatic force contributions in the case of AM-KPFM and FM-KPFM are depicted in Figure 3.10 (b,c). The plot shows the calculated contributions with respect to the distance between the probe apex and sample surface (z), but without considering the mechanical probe oscillation due to the intermittent mode (for considering intermittent mode, see Wagner *et al.* [146]). The red dashed regions highlighted in the graphs are the typical probe sample distances experimentally used for both cases (see subsection 1.7.3). It becomes evident that the force between the cantilever and sample dominates the contribution to the total force measured during AM-KPFM. While in the FM-KPFM case, the stronger contribution comes from the probe apex. This observation is not new in the SPM community [146], but the real impact on complex morphological structures such as GBs was never discussed. In the following, a demonstration of how vital the cantilever contribution is for grain boundary investigation and how it affects the measured surface potential will be addressed.

The first adopted assumption refers to Figure 3.10 (b), where it was proved that AM-KPFM is governed by the electrostatic force between the cantilever and the sample surface.

On the one hand, one can also assume that charges at the GB produce a band bending, resulting in a ΔU_{ts}, or a surface potential difference between the grain and GB. Consequently, it will produce a ΔF_{lever} that can be written as follow:

$$\Delta F_{lever} = -\frac{1}{2}\frac{\epsilon_0 A}{(z+H)^2}\Delta U_{ts}^2 \tag{3.5}$$

On the other hand, as soon as the probe scans the sample at constant distance (z) between the probe apex and the sample surface, changes in topography, e.g., when entering the GB, leads to changes in the distance between the cantilever and the sample. From the sketch in Figure 3.10 (a), this distance goes from h_G, when the probe apex is at the grain, to h_{GB} when the probe apex enters the GB. This change, denoted as Δh, is equal to the GB depth. It allows to rewrite ΔF_{lever} by means of the difference in the force at the grain and the force at the GB:

$$\Delta F_{lever} = -\frac{1}{2}\frac{\epsilon_0 A}{(z+H-\Delta h)})^2 U_{ts}^2 + \frac{1}{2}\frac{\epsilon_0 A}{(z+H)^2}U_{ts}^2 \tag{3.6}$$

Combining Equation 3.5 (ΔF_{lever} due to change in workfunction) and Equation 3.6 (ΔF_{lever} due to change in the distance Δh) results in the following equivalence

$$-\frac{1}{2}\frac{\epsilon_0 A}{(z+H-\Delta h)^2}U_{ts}^2+\frac{1}{2}\frac{\epsilon_0 A}{(z+H)^2}U_{ts}^2\equiv-\frac{1}{2}\frac{\epsilon_0 A}{(z+H)^2}\Delta U_{ts}^2 \tag{3.7}$$

Solving this equation for ΔU_{ts}, one can estimate the apparent change in CPD induced by Δh, when measuring AM-KPFM. In other words, ΔU_{ts} represents the measured ΔF_{lever} due to changes in the capacitive coupling when the cantilever goes up and down while keeping the probe apex/sample distance constant. Thus, the apparent change in CPD, ΔU_{ts}, can be written as

$$\Delta U_{ts}=-U_{ts}\sqrt{\frac{2(z+H)\Delta h-(\Delta h)^2}{(z+H-\Delta h)^2}} \tag{3.8}$$

Usually, experimental values for the parameters within this equation are: average CPD between probe and sample ($U_{ts} = 0.100\,\text{V}$), lift height during KPFM ($z = 50\times10^{-9}\,\text{m}$), the cone height ($H = 12\times10^{-6}\,\text{m}$), and the typical GB depth ($\Delta h = 100\times10^{-9}\,\text{m}$). It leads to an apparent change in the measured surface potential $\Delta U_{ts} = 12.8\,\text{mV}$. This value is very close to the measured surface potential contrast observed for the single-crystalline CISe (Figure 3.5) and perovskite (Figure 3.7, when measured in AM-KPFM).

To consider that each GB has a slightly different depth, the topography acquired during the AM-KPFM was used as an input value for changes in the cantilever-sample distance Δh. The result can be seen in Figure 3.11, where the topography (a), the measured (b), and simulated (c) surface potential are plotted side by side, with their respective extracted line profiles, Figure 3.11 (d). To bring the simulation as close as possible to the real KPFM setup, a random noise of 2 mV peak to peak to the simulated image was also introduced. It is evident that the simulation perfectly matches the experimentally measured AM-KPFM data, where the lower surface potential is observed at the GBs, and higher surface potential is observed in the highest features of the topography.

A similar simulation was done to the AM-KPFM acquired for the single-crystalline CISe sample. Figure 3.12 depicts the measured (a) and the simulated (b) KPFM. Once again, the extracted line profiles (c) show that the simulated data impressively

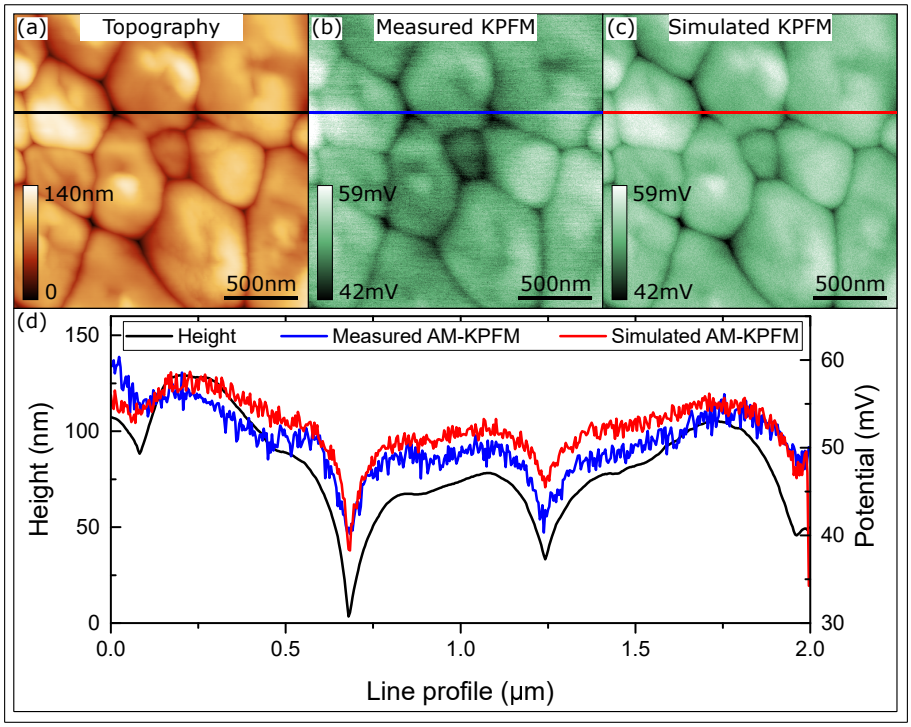

Figure 3.11: AM-KPFM simulation: (a) measured topography, (b) measured surface potential, and (c) simulated surface potential. Figure reproduced with permission from Lanzoni *et al.*, ©(2021) Nano Energy - Elsevier [160].

describes the measured KPFM data.

It is essential to remember that Equation 3.8, used in this simulation, considers only physical changes in the cantilever/sample distance and no electrostatic force due to charges at the GB. Furthermore, Equation 3.8 shows an interesting link between ΔU_{ts} and U_{ts}: The sign of ΔU_{ts} (apparent downward or upward band bending) depends heavily on the sign of U_{ts} (average CPD between probe and sample). In other words, if the probe's workfunction is smaller than the sample's average workfunction (U_{ts} is positive), the apparent GB contrast will be darker. This is the condition observed in Figure 3.11. But if the probe's workfunction is greater than the sample's average workfunction (U_{ts} is negative), the apparent GB contrast would be brighter. In practice, this means that if a sample with an average work function of 4.9 eV is measured in AM-KPFM with a Pt/Ir probe (4.8 eV), a brighter contrast at the GBs is expected. But if the same sample is measured with an Au-coated probe (5.1 eV), a

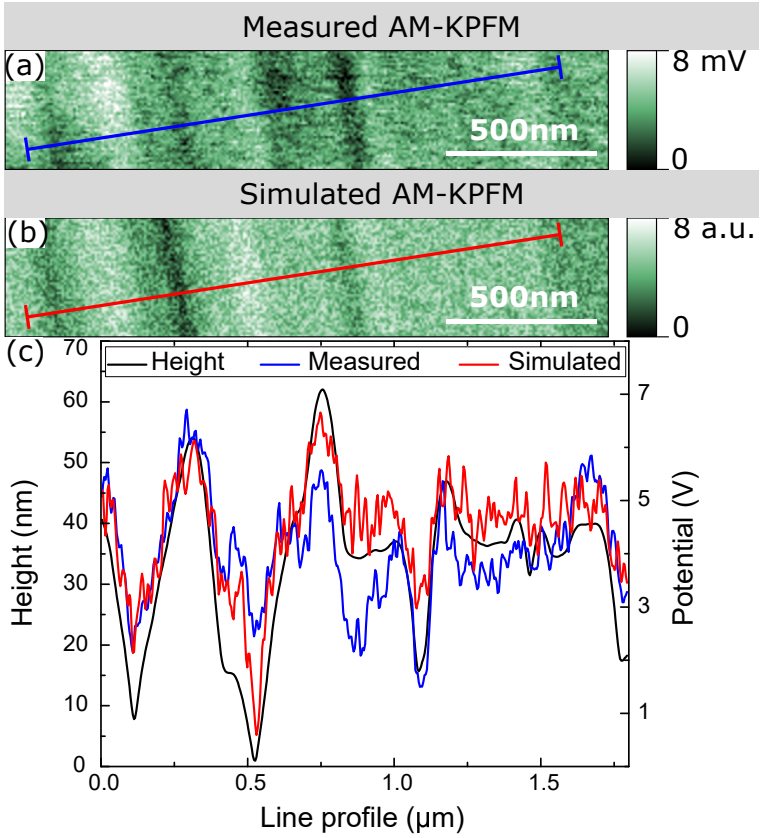

Figure 3.12: AM-KPFM simulation: (a) measured topography, (b) measured surface potential, and (c) simulated surface potential. Figure adapted from Lanzoni *et al.*, ©(2021) Nano Energy - Elsevier [160].

darker contrast at the GBs is then expected.

3.5 Chapter summary

The use of different kinds of samples and simulations showed that the electrostatic force in AM-KPFM, which is governed by the cantilever/sample interaction, can result in a strong topographic cross-talk artifact. These artifacts are very dependent on the sample roughness, leading to more issues when measuring rough surfaces, such as polycrystalline solar cells. The results showed that an inaccurate interpretation of the GB properties could happen when KPFM is measured in amplitude modulation KPFM. On top of that, upward or downward band bending resulting from this cross-talk artifact is just a matter of the average workfunction difference between probe and sample. If $\Phi_{sample} - \Phi_{probe}$ is a positive value, it results in a downward band bending and vice-versa.

In the opposite direction, FM-KPFM, which has the main contribution to the measured electrostatic force coming from the probe apex, showed reproducible results with no topography cross-talk artifacts when operating under UHV conditions. During this thesis, FM-KPFM operation mode under UHV will be the only method used for workfunction evaluations and conclusions regarding GBs properties. AM-KPFM will be used only when the average workfunction is needed, and no GB conclusions are taken.

Chapter 4

Properties of single-crystalline CISe absorber grown on GaAs (100)

Some of the results in this chapter are published in the contribution Lanzoni *et al.* [170].

To properly understand the GB properties of the CIGSe sample grown on GaAs substrates, it is essential to investigate earlier the electronic properties of the sample in its simplest form. For this, a CISe sample grown on GaAs (100), meaning no Ga and no GB, will be the first study case. In this chapter, the surface properties of the epitaxial CISe will be investigated employing SPM techniques. Details on the used criteria for choosing the most appropriate and reliable CIGSe sample for the current study will be described in this chapter.

4.1 Prior investigations of the CISe surface

A sample series was grown via MOVPE on (100) semi-insulating GaAs wafers by changing its Cu content. The details regarding sample preparation are described in Chapter 2. The entire set of samples was a Cu-rich absorber where CGI ranges from 1.10 to 1.95 as measured via EDX.

The initial goal of preparing this set of samples was to identify which chemical composition would lead to samples compatible with the KPFM setup under UHV conditions. As a reminder, under UHV, topography and surface potential data are acquired in frequency modulation (please refer to section 1.7 and Chapter 3). It results in a minimal probe/sample distance, ranging from 2 to 15 nm, limiting the

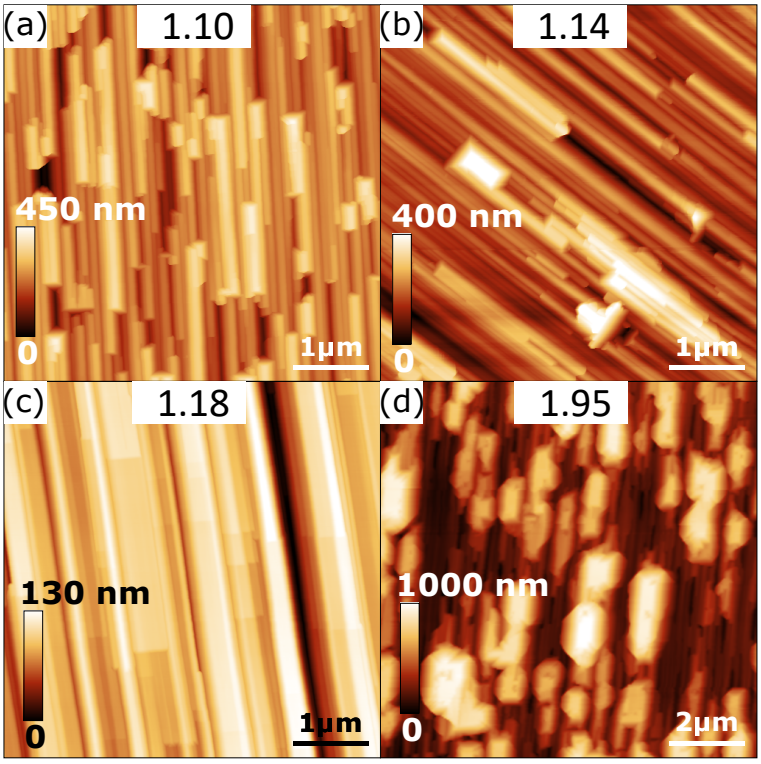

Figure 4.1: Topography acquired via AFM of the Cu-rich CISe sample series. The samples are labeled according to their CGI ratio measured via EDX (a) 1.10, (b) 1.14, (c)1.18, (d) 1.95

measurements to a flat surface only. In other words, if the difference in height from one pixel to another in the AFM image is larger than 15 nm, the AFM will fail to track the feedback signal, and the probe will touch the surface. UHV machines usually have a mechanism to protect the probe, which consists of retracting the probe if the feedback error exceeds a user-specified limit; in the SPM community, this is called "tip jumps". This effect does not occur in intermittent contact mode AFM, where the probe intermittently touches the surface. For this reason, before investigating the sample under UHV, an initial investigation of its topography was done via intermittent contact AFM under ambient conditions. The measured topographies of this sample series are depicted in Figure 4.1. The images are labeled concerning their CGI ratio.

All the samples were supposed to have the same thickness, where the change in roughness can be attributed exclusively to compositional changes. Indeed, by changing the Cu content, very distinct morphologies were observed. The sample with the lower Cu content presented stronger faceting, leading to a considerable roughness on the surface, as seen in the scale bar (Figure 4.1 (a)). By increasing the Cu content, the

faceting reduces, and flatter samples can be produced (Figure 4.1 (b) and (c)). This effect was previously observed by Siebentritt *et al.* [48], and it is associated with the lower surface energy of the (112) surface, which changes according to the Cu-content. However, further increase in the Cu content results in huge material agglomerations on the sample surface (Figure 4.1 (d)), which can be attributed to Cu_xSe secondary phase. Indeed, these observed structures are very similar to the previous observation from Fons *et al.* [171], where they could directly observe the Cu_xSe structures on Cu-rich CISe via Two-dimensional reciprocal space x-ray mapping.

This preliminary study aimed at identifying the Cu-content that leads to a flatter surface, and in this aspect, the sample with a CGI = 1.18 (Figure 4.1 (c)) was identified as the most suitable one. This sample is a 500 nm absorber with a peak-to-peak roughness of around 130 nm, and it will be called from now on as **Cu-rich CISe**.

Similar to the higher Cu content sample (CGI = 1.95), material agglomerations were also observed on the surface of the chosen Cu-rich CISe (CGI = 1.18) but in fewer amounts. Figure 4.2 shows the SEM (a,b) and the AFM (c) images of such agglomeration. It was possible to see in the SEM images that the CISe material form trenches well-aligned in the [110] direction, whereas the agglomerated material does not follow any preferential growth direction. This is another piece of evidence for the Cu_xSe formation; since its lattice parameters do not match the ones of CIGSe [49], [172], polycrystalline growth is expected. Figure 4.2 (c) depicts the topography of these structures, evidencing that they can form structures as higher as 3 μm. Additional Raman measurements reveal peaks that do not match the ones from CISe (see Appendix A.5), confirming a distinct composition of these structures.

The typical procedure to remove Cu_xSe secondary phase from the absorber surface is by etching it with a KCN solution [173], [174]. Here, a 10% wt KCN solution was used for 5 minutes. Figure 4.3 depicts the SEM and AFM images before and after the KCN etching.

From the as-grown sample (Figure 4.3(a)), a more significant material agglomeration is observed over the surface compared to the same sample after 5 minutes of KCN etching. Prolonged etching times do not entirely remove the structures, although they were further reduced. This fact can be attributed to the size of the Cu_xSe grains, which would require extended etching times to complete remove the agglom-

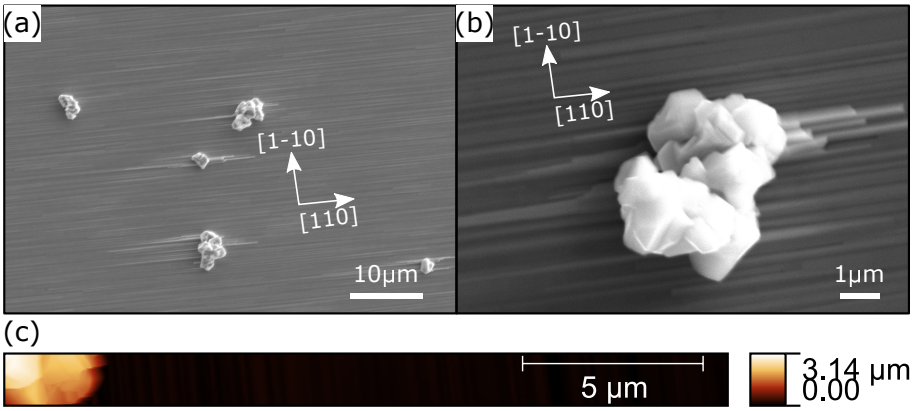

Figure 4.2: (a, b)SEM maps of the large area of the Cu-rich CISe sample showing some material agglomeration on the surface. (c) topography acquired via AFM.

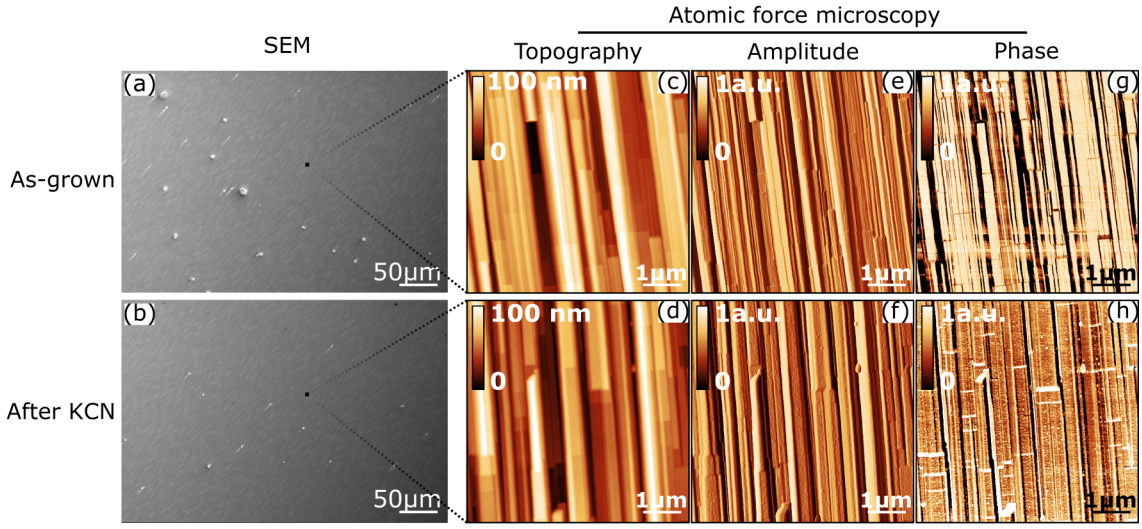

Figure 4.3: KCN treatment of the Cu-rich CISe absorber. (a,b) SEM image showing the reduction in the amount of the agglomerated structures on the surface after KCN etching. (c,d) topography images of the CISe surface before and after KCN. (e,f) amplitude images (also called error signals) where an easier visualization of small structures formed after KCN is possible. (g,f) phase-contrast images evidencing that the mechanical or electrical properties of the small structures are distinct from the CISe pristine absorber. Figure reproduced with permission from Lanzoni *et al.*, ©(2019) IEEE [170].

erated material. Figure 4.3 (c-h) shows the topography, amplitude, and phase images (for more information regarding phase-contrast images, see Chapter 1) acquired via intermittent contact mode AFM under ambient conditions for the as-grown (c, e, g) and KCN etched samples (d, f, h). From the topography images (Figure 4.3 (c,d)), a visible change in the sample morphology after the KCN was not observed. Note that the images were not acquired at the exact same spot, but the morphology from one is quite similar to the other.

However, the amplitude and the phase-contrast images showed the presence of small structures (in the range of $\approx 2\,\text{nm}$) on the KCN etched sample surface (Figure 4.3 (f, h)). Additionally, the phase-contrast image (Figure 4.3 (g-h)) suggests that a material with different mechanical and/or electrical properties is present at the sample surface, which can be attributed to remaining particles from the KCN etching process. It is worth reminding that these measurements were carried out under ambient conditions, meaning that an oxidation process could occur. These results showed that KCN etching modifies the sample surface of the pristine sample, which is in accordance with previous results where Se-related acceptor defects near the surface of Cu-rich CISe absorbers were already observed [82], [175]. However, these results proved that, except for the agglomerated structures, the remaining surface fits well the UHV KPFM requirement of a CIGSe absorber with low surface corrugation, and no additional KCN treatment is needed for further electrostatics experiments.

4.2 Facet dependence workfunction

In section 3.2, it was already mentioned that some well-oriented trenches were present on the sample surface of the CISe. Back there, it was observed that some of the facets showed higher workfunction values than others. A previous report on the epitaxial growth of CIGSe on GaAs(100) had already shown that a highly textured surface could be formed [48], [176]. The explanation is the preferential growth direction triggered by the lower energy formation of the polar (112) facets compared to the (100) [48], [168], [176]. As a result, trenches aligned in the [110] direction, such as the one observed in Figure 4.4 (a), is formed on the sample surface. Interestingly, some of the generated facets display higher workfunction values, as shown in Figure 4.4 (b).

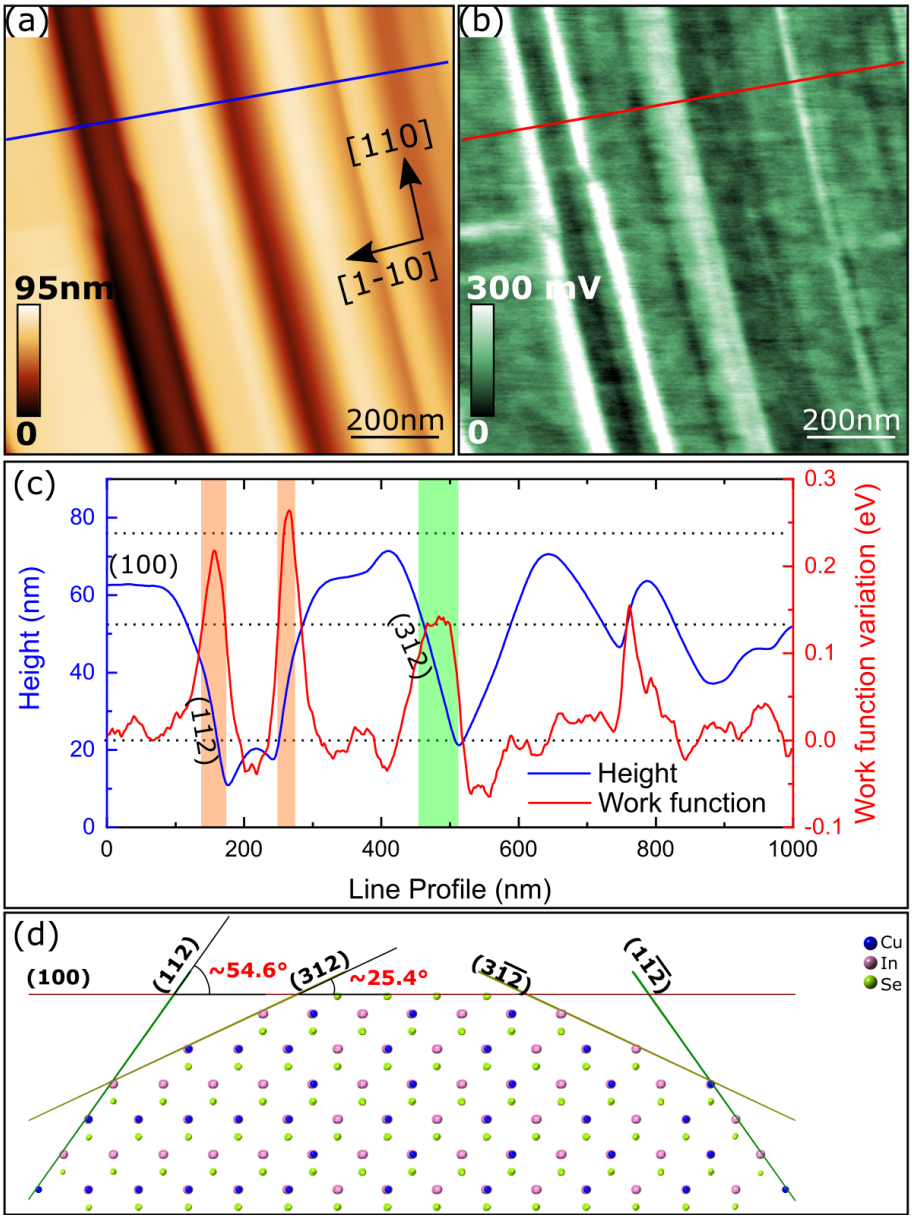

Figure 4.4: Facet dependence workfunction. (a) topography and (b) surface potential map of the Cu-rich CISe sample. (c) line profile extracted from the blue and red lines, topography, and surface potential images, respectively. The line profile shows a facet dependence workfunction. (d) shows the CISe crystal structure with the angles formed between the (100), (112), and (312) facets. Figure adapted with permission from Lanzoni *et al.*, ©(2019) IEEE [170].

The correlation between the changes in workfunction and the facets is better visualized in the line profiles shown in Figure 4.4 (c). The line profiles represent the topography (blue) and the workfunction differences (red) extracted from the corresponding marked regions in Figure 4.4 (a) and (b), respectively. The blue line profile (topography) shows a flat plateau that was assumed to be parallel to the GaAs (100) surface. By measuring the angle between the (100) and the other surfaces, one can calculate the orientation of the unknown facets. Two major angles were found, $27° \pm 11°$ and $54° \pm 4°$. The measured values are very close to the expected angles from the planes (312) and (112)/($1\overline{1}\overline{2}$)) respectively (see Figure 4.4 (d)). These regions are marked in Figure 4.4 (c) by orange, representing the plane (112)/($1\overline{1}\overline{2}$), and green representing the plane (312). The polar facets (112) are widely reported in the literature, being the most energetically favorable orientation for CIGSe absorbers. An apparent and well-localized change in workfunction of ≈ 200 meV between the polar (112)/($1\overline{1}\overline{2}$) and the (100) facets was observed. These differences in workfunction are well justified by the different surface terminations in each facet. Indeed, Figure 4.4 (d) depicts the different atomic arrangements expected for each facet, where distinct surface termination is observed between the facets. A slight difference in workfunction was also observed between the (112) and ($1\overline{1}\overline{2}$) facets. These differences are attributed to the also widely reported ($1\overline{1}\overline{2}$)-Se and (112)-metal terminated facets [48], [84], [168].

Contrary, the (312) facet was never reported in the literature, and besides the theoretical angle fitting quite well with the experimentally measured angle, it might not be the correct description here. Perhaps, the measured angle could be a stair-like convolution of the (100) and (112) facets. Remember that the KPFM probe radius is ≈ 25 nm, meaning the observed topography is a 25 nm convolution between probe and sample. If a stair-like morphology smaller than 25 nm is formed, one may not see either the facet (112) or the (100), but a convolution between them. Consequently, there will also be a convolution of their respective workfunction values. It explains why the "(312) facet" had a larger scatter of the measured angles (from 20° to 40°) and the workfunction (from 50 meV to 150 meV). The (112) facets show a minor scatter of the workfunction, due to whether the surface is Se or metal terminated. Still, the measured angle is quite reliable (always between 50° and 58°). Errors on the measured angle are expected, and they range from piezo creep/hysteresis that affects lateral and

horizontal movements of the piezo [150, (see chapter 6: Artifacts in SPM)], up to the leveling post-treatment of the images, where the (100) reference is not well aligned [177]. Nevertheless, within the same image, one should not expect the measurement to vary 20° in one facet and 8° in the other.

Additionally, slight fluctuations in the workfunction of $\approx 50\,\text{meV}$ are also present on the image and visible in Figure 4.4 (c). These small fluctuations in the workfunction can be associated with two main factors; the presence of other facets or defects within the same facet.

4.3 Chapter summary

In this chapter, the identification of reliable sample surfaces for UHV KPFM measurements was presented. Varying the Cu content of the absorber led to different morphologies on the surface due to trenches formation. These trenches are related to a well-reported favorable (112) facet formation compared to the (100) facet. Indeed, the direct measurements of the angles formed with respect to the (100) surface revealed the presence of the (112) facet on the surface. It was also shown that these (112) facets presented a higher workfunction value than the other facets. In conclusion, even for the single-crystalline CISe without any PDT, the appearance of different surface termination led to workfunction changes at the surface that can influence band bendings and consequently should be considered when preparing a solar cell device.

Chapter 5

Properties of CIGSe absorber epitaxially grown on multi-crystalline GaAs substrate

The previous chapter showed the results of single-crystalline CISe epitaxially grown on GaAs (100). Even in the presumably simplest case of thin-film CISe (no Ga, no GB), workfunction contrasts of $\approx 250\,\mathrm{mV}$ were observed in the sample surface due to faceting. The results of the CIGSe grown on multi-crystalline GaAs substrate will be discussed in the current chapter. It will be shown that this approach leads to some advantages regarding the grain boundary characterization, where individual GBs can be quickly investigated before and after PDTs.

5.1 The multi-crystalline GaAs substrate

The multi-crystalline GaAs substrate contains many macroscopic grains, each oriented in some specific direction. Figure 5.1 (a) shows a picture of the 2-inch multi-crystalline GaAs substrate, where the naked eye can easily see different grains. Figure 5.1 (b) depicts the EBSD map from a sister substrate. Each color in the EBSD map represents a different grain orientation.

Such substrate is commercially available and epi-ready, meaning epitaxial growth can be performed on its surface. Additional technical specifications regarding the substrate can be found in Chapter 2. However, before growing CIGSe on these sub-

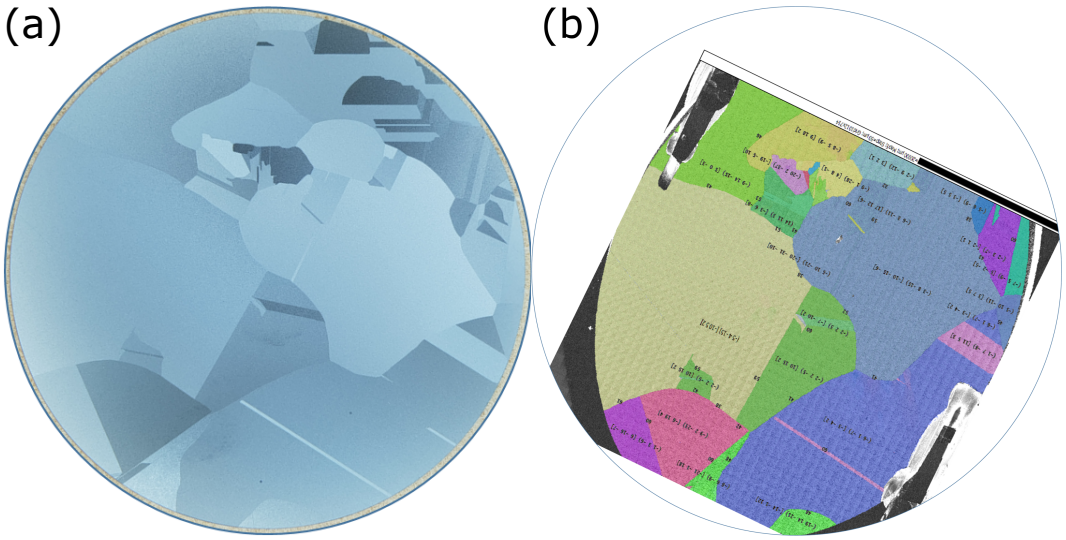

Figure 5.1: Multi-crystalline GaAs substrate: (a) picture of the 2-inch GaAs substrate. (b) EBSD map from a sister substrate.

strates, the surface was investigated via AFM. The goal was to identify possible complex structures at the GBs that would make the epitaxial growth impossible.

Twenty-six different GBs were measured on this substrate, where the topographies can be summarized by the two regions depicted in Figure 5.2. GBs with a significant height change was found, as observed in Figure 5.2 (a). The image shows the topography of a large scanned area ($80\,\mu$m $\times$ $80\,\mu$m) measured via AFM and its respective extracted line profile in the bottom. Changes in height from one grain to the other of ≈ 50 nm can be observed. These changes are expected since the polishing can act differently depending on the surface termination [178]. Besides the relatively big step observed in the larger scan area image, a maximum step height of $\approx 2\,nm$ was observed right at the GB. Figure 5.2 (b) shows a $3\,\mu$m $\times$ $3\,\mu$m topographic image of the GB region with 3 line profiles across the GBs, where the ≈ 2 nm is shown. Many small particles are also observed on the surface, which is attributed to dust due to mishandling of the sample; such particles should not be present on the epi-ready substrates. The changes in height observed in this multi-crystalline GaAs substrate should not be a problem for epitaxial growth even at the GB. However, in the close vicinity of the GB, the presence of a step height combined with a slight mismatch between GaAs and the CIGSe could lead to a strain gradient from the GB to the grain.

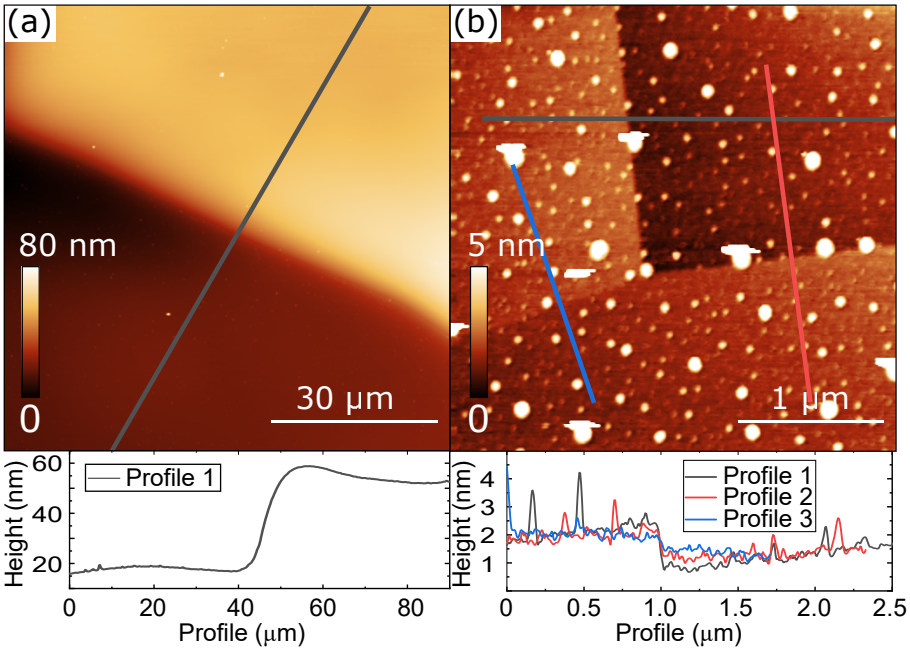

Figure 5.2: GBs of the multi-crystalline GaAs substrate: (a) 80 μm × 80 μm topographic image of the GB region with a line profile. (b) 3 μm × 3 μm topographic image showing 3 GBs and their respective line profiles.

5.2 Surface characterization of CIGSe grown on multi-crystalline GaAs substrate

Before any electrostatic characterization of the CIGSe epitaxially grown on multi-crystalline GaAs substrate, the surface morphology was investigated. Once again, issues during KPFM measured under UHV are expected if the topography is too rough (see tables 1.1 and 1.2). Indeed, by growing 500 nm of CIGSe on the multi-crystalline substrate, a few grains showed rough topographies that made the measurement impossible. For this reason, the CIGSe thickness was reduced to 200 nm by decreasing the deposition time during growth. Besides the 200 nm thickness not being the standard thickness for the solar cell absorber, the reduced thickness was necessary to obtain flatter surfaces. Details on the sample growth can be found in Chapter 2.

The SEM map from Figure 5.3 (a) shows an overview of the sample surface, where many grains and GBs are present. Increasing the SEM magnification shows that different structures are formed depending on the grain orientation. Few grains produced trenches, similar to those observed for the CISe sample grown on GaAs (100) (see Chapter 4). The trench-like structures are aligned in roughly the same direction over

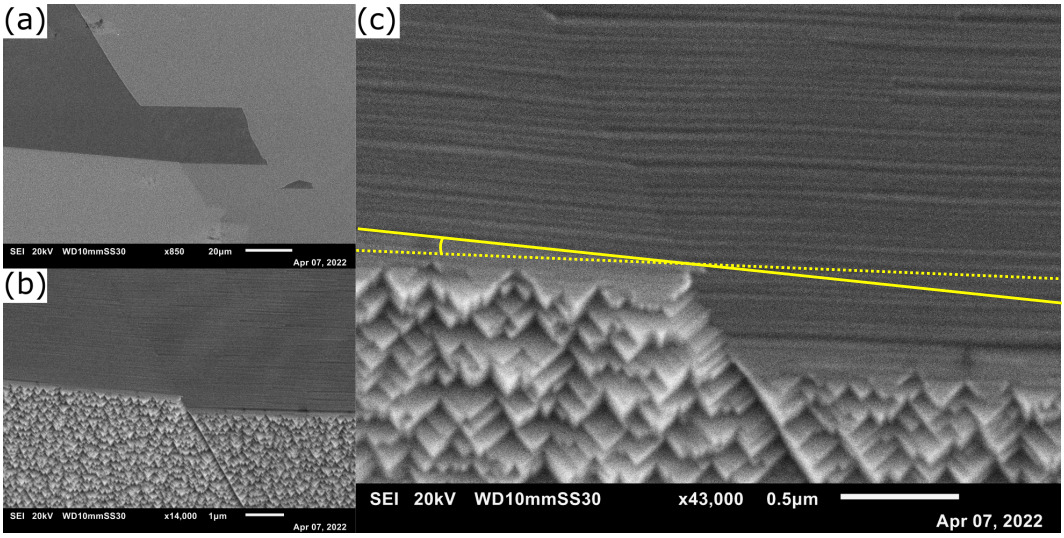

Figure 5.3: SEM overview of the CIGSe sample epitaxially grown on multi-crystalline GaAs substrate. Different morphologies are macroscopically visible in the larger images (a) and (b). A characteristic pyramid-like and trench-like structures are visible in the high-resolution scan (c), showing the GB interfaces between 4 different grains. Yellow lines highlight a small tilt between the formed structures.

the surface, but it is not possible to say from the SEM images whether they have the same [110] orientation observed in the GaAs (100) case. Indeed, careful observation of Figure 5.3 (c) indicates a slight angle between the trenches' direction from one grain to the other.

Furthermore, a pyramid-like structure is formed for a few grain orientations. The pyramids always grow perpendicular or parallel to the trench-like structures, with no other angles formed between them. The result is the appearance of flat triangular facets, as observed in Figure 5.3 (c). From the SEM images, no microscopic fissures are observed at the GB.

Figure 5.4 depicts AFM topographies of the different types of GBs. These images were acquired in non-contact mode AFM under N_2 environment without exposing the sample surface to the air. Similar to the SEM images, the trench-like and pyramid-like structures are visible. The scale bar of the images shows heights of up 300 nm within the scanned area, which can be a problem when measuring this sample in UHV. The surface roughness changes according to the substrate's grain orientation. The trench-like structures can present very flat surfaces, with very smooth GBs, like the one on the right side of Figure 5.4 (c), while the GBs between the trench-like and pyramid-like

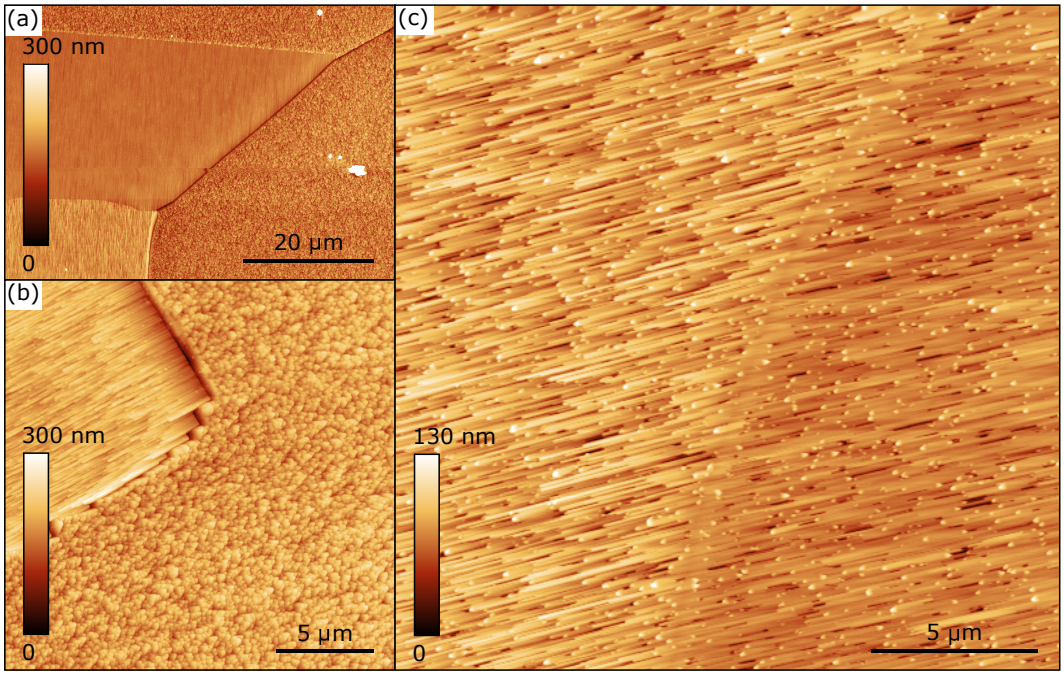

Figure 5.4: GBs in the CIGSe epitaxially grown on multi-crystalline GaAs substrate: (a) 80 μm × 80 μm topographic image of the GB. (b) 20 μm × 20 μm topographic image showing different grains and GBs. (c) 20 μm × 20 μm topographic image showing a very smooth GB.

structures can be very rough or smooth depending on the adjacent grain orientation.

The angle formed between the facets in the pyramid-like structures and the horizontal flat surface of the trench-like structures has an average value in the order of $\approx 15° \pm 5°$, which is not close to the 54° measured in Chapter 4 between the {112} and (100) surfaces. This is expected since now it could be that the surface does not have a (100) termination. However, as the {112} facets are known to have the most favorable formation, the triangular and the trench facets are most likely to be the {112}. Additional EBSD measurements would be necessary to conclude it. Despite everything, these are the two types of morphology formed all over the sample surface, flatter or rougher, or forming smother or rougher GBs interfaces depending on the substrate grain orientation.

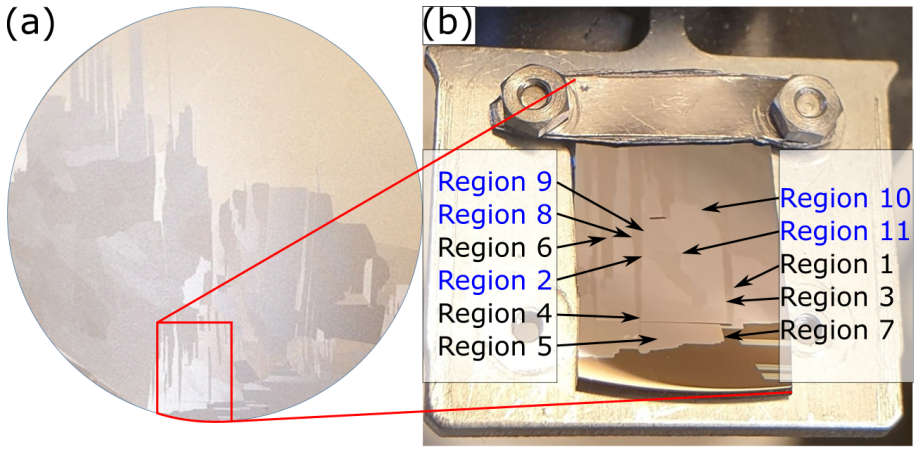

Figure 5.5: CIGSe sample epitaxially grown multi-crystalline GaAs substrate. (a) Picture of the 2-inch sample. (b) Picture of the small piece of the sample mounted in the UHV AFM sample holder and showing the regions of interest.

5.3 Grain boundary characterization of the CIGSe absorber epitaxially grown on multi-crystalline GaAs substrate

The previous section has shown that CIGSe absorber epitaxially grown on multi-crystalline GaAs substrate presents distinct topography depending on the grain orientation, producing rough surfaces. This section will show an exploratory UHV KPFM study on this sample. The sample was transferred from the MOVPE to the UHV KPFM setup without air exposure. XPS data (discussed further in Figure 5.12) confirmed that the surface was oxygen-free, indicating a smooth transfer.

5.3.1 As-grown sample

The CIGSe thin film was grown on a 2-inch substrate and was cut into a small piece for the UHV KPFM characterization. Figure 5.5 (a) depicts an overview of the 2-inch CIGSe grown on multi-crystalline GaAs substrate, and Figure 5.5 (b) a small piece mounted on the UHV sample holder. Figure 5.5 (b) also highlights the different regions measured in this sample. Even though the sample thickness was reduced, a few regions were still too rough for the UHV measurements, and they will not be shown here (labeled in black).

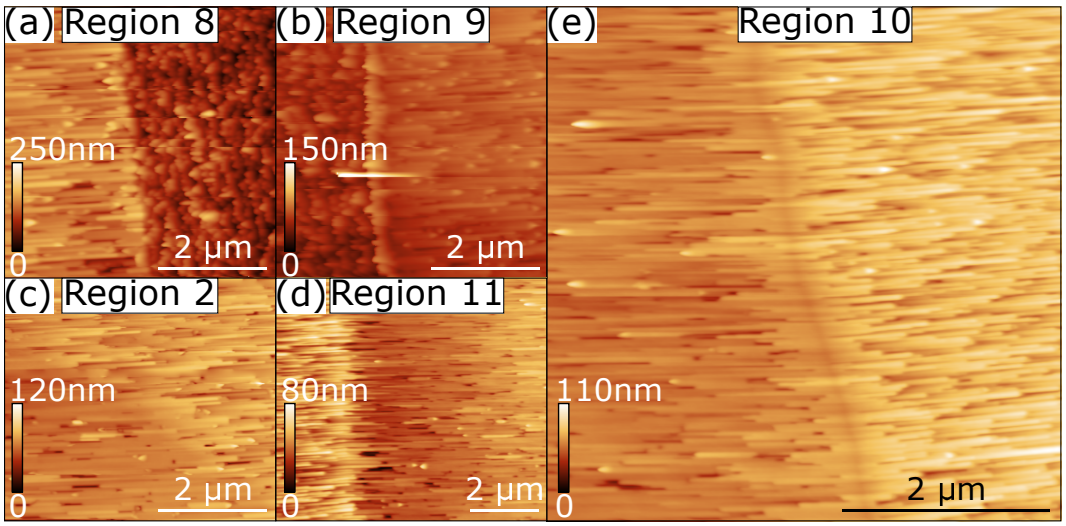

Figure 5.6: AFM topography images of GBs in the CIGSe absorber epitaxially grown on multi-crystalline GaAs substrate. (a-e) regions labeled with blue color in Figure 5.5.

Nevertheless, different GBs were possible to investigate and are labeled in blue color in Figure 5.5 (b). These regions are also macroscopically marked in Figure 5.5 (b), and the equivalent topographies are displayed in Figure 5.6 (b).

Each region highlighted in Figure 5.6 has its peculiarities regarding the GB interface. For example, region 8 has the pyramid apex pointing towards the trench-like structures. While in region 9, the pyramid has an inverted direction, from the trench-like to the pyramid-like structures, creating a smooth GB interface. Regarding the GB formed at the interface between trench-like grains, a condition where a very smooth GB is formed is presented in region 2. A condition where the morphology slightly changes right at the GB is visible in regions 10 and 11.

Figure 5.7 depicts the KPFM data acquired simultaneously with the topography images shown in Figure 5.6. The data was converted to display the workfunction values, where the average value between all the images is $\approx 4.35\,\text{eV} \pm 0.1\,\text{eV}$. As a general rule, a workfunction difference between the grains was visible. This difference is expected since different surface termination would lead to different workfunction values. Another general rule, no clear GB contrast is observed.

Figure 5.7 (a,b) depicts the workfunction map at the GBs formed between the pyramid- (brighter contrast) and trench-like (darker contrast) structures, while the remaining (Figure 5.7 (c - e)) depicts the workfunction map at the GBs formed between two trench-like structures.

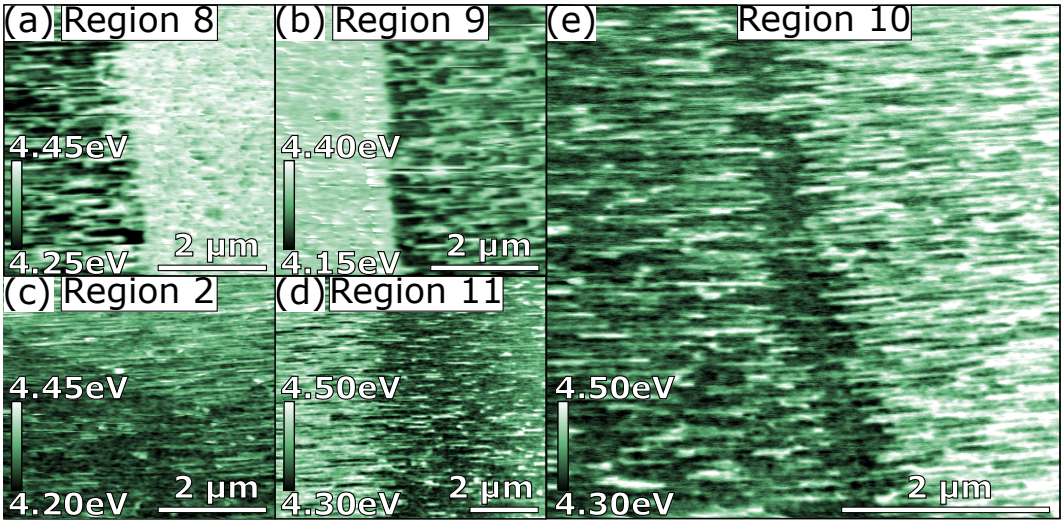

Figure 5.7: FM-KPFM workfunction images of GBs in the CIGSe absorber epitaxially grown on multi-crystalline GaAs substrate. (a-e) regions labeled with blue color in Figure 5.5.

From Figure 5.7 (a,b), one can see that the pyramid-like structures (brighter contrast) show a higher workfunction value (4.41 eV) and are pretty homogeneous (root mean square (RMS) equal to 19.1 meV), which indicates a single surface orientation.

The same uniform workfunction value was not observed for the trench-like structures (darker contrasts in Figure 5.7 (a,b)), where the measured workfunction value was 4.32 eV with RMS of 46 meV. The scattering in the workfunction values is due to faceting in the trench-like structures.

Figure 5.8 shows a more detailed discussion of Figure 5.7 (a). Dashed squares in Figure 5.8 (a) mark the areas selected for the statistical distribution in which the pyramid-like and the trench-like structures are ascribed to the blue and green squares, respectively. Figure 5.8 (b) shows the statistical distribution of the workfunction values for the trench-like (upper graph) and pyramid-like (bottom graph) structures. It immediately shows that most of the workfunction values in the pyramid-like structures are confined in one single Gaussian peak, while the distribution for trench-like structures is much broader. Three main workfunction values were found for the trench-like structure: 4.29 eV, 4.36 eV, and 4.41 eV, as shown by the three Gaussian fits in Figure 5.8 (b up). It confirms at least two different facets of the trench-like structures. Interesting, the workfunction value of 4.41 eV, coincides with the main workfunction value observed in the distribution from the pyramid-like structures Figure 5.8 (b down),

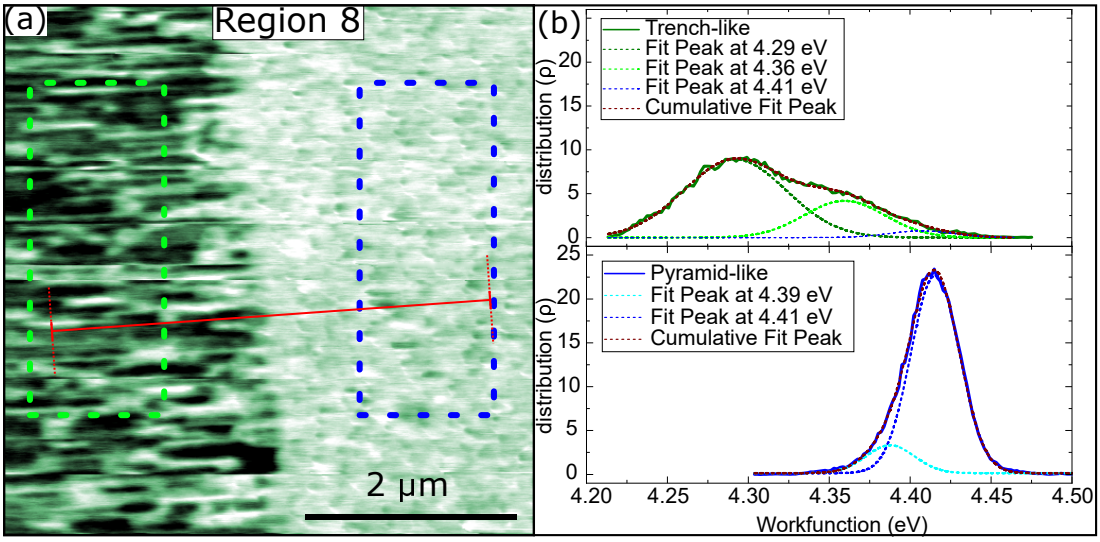

Figure 5.8: (a) KPFM image acquired in region 8 of the CIGSe sample. The colored dashed squares indicate the areas used for the statistical workfunction distribution plotted in (b). The upper graph shows the workfunction distribution for the trench-like structures with three Gaussian fitting at positions 4.29 eV, 4.36 eV, and 4.41 eV. The bottom graph shows the workfunction distribution for the pyramid-like structures with two Gaussian fitting at positions 4.29 eV, 4.39 eV, and 4.41 eV

suggesting the {112} facets since it is the most energetically favorable surface in the CIGSe absorber [47], [48], [84], [168], [179]. Besides the excellent agreement, only the AFM topography and workfunction values are not enough arguments to state that this fact is actually true. Additional EBSD measurements would be necessary to confirm the {112} facets.

Despite the changes in workfunction according to the surface orientation, no visible workfunction contrast was observed at the GB. Nevertheless, line profiles were extracted (red line in Figure 5.8 (a)) at the GB region. Figure 5.9 depicts the extracted line profiles, where a single and the average of 128 lines are plotted. With a single line profile (red curve called "1 line" workfunction), a slight decrease in workfunction right at the GB ($\approx 10\,mV$) is observed. This decrease could be associated with a downward band bending at the GB due to charge accumulation [86]–[89]. However, it could also be associated with a noise signal (KPFM noise level is $\approx 5\,mV$), a new facet close to GB, or even a kind of probe/sample convolution between the two different surfaces, similar to the CISe grown on the GaAs (100) substrate (see the Figure 4.4). A careful analysis of the equivalent topography height profile (black curve "1 line") also shows a

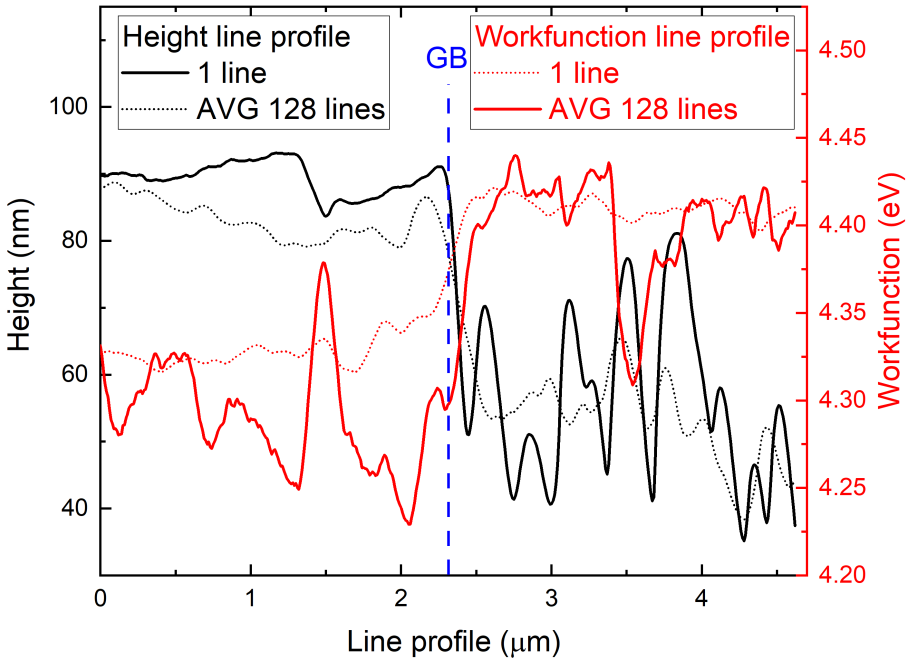

Figure 5.9: Topography and workfunction line profiles extracted from the KPFM image acquired in region 8 of the CIGSe sample. The red line in Figure 5.8 (a) indicates where line profiles were extracted to produce the graph. Single line profile and the average of 128 lines are plotted, with black lines showing the topography and red lines showing the workfunction.

slight change in the topography in the vicinity of the GB, which could cause a change in workfunction. For this reason, the average of 128 line profiles along the GB was analyzed, and it does not show the workfunction contrast at the GB anymore.

To conclude, small workfunction fluctuations close to the GB are associated with changes in topography and not with the electronic properties of the GBs, and consequently, no band bending is observed for this type of GBs. The same conclusions can be made for region 9 (Figure 5.7 (b)), where an entirely different GB was formed.

Similar analyses were done for regions 10 and 11, where a flatter GB was formed (see Figure 5.6 (e and d)). From the workfunction maps of regions 10 and 11, Figure 5.7 (e and d), respectively, one can see a lower workfunction value in a broad region near the GB. The width of these lower workfunction regions is $\approx 2\,\mu$m for region 10 and $\approx 4\,\mu$m for region 11.

Figure 5.10 (a) depicts the workfunction map of region 10. This workfunction map is the same image shown in Figure 5.7 (e) but rotated by 13.5° for better visualization of the GB interface. The inset figure is the equivalent topography acquired simulta-

neously with the workfunction map. Interesting, a distinct morphology was visible in the vicinity of the GB. As highlighted in the images, there is a strong correlation between the topographical features with the area where the lower workfunction was observed.

The lower workfunction value in the GB vicinity can be associated with a local change in strain. At the beginning of this chapter, it was shown that the AFM topography of the GaAs substrate before growing the CIGSe on top (see Figure 5.2). Back there, changes of up to 50 nm in height between one grain and the other were observed. Such changes in height combined with a slight mismatch in the lattice parameter between GaAs and CIGSe could cause changes in the strain, leading to a different morphology for the CIGSe. Furthermore, the width of the low workfunction area combined with the strong correlation between the workfunction and the topography maps excludes the space charge region hypothesis and suggests the changes in the strain as the responsible for the observed lower workfunction. Unfortunately, the local strain could not be confirmed and quantified with an appropriate tool (e.g., via TEM) in this thesis.

Figure 5.10 (b) depicts the workfunction distribution in 3 different areas of Figure 5.10 (a). Colored squares in the inset topography image highlight the chosen areas used for the statistical distribution, called rougher (red), GB vicinity (blue), and flatter (green). Gaussian fittings were again used here, and their peak positions are highlighted by the dashed lines in Figure 5.10 (b). The number of Gaussian peaks was chosen according to the visible contrasts in the workfunction maps, where three distinct color contrast are observed at the grains, and a uniform distribution is observed in the GB vicinity. The values for the Gaussian peak positions are:

- 4.41 eV, 4.37 eV, and 4.32 eV at the rougher region;
- 4.41 eV, 4.35 eV and 4.29 eV at the flatter region;
- 4.29 eV at the GB region.

Interestingly, for the analysis done in region 8 (Figure 5.8), the workfunction value of 4.41 eV was attributed to the {112} facets. This value is again present, reinforcing the argument of faceting formation with higher workfunction values attributed to the most energetic favorable {112} facets.

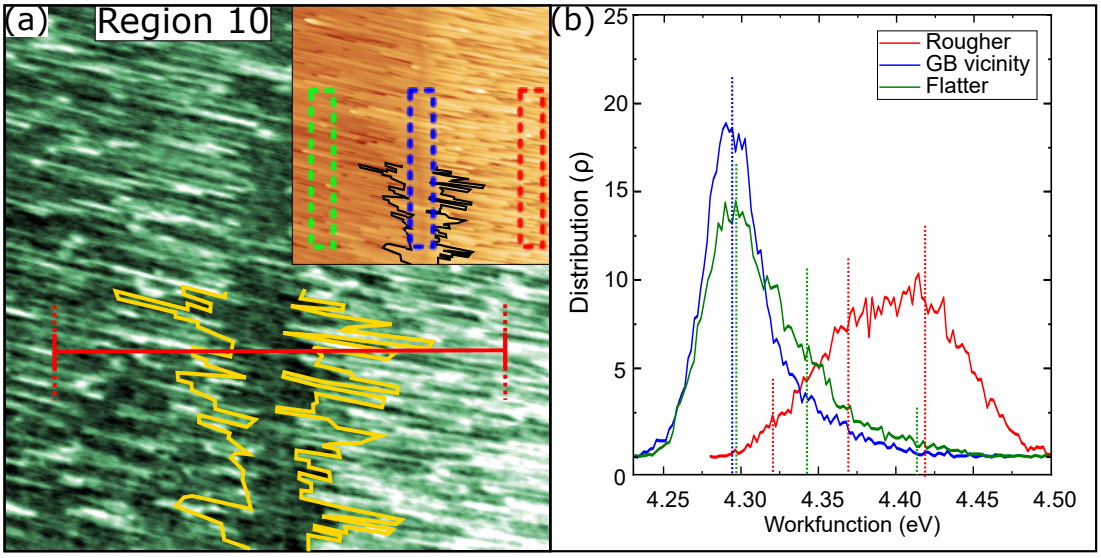

Figure 5.10: (a)KPFM image acquired in region 10 of the CIGSe sample. The colored dashed squares indicate the areas used for the statistical workfunction distribution plotted in (b). Lower workfunction values are present in the vicinity of the GB. This region is highlighted in yellow and correlates with a distinct morphology in the topography image (inset image). Dash lines in (b) highlight the peak positions for using Gaussian fittings.

On top of that, a shallow contrast in the workfunction map was observed right at the GB. Line profiles extracted from the red line in Figure 5.10 are plotted in Figure 5.11, with a dashed blue line marking the GB position. Solid lines represent a single workfunction (red), and topography (black) line profiles extract from the marked red line in Figure 5.10 (a). Higher workfunction values of $\approx 40\,\text{meV}$ located right at the GB, were observed with the "1 line" profile. Interestingly, by averaging 128 line profiles (dotted lines), the higher workfunction values at the GB were still there but with reduced intensity ($\approx 10\,\text{meV}$). Although the 128 averaged line profiles show the contrast, it can be seen from the workfunction map (Figure 5.10 (a)) that this tinny contrast was not always visible along the entire length of the GB, even within the scanned area, and it was also not visible in the region 11.

Once again, the shallow contrast at the GB could be due to a different facet formation, as there is a slight change in topography in this region. The only conclusion from this data is that no, or insignificant band bending was observed for the five analyzed GBs. The results agree with the observed for $\Sigma 3$ twin boundaries in $CuGaSe_2$

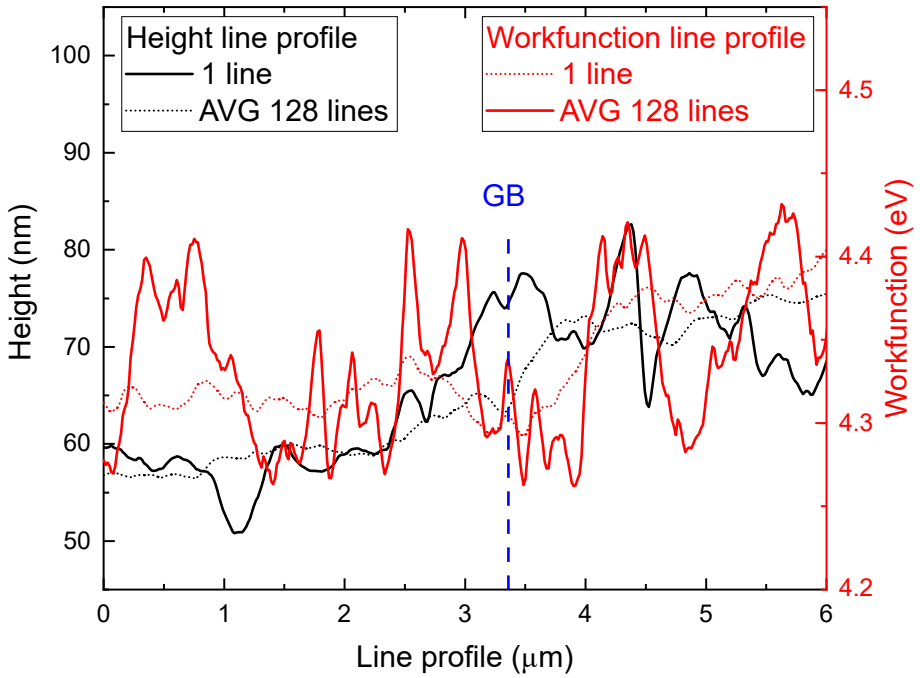

Figure 5.11: Topography and workfunction line profiles extracted from the KPFM image acquired in region 10 of the CIGSe sample. Red line in Figure 5.8 (a) indicates where line profiles were extracted to produce the graph. Single line profile and the average of 128 lines are plotted, with black lines showing the topography and red lines showing the workfunction.

[58] and with first-principles calculations from Persson *et al.* [7], where they predicted that depending on the CIGSe composition, an electrostatically neutral barrier at the GBs can be formed. It could also be related to the doping levels of the absorber, where low doping limits the barrier heights.

5.3.2 UHV annealing to remove residues from the sample surface

This section presents the observed changes at the CIGSe surface after an annealing step at 200° for 30 minutes and under UHV conditions. The annealing step was introduced to properly remove impurities from the sample surface due to adsorbates or organic residues that could hide the pristine CIGSe workfunction [180]. The 30 minutes at 200 °C under UHV was chosen according to the procedures from Boumenou *et al.* [82] and Mönig *et al.* [181], where surface deterioration due to loss of selenium could be neglected. Indeed, the experiments on the annealed single-crystalline CISe grown on

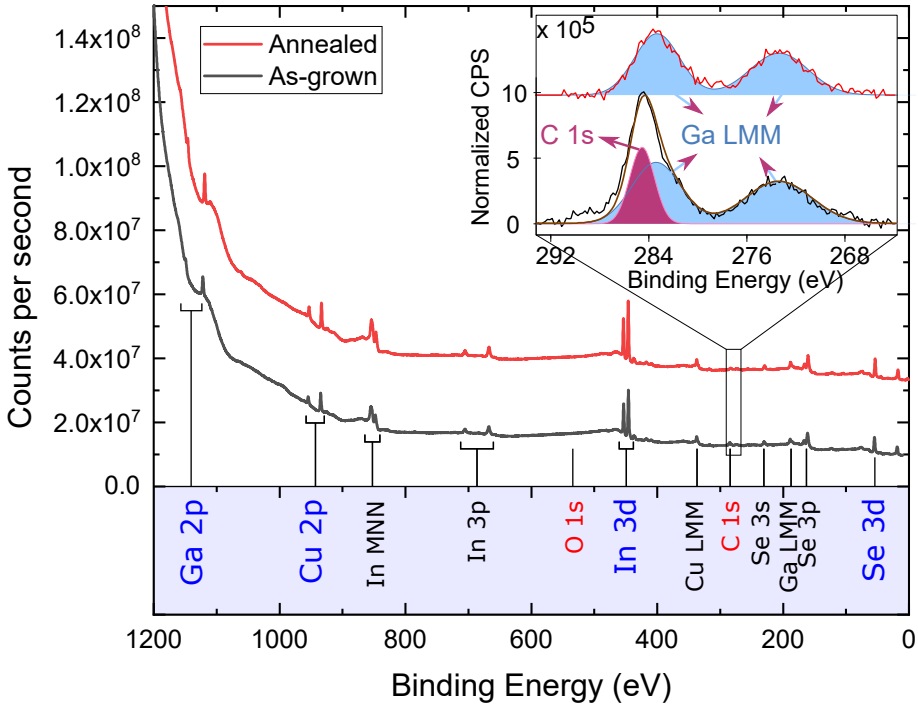

Figure 5.12: XPS of the as-grown and annealed CIGSe epitaxially grown on multi-crystalline GaAs substrate. Black and red curves show the survey spectra of the as-grown and the annealed conditions, respectively. At the bottom, the peaks are labeled. In blue, the peaks used for quantification. O 1s and C 1s regions are highlighted in red and black, the other prominent visible peaks in the survey. The inset figure shows the high-resolution scan in the binding energy region of the C 1s peak, and it shows that C 1s peak overlaps with Ga LMM Auger peaks. A proper fitting allows splitting the C 1s from the Ga LMM peak, which shows no carbon on the sample surface after the annealing step.

GaAs (100) show a complete recovery of the workfunction to the pristine values using the above-mentioned conditions (see Appendix A.1).

Figure 5.12 depicts the XPS survey spectra of the CIGSe sample before and after the annealing step, with black and red lines, respectively. First of all, the identification of all the CIGSe elements can be done on both spectra. The peaks used for quantification are labeled in blue, and other predominant peaks are labeled in black. In red, the binding energy region of the C 1s, and O 1s peaks are labeled. As previously mentioned, no oxygen peaks were observed for both samples, confirming that the transfer procedure using an inert gas transfer system avoided any oxygen contamination.

However, some peaks appeared in the binding energies close to Carbon 1s. The

Table 5.1: XPS surface quantification

XPS surface quantification (atomic %)						
	Cu 2p	In 3d	Ga 2p	Se 3d	C 1s	O 1s
As-grown	14.4	21.6	18.8	32.6	12.6	0
UHV annealing	17.8	22.7	27.9	32.6	0	0
Ratio between elements						
	Cu/(Ga+In)		Ga/(Ga+In)		Se/(Cu+Ga+In)	
As-grown	0.36		0.47		0.59	
UHV annealed	0.35		0.55		0.46	

inset graph in Figure 5.12 enlarges the view of the C 1s binding energy region. Two peaks are present in this region, one with a maxima peak position at ≈ 285 eV and another at ≈ 273 eV. In the as-grown spectra, the peak at ≈ 285 eV can be separated into two contributions: 285 eV from C 1s and 283.4 eV from Ga LMM Auger peaks [157]. Using the constraints of the Ga LMM peak from the as-grown condition to the spectrum of the annealed condition, reveals no indications of C 1s within the resolution limit of the XPS.

The summary of XPS surface quantification is presented in Table 5.1. It shows that besides removing carbon from the surface, there was a significant increase in the gallium content followed by a decrease in the Se content. It is more evident when only the ratios between the CIGS elements are analyzed. The GGI ratio went from 0.47 to 0.55 and the Se/(Cu + Ga + In) went from 0.59 to 0.46. The increase in gallium content is justified by its diffusion from the GaAs substrate to the CIGSe absorber. A few reports have also shown that Se has high vapor pressure being prone to volatilize at higher temperatures, as measured via X-ray fluorescence by Zhang *et al.* [182]. However, much lower temperatures were used here.

Apart from changes due to the annealing steps, it is worth pointing out some other characteristics of this sample surface. A substantial copper depletion at the surface is observed even in the as-grown condition, as seen in the CGI ratio. Such Cu depletion was already reported in the literature, and its origin is highly debated. One explanation for the Cu depletion at the surface is related to the reconstruction of the polar (112) and ($\overline{1}\overline{1}2$) surfaces [47], [168], [183], [184]. Indeed, in the previous

section, the KPFM data suggested the presence of 112 facets, which could then be Cu depleted due to surface reconstruction. Considering that the XPS penetration depth is between 5 to 10 nm, the reconstruction should not represent more than 20% of the signal measured via XPS, leading to a measured CGI of 0.8. However, one should also keep in mind that the analyzed surface is pretty much faceted, changing the real angle between the sample, the XPS X-Ray and the analyzer, and consequently the penetration depth of the XPS.

An additional explanation for Cu-depletion would be the Cu-electromigration on Cu-poor absorbers. This model was proposed by Herberholz *et al.* [45] and says that charges at the surface could cause band bending, dragging Cu from the surface to the bulk. Consequently, the fact that reconstruction may interfere with the Cu content at the surface, but other factors have to be considered. This discussion will appear again in the next chapter when metallic potassium is deposited on the sample surface.

In the following, KPFM data on the annealed sample will be presented. Figure 5.13 shows the KPFM images in regions 8 to 11, before and after annealing. It can be immediately noted that a similar trend with facet-dependence workfunction was kept. Additionally, an increase in workfunction upon annealing was measured, with an average of 0.55 eV higher workfunction values in the measured regions. The increase in the workfunction is explained by the absence of carbon adsorbates on the surface, but it can also be due to the change in the surface composition, as shown by XPS.

Below is the summary of the measured average values from region 9 using Gaussian fitting (Figure 5.13 (f)).

- 4.95 eV for the pyramid-like region;
- 4.81 eV, 4.89 eV and 5.04 eV for the trench-like region;

.

The criteria for choosing the number of Gaussian peaks in the workfunction distribution was based on the number of color contrasts seen in the KPFM maps, the same procedure as presented in the previous analyzes (Figure 5.8 and Figure 5.10). The higher value in the trench-like structure (5.04 eV) and the value for the pyramid-like structure (4.95 eV) are the ones associated with the {112} facets. It is interesting to note that region 9 now presents an average lower workfunction with a width of ≈

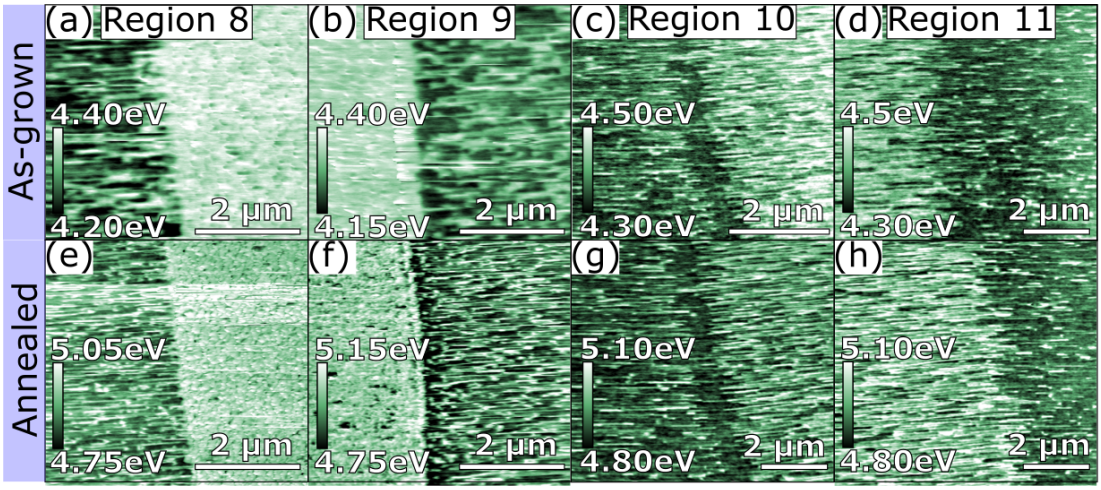

Figure 5.13: KPFM maps before and after annealing. An increase in workfunction was observed for all the analyzed regions.

2μm in close vicinity of the GB (see Figure 5.13 (f)), similar to regions 10 and 11 (see Figure 5.13 (c, d, g, and h)). As the contrast is very weak, it could be that it was masked by the carbon adsorbate layer in the as-grown condition. Again, this region of lower workfunction could be related to some differences in strain in the close vicinity of the GBs.

The average workfunction values were also measured for region 10 (Figure 5.13 (g)), which are summarized below.

- 4.89 eV, 4.96 eV, and 5.02 eV for the rougher region;
- 4.85 eV, 4.94 eV, and 5.02 eV for the the flatter region;
- 4.85 eV for the lower workfunction region.

The observed tinny contrast ($\approx$ 10 meV) at the GB of region 10 in the as-grown condition vanishes after the UHV annealing. Interestingly, the measurements were acquired at the exact same spot before and after annealing, which excludes the heterogeneity of the workfunction at the GB. Even so, the origin of the observed contrast in the as-grown condition was not clear, it could be facet-related or band bending, and it is also difficult to conclude what makes the contrast to disappear. Perhaps passivation of the defect at GB (the case of band bending) or some reconstruction of the surface upon annealing that changes the surface termination (the case of facet-related workfunction) could be associated with the disappearance of the observed signal.

5.4 Chapter summary

- The occurrence of faceted surfaces forming pyramid-like and trench-like surfaces were observed, which are associated with the low energy polar {112} facets.
- AFM topography maps showed that the GBs of the CIGSe epitaxially grown on multi-crystalline GaAs can be very smooth or with significant height changes depending on the grain orientations.
- A few GB regions were macroscopically selected for a systematic KPFM characterization. Workfunction differences up to 200 meV between grains were associated with different surface terminations.
- No, or very shallow workfunction contrast at the GB was observed for all the analyzed regions. However, few regions presented lower workfunction values with 2 μm width in the vicinity of the GBs. This change in workfunction was associated with changes in the strain that also induced morphological changes in the vicinity of the GBs.
- An additional annealing step of 200 °C for 30 minutes under UHV led to an increase in the gallium content followed by a decrease in the selenium content at the surface. Gallium increase is associated with diffusion from the GaAs substrate to the CIGSe. The annealing step also removed the carbon adsorbates, leading to a surface completely free of oxygen and carbon, as measured via XPS.

Chapter 6

Alkali post-deposition on CIGSe absorber grown on multi-crystalline GaAs substrate

Parts of the results in this chapter were published in the contribution Lanzoni *et al.* [158].

The most common mechanism for alkali incorporation into the CIGSe absorber is based on the thermal evaporation of alkali fluorides under a selenium atmosphere [17]. Besides improving the optoelectronic properties, disentangling the individual contributions of the GBs, the surface, and the absorber bulk can be very difficult. The main reason is the system complexity of the CIGS materials under PDT, where many concurring chemical reactions and diffusion processes of all the involved elements happen simultaneously. This chapter will show how pure metallic K diffuses and interacts with a CIGSe absorber epitaxially grown on GaAs (100) and multi-crystalline GaAs. The evaporation is done at room temperature, followed by an annealing step at 200 °C for 30 minutes to promote diffusion into the bulk. More details of the evaporation procedure are discussed in Chapter 2.

The chapter starts by presenting the results of K deposition on epitaxial CISe and CIGSe grown on GaAs (100) to understand the diffusion mechanisms in the absence of GBs. Then, K deposition on epitaxial CIGSe grown on multi-crystalline GaAs substrates elucidates how K acts at well-defined GBs.

6.1 Workfunction changes after K deposition on single-crystalline CISe

Before starting this section, the nomenclature of the samples needs to be adapted to avoid misunderstandings. The reason for that is related to the diffusion process of K into the CIGSe absorber, where additional annealing steps will be studied. From now on, the called **K-free** absorber is assumed to be the as-grown sample that underwent a 200 °C UHV annealing to remove the carbon contamination. This amendment results in the following set of samples:

- **As-grown** - The sample without any treatment or annealing.
- **K-free** - The sample that underwent a UHV annealing of 200 °C for 30 minutes.
- **K-deposited** - The K-free sample plus a thin layer of K deposited on the surface
- **K + annealing** - The K-deposited plus additional annealing to promote diffusion.

To first check the deposition mechanism of K on single-crystalline CIGSe surfaces, the known Cu-rich CISe sample (see Chapter 4) was used as a reference. The KPFM setup was used to in-situ monitor the workfunction changes after each step of K deposition and annealing. The measured workfunction maps are depicted in Figure 6.1. The scale bar of all the images is set between 3.4 eV to 5.4 eV, allowing better comparison of workfunction changes after the various treatments.

Figure 6.1 (a) shows the workfunction map in the as-grown condition. As presented in Chapter 4, well-oriented workfunction contrasts linked to the {112} facets are visible in the as-grown sample. This contrast is present on the entire set of images, meaning that the faceting influences the surface workfunction even if a very thin layer is present on the surface.

K deposition also led to a drastic drop in the workfunction, as shown in Figure 6.1 (b). Such a change was expected since the workfunction value for thick K films is much lower than that of CISe. The workfunction values are predicted to be 2.74 eV, although experimental measurements led to 2.3 eV [163]. Subsequent UHV annealing

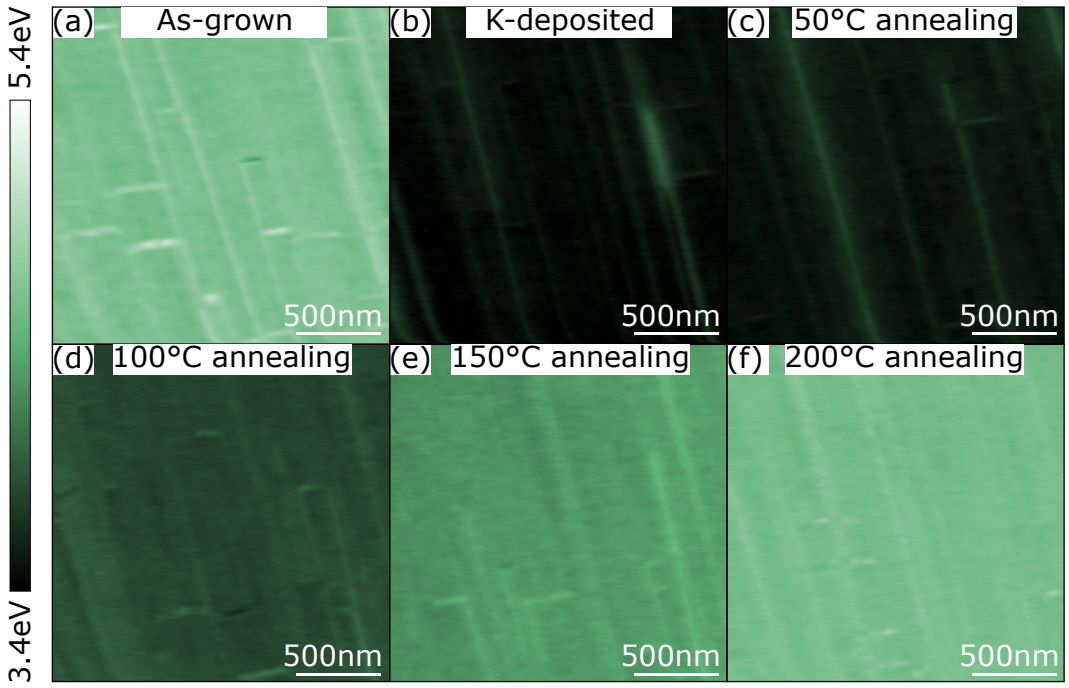

Figure 6.1: KPFM workfunction maps after each stage of the K deposition. (a) as-grown condition. (b) with a thin layer of metallic K on the surface. (c - f) after annealing steps.

steps ranged from 50 °C up to 200 °C for 10 minutes each. The workfunction gradually increased after each annealing step, indicating a reduction of the K content at the surface. After heating to 200°C, the pristine workfunction value was almost recovered. Even though the workfunction massively varied, no changes in morphology were visible between the treatments (topographic images are not shown here).

A summary of the workfunction changes after the various treatments is depicted in Figure 6.2. It shows the average workfunction over the scanned area, with the workfunction in the as-grown condition, after K deposition, and after the annealing step represented by the red, blue, and green bars, respectively. The error bars were extracted from the measured RMS values in each image.

Despite the used methodology being a very effective and sensitive way of identifying the presence of K on the surface, it does not tell if the observed recovery of the workfunction values to the pristine stage is due to diffusion of K inside the CISe bulk or if it evaporates after the post-annealing steps. Even if the vapor pressure of K is relatively high at room temperature [185] and is unlikely to happen, correlative measurements were needed, and a special set of samples was prepared for that.

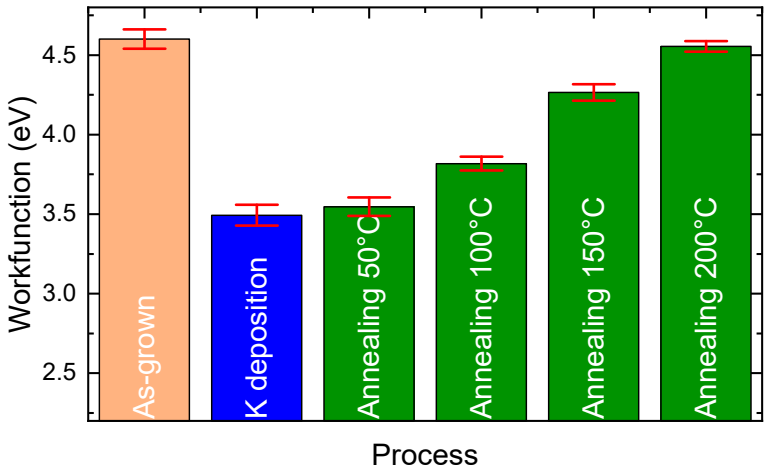

Figure 6.2: Average workfunction after indicated samples treatment. The error bars were extracted from the RMS values of each image.

6.2 K deposition on single-crystalline CIGSe epitaxially grown on GaAs (100)

Two sets of samples were prepared, namely Cu-rich CIGSe and Cu-poor CIGSe. XPS, SIMS, and PL, allied to the previous KPFM measurements, were used to understand the mechanism of depositing pure metallic K on the epi-CIGSe and the consequence of subsequent annealing steps. Initial XPS measurements were carried out for the **Cu-rich** and the **Cu-poor** samples in the following conditions:

- As-grown sample;
- K-free sample;
- K-deposited sample;
- K-deposited sample + 200° annealing

The XPS data from this section were measured in collaboration with Dr. Harry Mönig and Amala Elizabeth from Westfälische Wilhelms-Universität and Center for Nanotechnology (CeNTech) at Münster in Germany. It is essential to point out one characteristic that differs the XPS data presented in this section from those in the remaining thesis: the X-ray source. Here, a monochromatic Al Kα source was used, improving the energy resolution but also showing some undesired Auger peaks right at

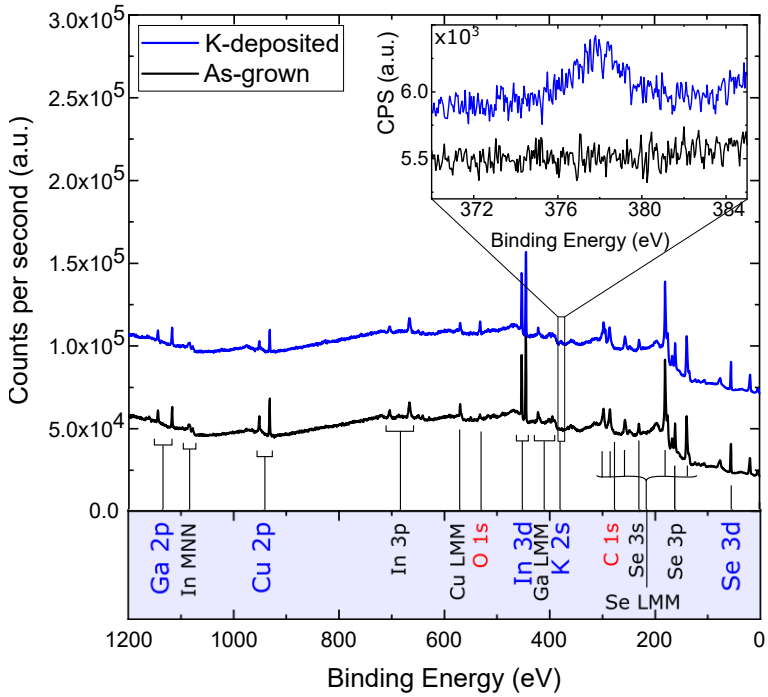

Figure 6.3: XPS data showing the presence of K at the sample surface after deposition. All the CIGSe elements can be identified in the survey spectra, with the blue labels highlighting the peaks used for quantification, the red show the oxygen and carbon peaks, and the black labels showing the remaining predominant peaks. The inset confirms the presence of K on the surface.

the K 2p and C 1s binding energies (see Appendix A.2). More details and differences between each experimental setup can be found in Chapter 2.

To prove that K was successfully deposited on the CIGSe surface, XPS measurements were performed in the sample with and without K . The survey spectra of the Cu-rich sample with and without K are presented in Figure 6.3. All the CIGSe predominant peaks are labeled at the bottom of the figure. The survey spectra allowed the identification of all the CIGSe elements in both as-grown and K-deposited samples, black and blue lines, respectively. The inset graph shows the binding energy region for the K 2s peak, where the presence of K on the K-deposited surface is confirmed (blue curve).

A rough estimation of the K thickness can be done by analyzing the XPS intensity of the CIGSe peaks before and after K-deposition. Lambert-Beer's law was used here, which describes the attenuation of the photoelectrons originating from the CIGSe in

the presence of an overlayer, in this case, K. The law can be written via

$$I_K = I_0 \cdot exp\left(-\frac{d}{\lambda_{IMFP} \cdot cos\theta}\right) \tag{6.1}$$

Where I_0 and I_K are the peak intensities of the film before and after K deposition. The inelastic mean free path of the photoelectrons penetrating a K over-layer is denoted as λ_{IMFP}, and the angle θ corresponds to the emission angle. The intensity changes of the Se 3d before and after deposition were used here as I_0 and I_K. Se 3d was chosen since its kinetic energy is higher, meaning it is less affected by any other surface contamination, and because strong diffusion of Se due to K deposition is not anticipated. λ_{IMFP} from the NIST database were used for the calculation [156], leading to a calculated K thickness of 8 Å (via Equation 6.1).

A comparative study of the as-grown and K-deposited samples was carried out via XPS to check chemical variations in the K-deposited sample surface upon annealing. As shown in Figure 6.2, the 200 °C annealing temperature was enough to recover the workfunction to the pristine condition. Based on that, the samples were annealed at 200 °C for 30 minutes. Figure 6.4 depicts the survey spectra of the K-deposited Cu-rich (blue) and Cu-poor (orange) samples, both before (darker colors) and after (brighter colors) UHV post-annealing steps. At first sight, the survey spectra did not massively change upon post-annealing. However, the XPS quantification showed that the post-annealing step reduced by half the amount of K on the surface of the Cu-poor sample but did not change the amount of K on the Cu-rich one. It can be seen in the inset graph of Figure 6.4, where the blue bars represent the atomic percentages of K on the Cu-rich before (dark blue) and after (bright blue) annealing. The orange bars represent the atomic percentages of K on the Cu-poor before and after annealing, respectively, dark and bright.

Table 6.1 summarizes the XPS quantification. Despite the changes in the K concentration for the Cu-poor absorber, a decrease in Cu content followed by an increase in Ga content is observed after annealing. These changes are more evident when the CGI and GGI ratios are analyzed. Cu-rich and Cu-poor samples show respectively $\approx$ 54% and 33% reduction in the CGI ratios. Both samples show an increase of $\approx$ 65% in the GGI after the annealing step. However, the compositional changes are not linked to binding energy shifts, which do not support a new chemical bond formation, i.e.,

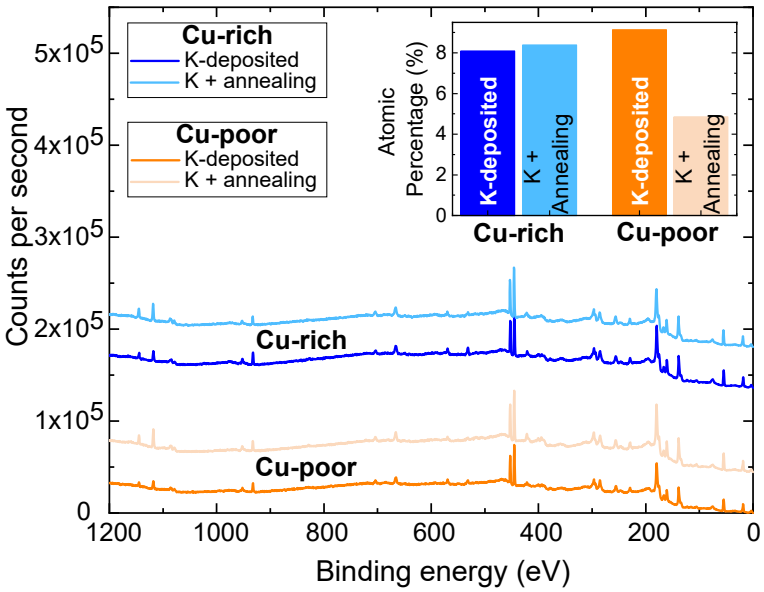

Figure 6.4: XPS spectra of the Cu-poor (orange) and Cu-rich (blue) single-crystalline CIGSe and K-deposited. Darker Orange and darker blue refer to the K-deposited sample (thin layer of K on the surface). Brighter orange and brighter blue refers to the K-deposited samples annealed at 200 $°C$ under UHV. The inset shows the amount of K present on the surface after annealing using the K2s peak for quantification.

$KInSe_2$.

The combination of KPFM and XPS data showed that the observed changes in the electrical properties along all the K deposition steps are mainly attributed to the presence or absence of K on the surface. However, these measurements did not give enough information regarding the diffusion of K and how it distributes inside the CIGSe bulk. For this reason, the "K-free" and the "K-deposited + annealing" samples were measured via SIMS depth profiles. As air exposure could not be circumvented, a CdS buffer layer was deposited on the CIGSe surface via chemical bath deposition. The CdS had the advantage that residual K on the CIGSe surface could be removed, and it also protected the surface from further degradation.

Figure 6.5 depicts the K depth profile for the Cu-rich (blue) and Cu-poor (orange). Solid brighter curves refer to the depth profile of the sample containing K (plus a post-deposition 200°C annealing), whereas the dashed darker curves arise from samples without K. The normalized depth profile first showed a higher amount of K observed all over the bulk length for both K-deposited samples, which proves that K diffused inside the bulk. Higher K counts were also observed in the CdS/CIGSe interface for

Table 6.1: XPS surface quantification of the K-deposited and annealed samples

XPS surface quantification (atomic %)								
Cu-rich sample								
	Cu	In	Ga	Se	K	O	CGI	GGI
K-deposited	8.3	19.8	6.0	39	8.0	18.8	0.32	0.23
K + annealing	5	23.0	10.0	41.5	8.4	12.2	0.15	0.30
Cu-poor sample								
	Cu	In	Ga	Se	K	O	CGI	GGI
K-deposited	7.5	22.2	6.0	41.8	9.1	13.3	0.27	0.22
K + annealing	6.3	23.5	10.9	47.6	4.8	6.8	0.18	0.32

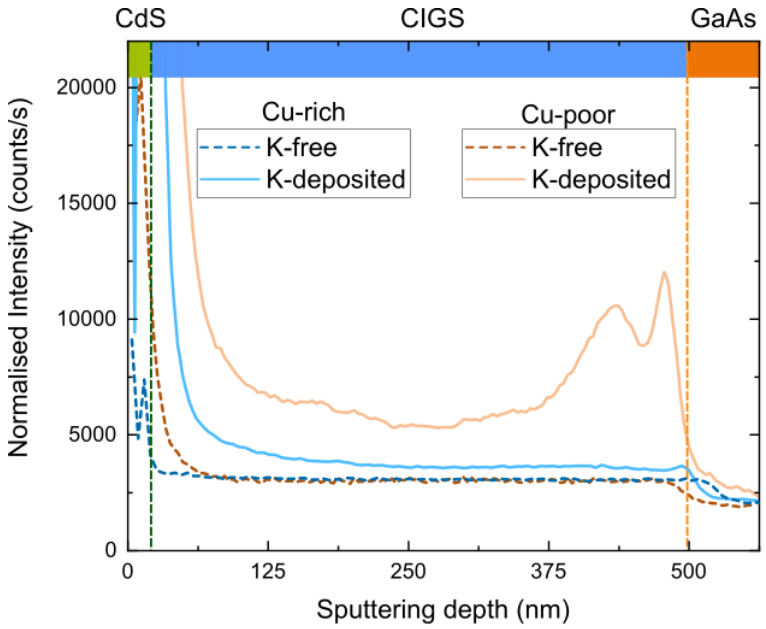

Figure 6.5: SIMS depth profile of the K-deposited CIGSe sample showing the diffusion of K into the bulk. Blue and orange curves represent the depth profiles for the Cu-rich and Cu-poor samples, respectively, being the K-free the dashed darker colors and the K-deposited the solid brighter color. In the Cu-poor case, there is an accumulation of K at the interface between CIGSe and GaAs.

all spectra. Such effect were also observed in literature for polycrystalline CIGSe [12]. Perhaps when moving from one material to the other, the sputtering rate can change (matrix effect), and consequently, different intensities are expected.

Both, Cu-rich and Cu-poor samples showed an in-diffusion of K into the bulk of the CIGSe, as depicted by the higher counts in Figure 6.5. However, the Cu-poor sample showed much higher counts of K in the bulk and a pronounced accumulation at the CIGSe/GaAs interface, with a double peak near the back contact. The observed double peak is probably related to a combination of effects, ranging from K accumulating in both matrix (CIGSe as well as in the GaAs substrate), voids at CIGS/GaAs interface, or even a matrix effect, where the same material can ionize more or less depending on the surrounding atoms. The clear difference between Cu-poor and Cu-rich indicates that K diffuses easily in Cu-poor absorbers. It supports the XPS results shown in Figure 6.4, where the atomic percentage of K at the surface did not significantly change for the Cu-rich sample, while it decreased by half for the Cu-poor. These results confirmed that the diffusion mechanism of K in CIGSe absorbers is not limited to the GBs, and the number of Cu vacancies can be the channel for K diffusion inside the CIGSe bulk.

Further studies of the optoelectronic properties related to the addition of K on the CIGSe absorbers were carried out employing panchromatic PL imaging. The same set of samples used in the SIMS measurements was used in the PL imaging, meaning that the samples were capped with a CdS buffer layer of $\approx 20\,\text{nm}$. A special transparent box was used to keep the samples under N_2 environment.

The panchromatic PL image of the K-deposited Cu-rich CIGSe sample is depicted in Figure 6.6. Due to the glass cover of the transparent box, some interference rings in the PL intensity image were observed. These artifacts must not be considered in the following discussion. A region of lower PL yield is highlighted with a dashed blue line in the image. Interestingly, the lower PL yields coincided with the region covered by a physical mask, which protected the surface from K deposition. A line profile was extracted from the black line in Figure 6.6 (a) and is presented in Figure 6.6 (b). The line profile shows even more evidence that the lower intensity in PL yield for the region where no K was deposited. The same is observed for the Cu-poor sample (not shown here). The PL setup allowed access to the real impact of K on CIGSe absorber

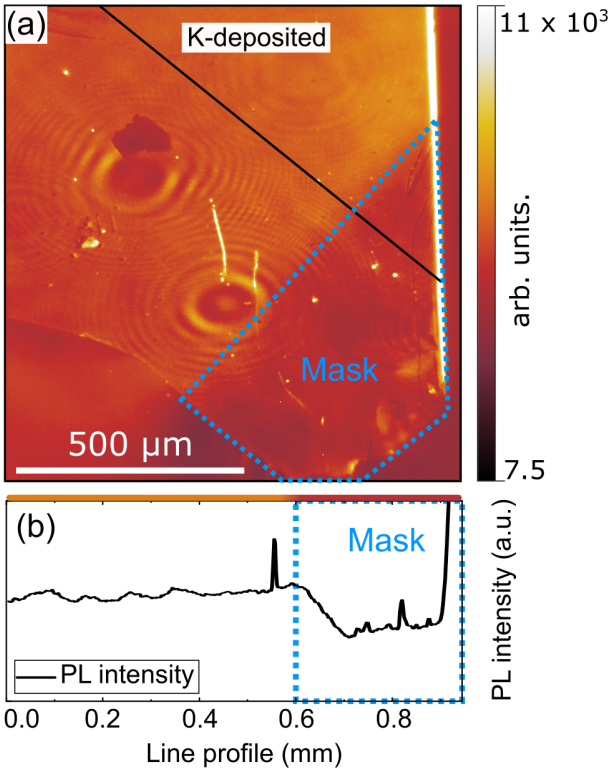

Figure 6.6: PL imaging of the K-deposited Cu-rich CIGSe absorber. Figure reproduced with permission from Lanzoni *et al.*, ©(2022) Thin Solid Films - Elsevier.

properties without caring about small fluctuations in the sample composition. Indeed, Ramírez *et al.* [118] showed that the single-crystalline CIGSe absorbers grown on a two-inch GaAs wafer did present a slight compositional gradient. Moreover, it is essential to remind that the K-free absorber underwent only one annealing step, whereas the K-deposited sample was annealed twice. Therefore, the results here show the importance of carrying PL imaging on the same piece of the absorber. Such methodology allowed the observation of the improved the optoelectronic properties due to the addition of K.

Consequently, these results corroborate the systematic study from Ramírez *et al.* [118] for the KF PDTs on epi-CIGSe. Ramírez *et al.* [118] showed improvements in the quasi-Fermi level splitting of up to 30 meV after KF treatment, while ≈ 2 meV was measured for the samples presented in this thesis. However, compositional changes might be of enormous importance here, where Cu-poor samples showed a decrease in quasi-Fermi level splitting after KF deposition. The XPS data presented here showed that the Cu content is reduced after K+annealing. Moreover, ≈ 1 monolayer of K was

evaporated on the CIGSe absorber that diffuses after post-annealing. It is different from the standard KF PDTs, where higher temperatures and more material (between 6 nm to 10 nm) are employed [17], [118].

6.3 Grain boundary characterization of K-deposited CIGSe epitaxially grown on multi-crystalline GaAs substrate

The previous section showed the effect of alkali post-deposition on single-crystalline CIGSe grown on GaAs (100), where potassium diffusion causing changes in the opto-electronic properties were observed even in the absence of GBs. Now, a study of how the alkali interacts with the CIGSe in the presence of large GBs will be presented. The CIGSe sample epitaxially grown on multi-crystalline GaAs substrate was used. The K deposition procedure was the same as for the GaAs (100) case, meaning that the as-grown CIGSe sample was first UHV annealed at 200 °C to remove surface contaminations, then K was deposited, and a subsequent UHV annealing at 200 °C was done to promote the diffusion of K into the bulk.

KPFM was performed in the same regions 8, 9, 10, and 11 that were presented in Chapter 5. Figure 6.7 depicts the topography (a-e) with the simultaneously acquired workfunction (f-j) maps after each step of K-deposition on region 10. As previously mentioned, region 10 had a tiny workfunction contrast ($\approx$ 10 meV higher values) at the GB and a significant broad darker contrast in the vicinity of the GB ($\approx 2\mu$m width) that can be seen in Figure 6.7 (f). It was also shown that the GB workfunction contrast completely vanishes after a 200 °C annealing step, while the broad darker contrast remains (see Figure 6.7 (g)). Interestingly, for the as-grown (a-e) and K-free samples (b-f), the exact same spot of the sample was measured, which mitigates any factor other than the annealing step as the responsible for the observed changes in the workfunction.

Similar to the single-crystalline CISe on GaAs (100), a drastic change in workfunction was observed for the K-deposited sample. The average value decreased from 4.95 eV to 3.55 eV, which is very close to the obtained for the case of CISe grown on

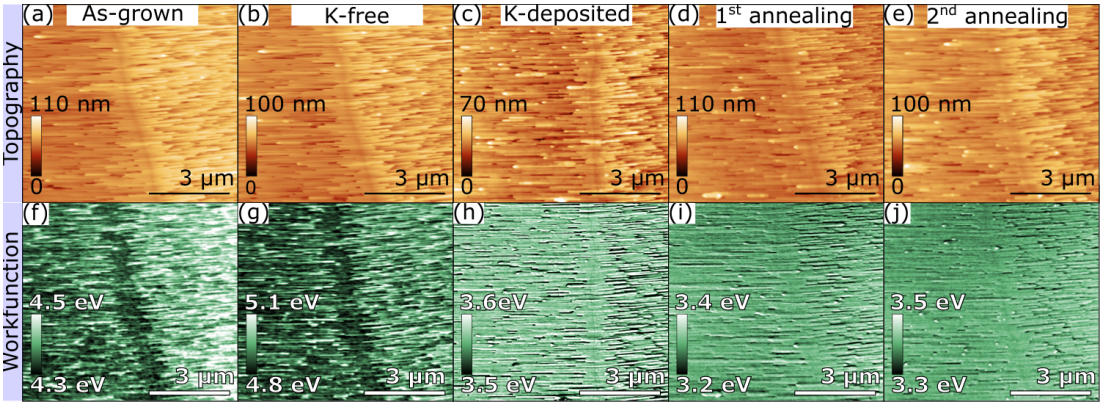

Figure 6.7: KPFM from region 10 after each step of K-deposition: (a-e) topography and (f-j) workfunction maps.

GaAs (100) (3.49 eV, see Figure 6.2). The decrease in workfunction is expected since metallic K has a theoretical workfunction of 2.74 eV [163]. Despite the significant change in the workfunction, no precipitation or other material accumulation was observed in the topography image. It confirms a uniform deposition all over the sample surface. Surprisingly, the full recovery of the workfunction values was not observed after the UHV post-annealing step. An additional post-annealing step did not produce further changes in the workfunction values, as shown in Figure 6.7 (e) and (j).

XPS data (Appendix A.3) support the KPFM data, by showing that a considerable amount of K remains on the surface, which explains why the measured workfunction values did not change after annealing. However, it contradicts the experiment carried out on single-crystalline CIGSe on GaAs (100), where the workfunction completely recovered after annealing (Figure 6.2), and an in-diffusion of K was observed (Figure 6.5). Many parameters changed from one experiment to another, starting from composition and thickness, and going up to the GBs present in the multi-crystalline substrate.

For this reason, the experiment was repeated with a new set of samples. This time, half a wafer of multi-crystalline and half a wafer of GaAs (100) substrates were loaded into the MOVPE to allow the CIGSe to be grown simultaneously on both substrates. The samples were immediately transferred to the UHV machine using the inert gas transfer system. Additionally, all the K-deposition and measurements were done in-situ inside the UHV machine, with the samples mounted side by side in the same sample holder (see the picture of the substrates in Appendix A.6). The used pieces

faced each other during the CIGSe growth to minimize compositional changes.

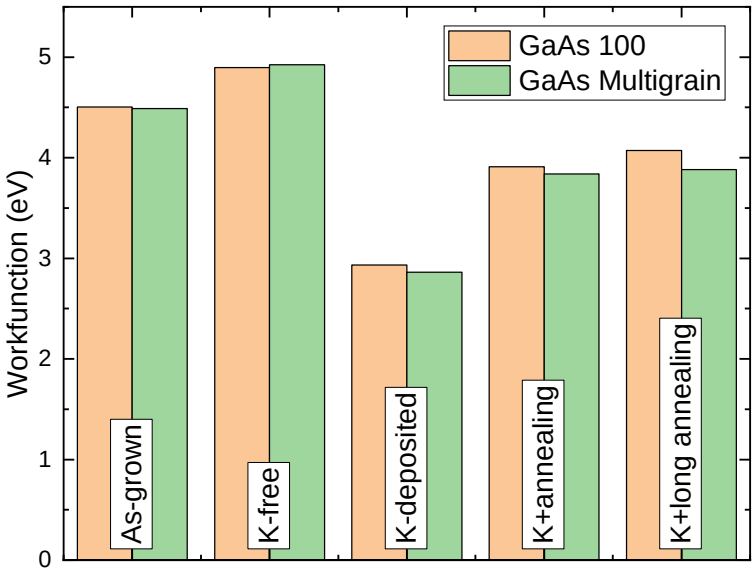

Figure 6.8: KPFM workfunction summary of the K-deposition of the CIGSe epitaxially grown on GaAs (100) and Multi-crystalline substrates.

Figure 6.8 summarizes the workfunction variation after each K-deposition step. An immediate observation is the similar workfunction variations for both samples (grown on GaAs (100) and multi-crystalline substrates) after each process. Additionally, the trend observed for the CISe grown on GaAs (100) Figure 6.2 was confirmed here, where the workfunction of the as-grown sample increased upon annealing and decreased after K deposition, with a subsequent recovery after post-annealing. Interestingly, only a partial recovery of the workfunction values after the subsequent annealing steps was observed.

XPS data were also acquired between each deposition step. Using Equation 6.1, the calculated thickness of the thin K layer was 2.84 nm, much more than what was measured in section 6.1 (0.08 nm). The discrepancy is surprising since the same deposition procedure was done; however, it is essential to note that the entire procedure for the CIGSe samples from section 6.3 was done under UHV, while the CIGSe samples from section 6.1 were exposed to N_2.

Figure 6.9 depicts the evolution of the measured $Cu/(Ga+In)$, $Ga/(Ga+In)$, $Se/(Cu+Ga+In)$, and $K/(Ga+In)$ ratios after each step process. Two more steps were added here, which required the sample to be exposed to air to rinse with water and ammonia. The black squares correspond to the CIGSe sample grown on a multi-

crystalline substrate, while the red circles are the ones from CIGSe grown on GaAs (100). One can immediately see that both curves follow the same trend with only a slight discrepancy in composition with a higher concentration of Se in the As-grown and K-free cases. Such changes in content could arise from the fact that XPS measures an area of $\approx 30\,\mu$m $\times$ $30\,\mu$m combined with the multi-faceting of the CIGSe grown on the multi-crystalline substrate, bring some heterogeneity to the analyzed surface.

On the one hand, switching between facets means changing the angle between the sample surface and the detector and, consequently, the penetration depth of the XPS. Additionally, the CIGSe surface can be Cu-depleted due to the surface reconstruction, which is facet-dependent [47]. Therefore, changes in penetration depth combined with the Cu-depletion result in lower Cu and higher Se counts measured by the XPS.

On the other hand, different growth rates are expected in the multi-crystalline substrate, as seen in the topography images (see Figure 5.6), which could also produce a real change in the CIGSe composition according to the grain orientation. In any case, the observed trend is the same, which is the essential take-over message.

Figure 6.9 also confirms some of the observations made in the previous chapter. The first one is related to the initial Cu depletion at the surface, but now it was followed by the complete disappearance of Cu after K-deposition. The CGI ratio remains almost constant (≈ 0.33) until the K-deposited sample, which shows that the deposited few layers of K on the surface alone do not change the CIGSe composition at room temperature. However, as soon as the first post-annealing step was concluded, a substantial Cu depletion was observed, with Cu no longer present within the detection limit of the XPS. Cu-depletion was also observed by other authors [12], [103], [108], [109], but it is the first time that a complete depletion has been observed.

Interestingly, the amount of K remaining on the sample surface after the post-annealing is close to the amount of Cu that diffused from the sample surface. Table 6.2 summarizes this interplay, where the amount of Cu for the as-grown samples, the K-deposited + post-annealing, and the difference between them are presented. This effect happened to the Cu-poor and Cu-rich samples, in the presence or absence of GBs, and even measured in different laboratories; in summary, to the entire set of samples that were analyzed via XPS in this thesis. It is a surprise since previous reports predicted that alkali elements could passivate Cu vacancies [100], [186], but not that a complete

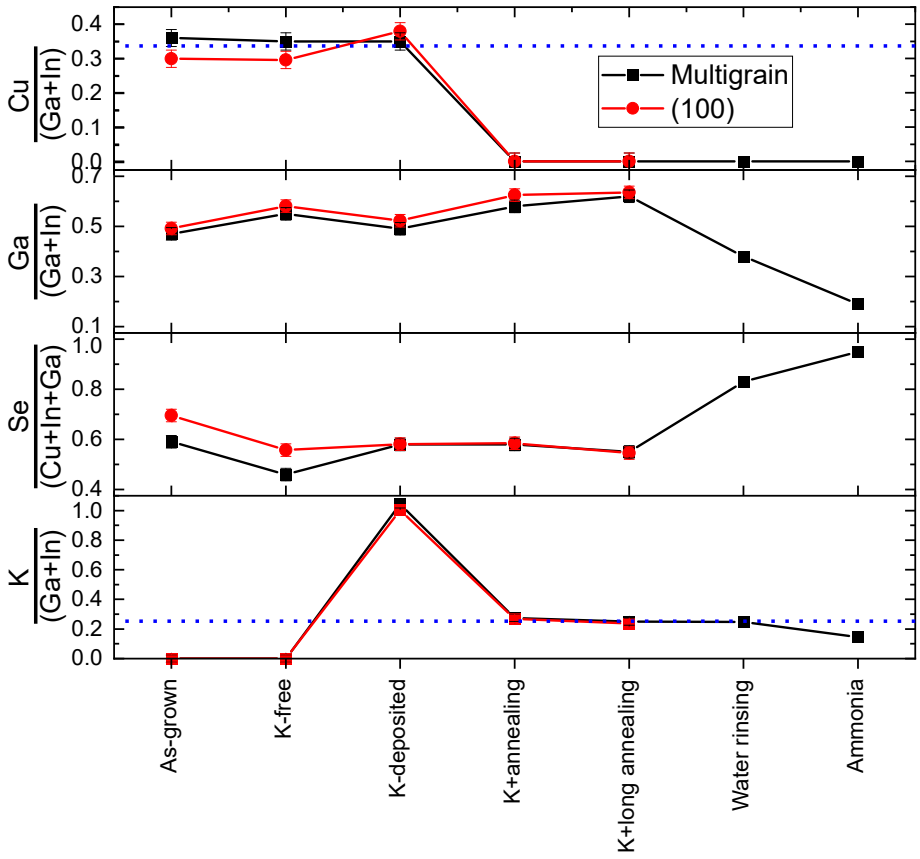

Figure 6.9: Summary of the element ratios at the surface after each step of the K-deposition for the CIGSe sample grown GaAs (100) and multi-crystalline substrates.

substitution could happen.

For the K-deposited sample, the high $K/(Ga+In)$ ratio only means that a thin layer of K on the surface is expected, with no chemical changes. Interestingly, is the constant value for $K/(Ga+In)$ ratio of ≈ 0.25 after the annealing step. A reduction in the $K/(Ga+In)$ ratio was observed only after ammonia rinsing.

Nevertheless, the results suggest that besides the passivation, the presence of K induces Cu to diffuse at 200 °C. This interplay between Cu and K also confirms the theory proposed by Herberholz *et al.* [45] in which a minimum amount of Cu (CGI = 0.25 of the OVC phase on Cu-poor CISe) is needed at the surface; otherwise, structural changes are necessary. Remember that the Cu content does not change at the surface if only the UHV annealing is done. The depletion only happened in the presence of K + annealing. When K was added, it became the element responsible for keeping the crystal structure intact. The crystal structure is destroyed when ammonia rinsing is done since it etches K from this new compound. Thus, only In and Se

	Amount of Cu			Amount of K
	As-grown	K+annealing	Difference	K+annealing
Cu-rich single-crystalline CIGSe from (section 6.2)	14.5	5	9.5	8
Cu-poor single-crystalline CIGSe from (section 6.2)	13.3	6.4	6.9	4.8
CIGSe multi-crystalline from (the current section)	17.8	0	17.8	14.8
CIGSe (100) from (the current section)	14.4	0	14.4	14.5

Table 6.2: The interplay between K and Cu after K deposition + annealing as measured via XPS.

remains at the surface, which may form oxides.

Another trend observed in the previous experiments, and Figure 6.9 makes it more evident, is the increase in Ga content after annealing steps. This trend was attributed to Ga diffusing from GaAs substrate to the CIGSe. The increase in Ga content suggests more defects in the GaAs/CIGSe interface, which could allow substitutional atoms, in this case, Cu, to diffuse into vacancies of the GaAs substrate [187]. It would make the CIGS even more Cu-depleted, explaining the even stronger depletion at the surface after K+annealing.

Finally, it was also observed a broadening of all the XPS peaks for the case where K is deposited on the surface, but without post-annealing to promote diffusion. This broadening is summarized in the Table 6.3, where the FWHM of all the elements in each step is displayed. As discussed in Figure A.3 from Appendix A.3 the increase in FWHM indicates the formation of new chemical species on the surface. However, simultaneously broadening all the peaks can also be associated with electrostatic effects [188]–[191]. Greczynski *et al.* [188], demonstrate that the measured binding energy of C 1s depends on the sample workfunction, despite the proper alignment in the

Fermi level. Therefore, K-deposition induces not only surface workfunction but also band bending and changes in the surface conductivity, and, as the film is very thin, heterogeneities should not be neglected. All these factors could broaden the measured peaks of the emitted photoelectron. Indeed, the broadening reduced when the sample was heated, and the amount of K on the surface was reduced.

Table 6.3: XPS FWHM of the samples grown on GaAs (100) and multi-crystalline substrates after each step of the K deposition.

XPS FHWM fitting curves					
CIGSe on multi-crystalline GaAs					
	Cu 2p 3/2	In 3d 5/2	Ga 2p 3/2	Se 3d 5/2	K 2p 3/2
As-grown	2.22	2.08	2.25	2.09	
K-free	2.14	1.94	2.32	1.92	
K-deposited	2.31	2.46	2.68	2.32	2.3
K + annealing		2.09	2.28	2.14	2.16
K + long annealing		2.11	2.35	2.14	2.18
CIGSe on GaAs (100)					
	Cu 2p 3/2	In 3d 5/2	Ga 2p 3/2	Se 3d 5/2	K 2p 3/2
As-grown	2.25	1.96	2.25	1.99	
K-free	2.14	1.95	2.32	2.07	
K-deposited	2.60	2.43	2.66	2.34	2.3
K + annealing		2.10	2.42	2.17	2.09
K + long annealing		2.11	2.37	2.18	2.13

Therefore, the adopted procedure for pure metallic deposition indicated that no secondary phase from alkali deposition, such as $KInSe_2$, was formed on the sample surface. Instead, the interplay between K and Cu happens, which keeps the $[Cu + K]/[In + Ga]$ ratio and, consequently, keeps the crystal structure intact.

To check if K is diffusing into the bulk or to the GB, high-resolution SIMS based on helium ion microscope HIM-SIMS was applied (for additional setup details, see Chapter 2). This machine is capable of a 3D SIMS depth profile with nanometer resolution. Appendix A.4 shows a discussion regarding the observed continuous decrease in counts

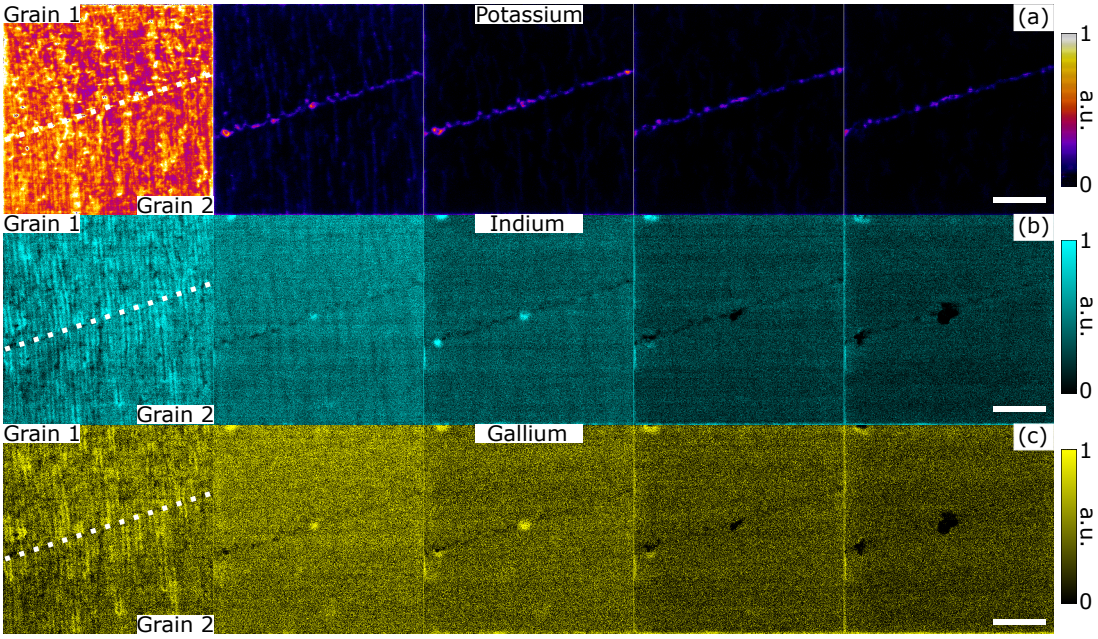

Figure 6.10: HIM-SIMS depth profile images for the K-deposited + long annealing CIGSe sample grown multi-crystalline GaAs substrates. The lateral scale bar is 2μm

for all the elements over time. This trend will not be discussed in this thesis because it is instrument-related. However, the inset graph in Figure A.4 shows a distinct decay of K compared to the other elements, confirming a K gradient in the grain interior of the CIGSe.

Figure 6.10 depicts the images for the elements acquired in positive mode (K, In, Ga). Unfortunately, Cu has a very low yield because of its low electronegativity, and only a negligible signal was observed (not shown here). The images were acquired right at the GB (between 2 macroscopic grain orientations). The first frame from left to right was acquired at the sample surface. Then the sample was etched, and another frame was acquired. The depth between the first and final images measured via AFM is $\approx$ 500 nm, resulting in 100 nm between each frame in Figure 6.10. The higher counts of K on the sample surface (first frame from Figure 6.10(a)) agree with the XPS and KPFM data. After sputtering, the K counts reduce drastically; however, a predominant contrast is observed, meaning an accumulation of K right at the GB. Conversely, the number of counts slightly decreases at the GB for indium and gallium elements.

The amount of K diffusing from the sample surface is directly linked to the number of Cu-vacancies produced by the PDT treatment. The exchange mechanism can be

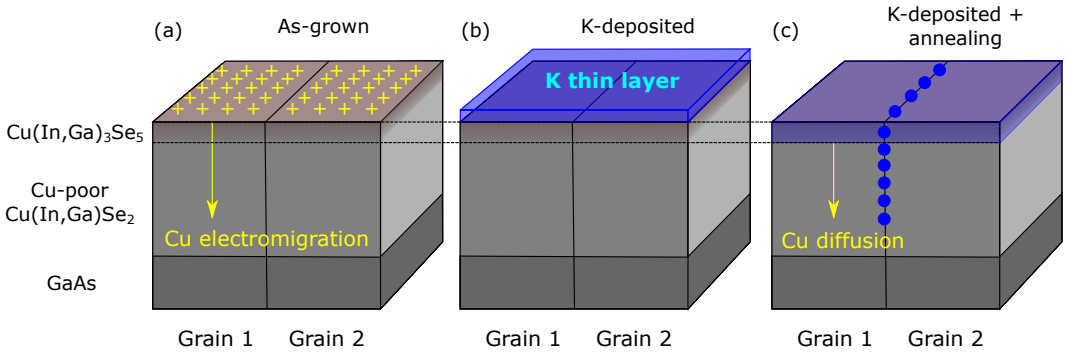

Figure 6.11: Sketch of the K diffusion mechanism on single-crystal CIGSe. (a) as-grown Cu-poor CIGSe with the presence of an OVC phase on the surface as proposed by Herberholz *et al.* [45]. (b) K-deposited sample showing a thin layer of K and no modification in the absorber composition. (c) K-deposited and the annealed sample show the complete substitution of Cu atoms by K atoms in the OVC phase, which holds the CIGSe crystal structure and promotes Cu diffusion from the OVC to the bulk.

summarized in Figure 6.11, where (a) shows an example of a Cu-poor CIGSe absorber with a Cu-depleted surface. A Cu electromigration explains the Cu-depletion from the surface due to an electric field caused by charges on the surface as proposed by Herberholz *et al.* [45]. Their model also calculated that a minimum CGI of $\approx$ 0.33 is needed to hold the crystal structure of the CIGSe, which is very similar to the values measured for the CIGSe samples presented in this section. K deposition only does not change the CGI composition of the front surface (Figure 6.11 (b)). However, as soon as an annealing step is introduced, the exchange mechanism happens (Figure 6.11 (b)). K accumulates in the GB as extensively reported and shown by the HIM-SIMS measurements. Additionally, a complete Cu substitution by K at the surface is observed. Interestingly, this exchange mechanism keeps the stoichiometry $[Cu + K]/[In + Ga]$ constant, which holds the crystal structure of the CIGSe intact. Further water and ammonia rinsing let mainly In and Se at the surface, probably binding to oxygen, destroying the surface crystal structure.

6.4 Chapter summary

In this chapter, pure metallic K was deposited on the surface of epitaxially grown CIGSe. The deposition procedure was first applied to the single-crystalline CISe grown on GaAs (100). KPFM data showed a reduction of the workfunction in 1 eV after depositing metallic K on the surface. Complete recovery of the workfunction was observed upon UHV annealing at 200 °C for 30 minutes. Combining SIMS and XPS data proved that the post-annealing step promoted K diffusion from the surface to the GaAs/CIGSe interface. Panchromatic PL imaging showed an improvement of the optoelectronic properties of the sample due K deposition.

Thus, the influence of K was investigated for the CIGSe sample epitaxially grown on a multi-crystalline GaAs substrate. Four different GBs of this sample was extensively studied via KPFM. A trend similar to the single-crystalline case was observed, except for the full recovery of the workfunction after annealing. One reason could be the amount of K deposited during the experiments. The single-crystalline CISe sample (section 6.1) had 8 Å of K on the surface, while the sample from section 6.3 had almost three times more, as measured via XPS. Interestingly, a negligible workfunction change at all the analyzed GBs was observed for the CIGSe sample grown on a multi-crystalline substrate, indicating a neutral barrier. All the samples measured via XPS were Cu-depleted at the surface. A stronger depletion was observed after K deposition plus an annealing step, which was assigned to an interplay between K and Cu atoms. XPS also showed a broadening of the peaks for all the elements after K deposition, which is most likely a consequence of different electric potential on the surface and not different species on the surface. HIM-SIMS showed a gradient of K on the grain interior and an accumulation of K at the GB.

Chapter 7

Summary and Conclusions

The focus of this thesis was to understand the nanoscale electrostatic properties of GBs in CIGS absorbers and the mechanism of potassium diffusion and passivation. SPM-based techniques were chosen as the primary tool for this investigation, and consequently, the first goal was to identify a proper measurement procedure. It was found that the vast majority of the KPFM data in the literature is based on AM-KPFM, which is known to be more prone to artifacts arising from the cantilever/sample interaction. It was believed that such artifacts would only reduce the spatial resolution of the KPFM. However, the data presented in this thesis showed that AM-KPFM is not a suitable technique to measure GB properties since the long-range electrical force acting between the KPFM cantilever and the sample produces artifacts in the measured workfunction. These artifacts are not present in the FM-KPFM mode since the electrostatic force gradient (physical property measured in FM-KPFM) is confined to the probe apex. Allied to it, measurements done under UHV conditions better control the probe sample distance, making the FM-KPFM even more reliable. Although FM-KPFM has the advantage of measuring the correct workfunction value, it cannot measure rough surfaces, limiting the application. It was not an issue for the samples analyzed in this thesis (roughly 200 nm peak to peak), and reliable workfunction measurements were acquired.

In the following, the single-crystalline CISe epitaxially grown on GaAs (100) substrate was investigated. This sample had very strong faceting on the surface due to the most energetically favorable {112} facetting. According to the facet orientation, different values for the workfunction were observed, which was related to different sur-

face terminations. Three main workfunction values were found, one associated with the {112}, another one with the (100), and a third one which is a convolution of the (112) and (100) facets.

Next, the CIGSe epitaxially grown on multi-crystalline GaAs substrate was introduced. A systematical study was carried out via KPFM and XPS measurements, proving that epitaxial growth could be done on this peculiar substrate. Two main morphological features are present on the sample surface, a pyramid-like structure, and a trench-like structure. These structures could be again associated with the most energetically favorable {112} facetting. KPFM measurements on the macroscopic GB reveal stronger contrast between grain orientations but only a shallow or almost no contrast at GB. For some GBs, lower workfunction values were found in the surroundings of the GB, which was linked to changes in topography, suggesting the presence of strain. The inert gas-transfer system adopted in this thesis proved to be an effective way of keeping the pristine condition of the samples when moving them from the MOVPE to the UHV characterization chamber, with no oxygen contamination. Additionally, carbon adsorbates were removed entirely by annealing the sample at 200 °C under UHV. However, the annealing step introduced more Ga to the surface due to diffusion from the GaAs substrate. Se depletion was also observed.

The effect of pure metallic potassium could be evaluated on the well-defined GBs of the CIGSe grown on multi-crystalline GaAs substrate. The samples were always Cu-depleted at the surface due to reconstruction, as predicted by many authors [47], [64], [168]. However, it was observed that the Cu-depletion present in the analyzed samples had a CGI threshold of 0.33, which agrees with Herberholz *et al.* for an OVC phase $Cu(In,Ga)_3Se_5$ on the surface. This threshold was defined as the minimal amount of Cu needed to keep the tetragonal crystal structure. Interestingly, the presence of K pushes Cu into the bulk, with K substituting the Cu vacancies. Additionally, K accumulates at the GBs, as already observed by many authors [17]. No material segregation or indication for a secondary-phase formation due to the addition of K was observed. It is how the crystal structure is preserved. Ammonia rinsing removed K from the surface, leading the surface with a substantial deficit of Cu and Ga and the probable formation of In and Se oxides.

Chapter 8

Outlook

The results presented in this thesis strongly contributed to a better understanding of how pure alkali elements interact with CIGSe absorbers in the absence of selenium, fluorides, and other contaminants during PDT. However, there are still many ways for improvement.

The first main contribution of this thesis was the review of the KPFM data in the literature, where most of them use AM-KPFM to measure GB of solar cells. It was demonstrated here that AM-KPFM could lead to issues when measuring GBs. Ideally, FM-KPFM under UHV should be the preferred operation mode for this application.

The observed 1:1 interplay between Cu and K could open another field of investigation for the real impact of alkali on device performance. New theoretical studies should investigate which kind of compound would be the most favorable at the surface. In the same direction, how the Cu migration from the surface to the bulk affects the device performance needs to be investigated.

The results presented in this thesis also opened a field to investigate the exchange between alkali elements. The exchange between sodium and other heavy alkali elements could be analyzed using this thesis's same approach.

The impact of oxygen could also be investigated. The UHV system used in this thesis would allow in-situ monitoring of controlled oxygen doses on the CIGSe surface.

The effect of K could also be explored using a standard polycrystalline CIGSe absorber without air exposure.

Many are the possibilities that this work opened for further understanding and improvements of alkali deposition on CIGSe absorbers.

Appendix

A.1 200°C annealing in UHV

Figure A.1 depicts a set of images of the Cu-rich CISe sample at different surface contamination level. The entire set of images was acquired under UHV conditions. Figure A.1 (a) and (d) show the topography and the workfunction maps for the sample in the as-grown condition and without air exposure. An average workfunction value of 4.63 eV was measured. The same samples was stored under UHV conditions for ≈ 20 months dropping the average workfunction to 4.35 eV (A.1 (b) and (f)). Besides the reduction in the average workfunction, the characteristic higher workfunction values according to the surface facet completely vanished. These changes are attributed to the presence of carbon adsorbates on the surface. The same sample was UHV annealed at 200 °C for 30 minutes, which removed the carbon adsorbates and brought the workfunction to values close to the as-grown condition, 4.60 eV (Figure A.1(c) and (g)). The UHV annealing step could not recover the surface workfunction to the pristine condition when the same sample was exposed to ambient conditions for six months. This result shows that UHV annealing at 200 °C for 30 minutes recovers the surface workfunction if no oxidation is present.

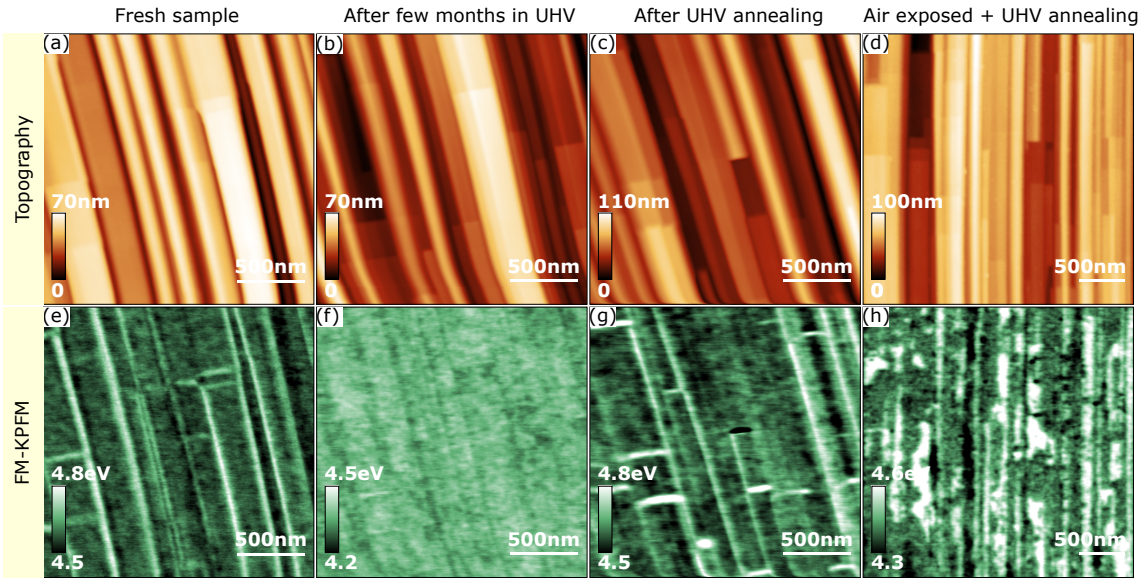

Figure A.1: Annealing effect: Topography (a-d) and FM-KPFM (e-h) images of the epitaxial CISe sample exposed to different levels of surface contamination. (a) and (e) as-grown and non-air-exposed conditions. (b), (f) the same non-air-exposed sample that was kept under UHV environment for ≈ 20 months. (c) and (g) the same aged sample after UHV annealing. (d) and (h) air-exposed sample after UHV annealing.

A.2 X-Ray sources

Auger and photoelectron peaks can sometimes overlap, causing misinterpretation of the XPS data. Overlaps will probably happen when several elements are present on the surface, in the case of CIGSe with alkali PDT, where Cu, In, Ga, Se, O, C, and K are present. One way to identify overlaps between the Auger and photoelectron peaks is by switching the X-ray sources. In this way, the Auger peaks move (in the binding energy plot) by the difference between the X-ray emission lines. For example, the Se LMM Auger peaks that appear at 299 eV and 287 eV using the Al K α source, will appear at 66 eV and 54 eV for the Mg K α source. Choosing the Al K α source can be critical for the data interpretation since potassium 2p peaks, with binding energies at 297 eV (K 2p 1/2) and 294 eV (K 2p 3/2) will overlap with Se LMM Auger peaks. Figure A.2 depicts the survey spectra acquired in the same sample using the Mg K α (blue curve) and Mg K α (red curve). The inset depicts the region where Se LMM and K 2p overlap for the Al K α but not for the Mg K α. In conclusion, switching between the X-ray sources is an effective way of dislocating undesired Auger peaks in the binding energy plots. For this reason, the Mg K α source was chosen for the in-house XPS experiments.

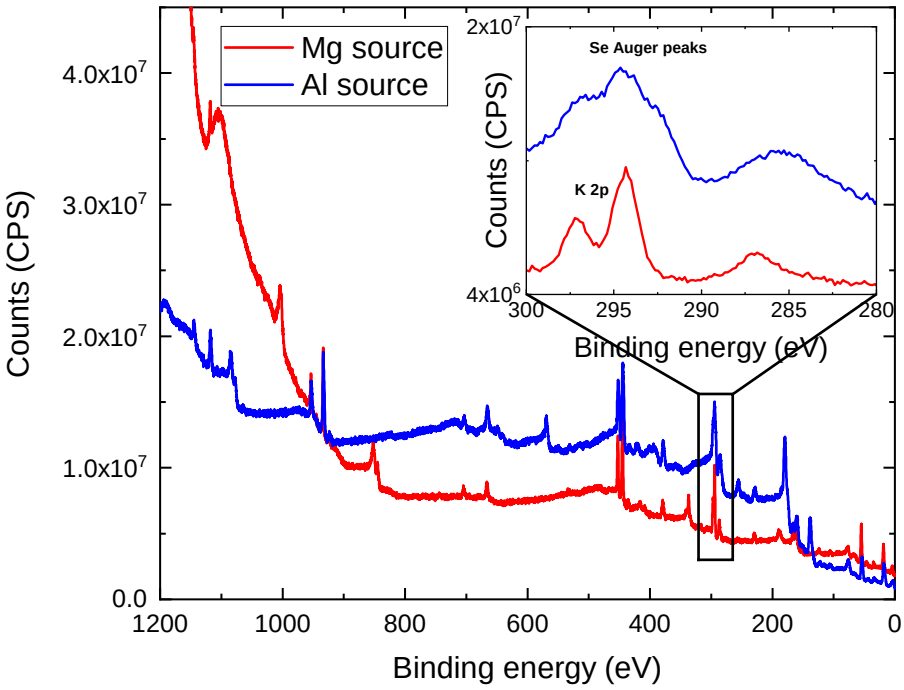

Figure A.2: Comparison between the X-ray sources. Blue curve shows the survey spectra of the CIGSe K-deposited sample acquired with the Al K α X-ray source, while red curve is using the Mg K α source. The inset graph shows the high-resolution spectra in the region of K 2p peak, where the overlap with Se LMM Auger peak happens only in the case of using Al K α X-ray source.

A.3 XPS K 2p peak during K-deposition

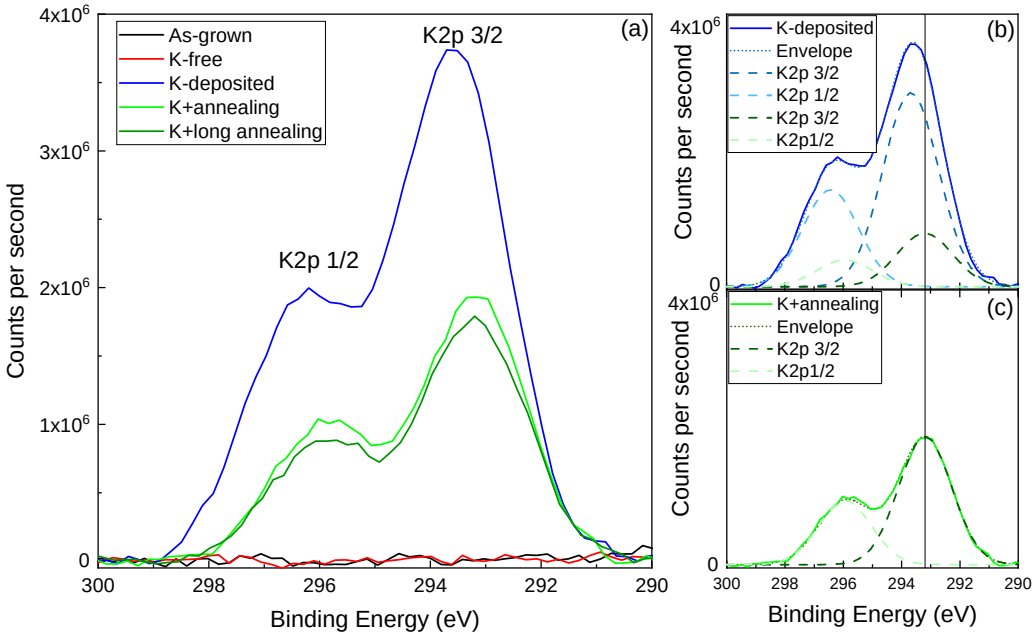

Figure A.3: XPS in the K 2p region. (a) K 2p peak after the various step of the K deposition. (b) K 2p peak of the K-deposited sample with two Gaussian peaks to fit the experimental data. (c) K 2p peak of the K+annealing sample with a single Gaussian peak to fit the experimental data.

XPS was used to investigate the chemical composition on the sample surface during the K-deposition process. Figure A.3 (a) depicts the XPS spectra of the K 2p region after each processing step. Before deposition, the doublet peaks of K 2p are not observed (see black and red lines), but these peaks are present for the K-deposited case and even after the two subsequent annealing steps. A careful observation of the K 2p peak shapes showed a broadening of the peaks for the K-deposited sample. This broadening suggests that more than one chemical species were formed as soon as K was chemisorbed on the surface, and using the same FWHM on both curves, two Gaussian are needed to fit the K-deposited curve. It can be better visualized in Figure A.3 (b) and (c), where the individual peaks for the K-deposited and the K+annealing samples are plotted. However, the broadening can also be attributed to electrostatic effects [188]–[191], which is confirmed by the peak broadening from all the CIGSe elements (see Table 6.3. Interestingly, the amount of K on the surface reduced after the first

annealing, but it did not change much from the first to the second annealing.

A.4 HIM-SIMS decay

As showed in Figure 6.10, a clear contrast at the GB of the CIGSe sample grown on GaAs multigrain substrate was observed in the HIM-SIMS images. Not that clear is the visualization of potassium in the grain interior. To check whether there is a gradient of potassium within the bulk, the average intensity of counts measured via HIM-SIMS was plotted. (Figure A.4 shows the plot of the measure count at each frame, from the surface (0 nm) up to 450 nm inside the bulk, for indium (green), gallium (yellow), and potassium. Two regions in the image were selected for potassium evaluation, one in the grain 2, called here as potassium only (pink) and another one right at the GB, called potassium at the GB (dark pink). From the plot, it is clear that a lot of potassium is present on the surface. A decay in counts for all the elements happens from 50 nm to 400 nm, this decay becomes more evident when normalizing the curves (inset graph). The decay is related to changes in the ionization current along the measurements. However, it is interesting to notice that the decay for potassium in the grain is different from the decays of the other elements. This change in decay proves that potassium diffuses into the bulk and a gradient from the surface to the back contact is observed.

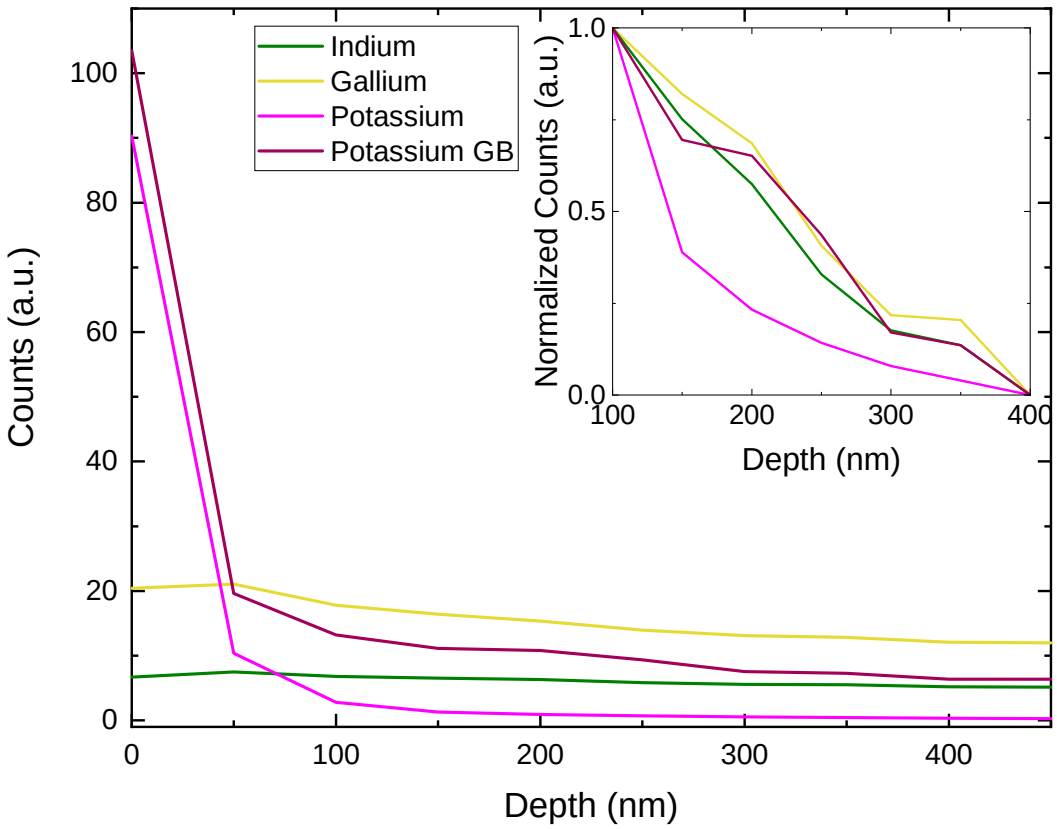

Figure A.4: HIM-SIMS decay for the elements indium, gallium, and potassium. Green and yellow curves represent indium and gallium, respectively. Potassium was split into two contributions, one in the grain (pink) and another at the GB. The inset shows the normalized counts in from 50 nm to 400 nm depth.

A.5 Raman

Raman spectroscopy was used to qualitatively identify the composition of the dots formed on the CIGSe surface, as observed in Figure 4.3. The spectra were collected with the same parameters and laser illumination (blue laser with wavelength at 442 nm at 5% of the maximum power and integrating 50 spectrum).

Figure A.5 depicts the Raman shift measured at the dot (red curve) and in the surrounding of the dot (black curve). The measured dot is depicted right in the center of the inset image. Clear differences between the spectra are observed, with the black spectra presenting a predominant peak at $177\,\mathrm{cm}^{-1}$, which is characteristic of the A_1 mode of the CIGSe [192]. The red curve, acquired in the dot, shows the presence of a peak at $179\,\mathrm{cm}^{-1}$ that could be A_1 mode of the CIGSe, but it also shows two new peaks, at $266\,\mathrm{cm}^{-1}$ and $287\,\mathrm{cm}^{-1}$. The peak at $266\,\mathrm{cm}^{-1}$ corresponds quite well with A_1 mode of Cu_2Se secondary phase. Perhaps, Peiris *et al.* [193] showed the split of the A_1 mode of CuSe under certain conditions, which could explain the second peak. However, further investigations need to be done in order to identify the origin of the peak at $287\,\mathrm{cm}^{-1}$.

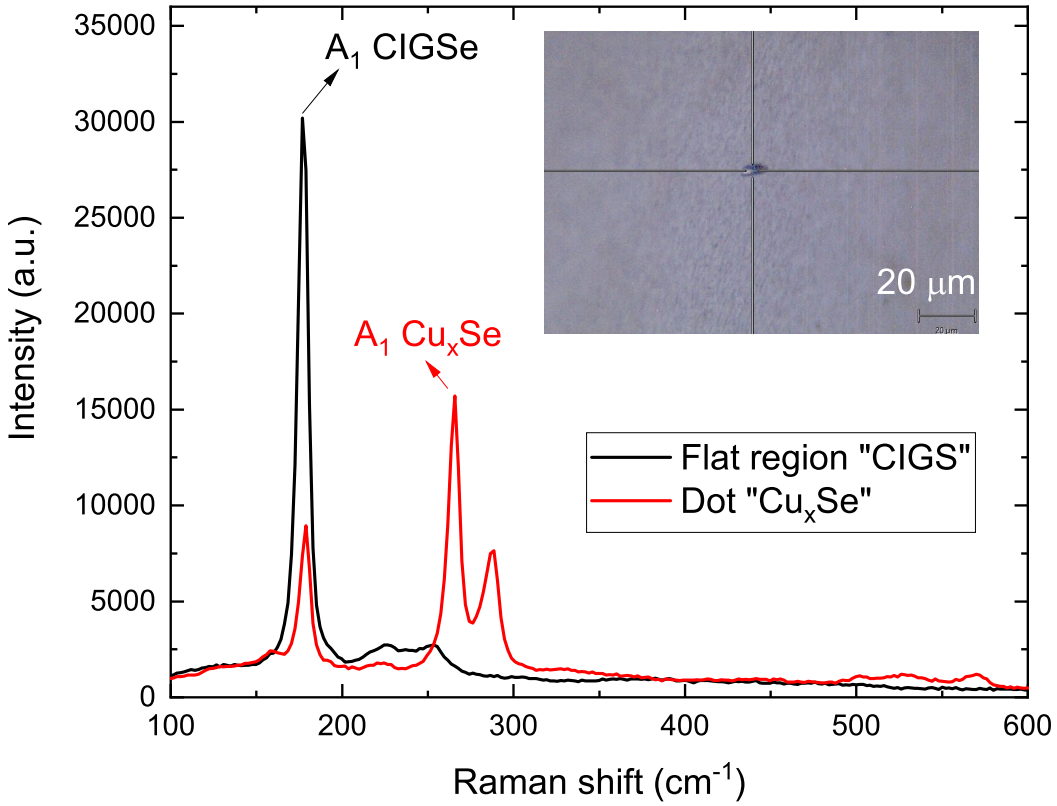

Figure A.5: Raman shift of the dots observed in Figure 4.3. The red curve shows the spectra acquired at the dot showed in the image. The black curve shows the spectra acquired in the surrounding of the dot.

A.6 Sample holder for K-deposition

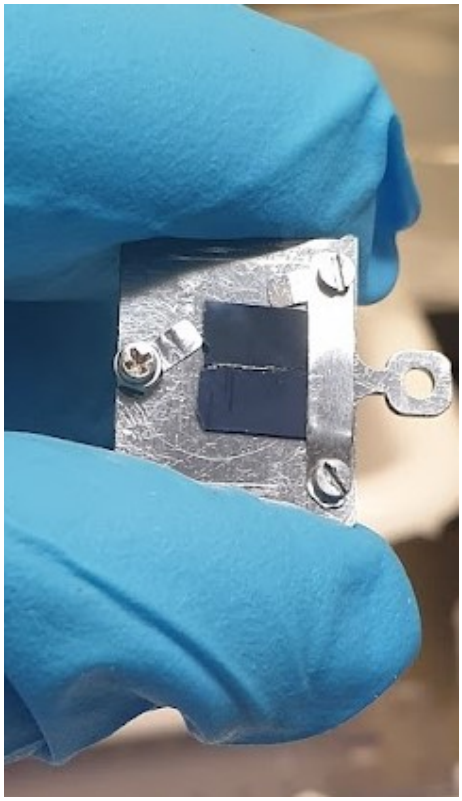

Figure A.6: Picture of the sample holder with the samples mounted for UHV experiments. GaAs (100) (up) and multi-crystalline (bottom) GaAs substrates side by side in the holder.

Publications and Presentations

List of publications (first author)

- **E. M. Lanzoni**, C. Spindler, O. Ramirez, S. Siebentritt, and Alex Redinger, " Surface characterization of epitaxial Cu-rich $CuInSe_2$ absorbers," 46th IEEE Photovoltaic Specialists Conference (PVSC), 2019. DOI: 10.1109/PVSC40753.2019.8981200

- **E. M. Lanzoni**, T. Gallet, C. Spindler, O. Ramirez, C. K. Boumenou, S. Siebentritt, and A. Redinger, " The impact of kelvin probe force microscopy operation modes and environment on grain boundary band bending in perovskite and $Cu(In,Ga)Se_2$ solar cells," Nano Energy, vol. 88, p. 106 270, 2021, DOI: https://doi.org/10.1016/j.nanoen.2021.106270.

- **E. M. Lanzoni**, O. Ramirez, H. Phirke, A. Elizabeth, H. Mönig, and A. Redinger, " Impact of metallic potassium post-deposition treatment on epitaxial $Cu(In,Ga)Se_2$," Thin Solid Films, vol. 741, p. 139 002, Jan. 1, 2022, DOI: 10.1016/j.tsf.2021.139002.

List of publications (second author)

- T. Gallet, **E. M. Lanzoni**, A. Redinger, " Effects of Annealing and Light on Co-evaporated Methylammonium Lead Iodide Perovskites using Kelvin Probe Force Microscopy in Ultra-High Vacuum " – 46th IEEE Photovoltaic Specialists Conference (PVSC), 2019. DOI: 10.1109/PVSC40753.2019.8980602

- T. Gallet, R. G. Poeira, **E. M. Lanzoni**, T. Abzieher, U. W. Paetzold, and A. Redinger, " Co-evaporation of $CH_3NH_3PbI_3$: How growth conditions impact

phase purity, photostriction, and intrinsic stability," ACS Applied Materials & Interfaces, vol. 13, no. 2, pp. 2642 - 2653, Jan. 20, 2021, Publisher: American Chemical Society, issn: 1944-8244. DOI: 10.1021/acsami.0c19038.

- O. Ramirez, **E. M. Lanzoni**, R.G. Poeira, T.P. Weiss, R. Leturcq, A. Redinger, and S. Siebentritt, "How much gallium do we need for a p-type Cu(In,Ga)Se2?" accepted for publication in APL Materials.

List of presentations

- **E. M. Lanzoni**, C. Spindler, O. Ramirez, M. Melchiorre, S. Siebentritt, and Alex Redinger, " Surface characterization of epitaxial Cu-rich $CuInSe_2$ absorbers," 46th IEEE Photovoltaic Specialists Conference (PVSC), 2019 - (Chicago - United States)

- **E. M. Lanzoni**," Overview on scanning probe microscopy (SPM)" - Permanent Seminar of the Master's program in Applied Physics, 2020 - (Medellin - Colombia).

- **E. M. Lanzoni**, T. Gallet, C. Spindler, S. Siebentritt, and A. Redinger, "Grain boundary band bending in polycrystalline materials: A Kelvin Probe Force Microscopy study" - VIRTUAL CHALCOGENIDE PV CONFERENCE (vCPVC), 2020 - (Virtual)

- **E. M. Lanzoni**, Young Scientist Tutorial on "Advanced Characterization Techniques for Thin-Film Solar Cells" - Tutorial on Scanning Probe Microscopy (SPM) - European Material Research Society (E-MRS), 2021 (Virtual)

- **E. M. Lanzoni**, O. Ramirez, A. Elizabeth, H. Mönig, S. Siebentritt, A. Redinger, "Impact of metallic potassium post-deposition treatment on epitaxial Cu(In,Ga)Se_2". - European Material Research Society (E-MRS), 2021 (Virtual)

- **E. M. Lanzoni**, O. Ramirez, S. Siebentritt, A. Redinger, "Interplay between potassium and copper on epitaxial Cu(In,Ga)Se_2 after post-deposition treatment". - European Material Research Society (E-MRS), 2022 (Virtual)

Acknowledgments

During the four years of my Ph.D., I interacted with many people in the professional field who contributed a lot to the work I developed at the University of Luxembourg. However, many other people, whom not even a single word of work was discussed, also contributed significantly to the final result of this thesis. Many thanks to all of you who made my stay in Luxembourg an environment that will be marked for life. Unfortunately, I will probably forget some of you in the acknowledgment, but if you ever interacted with me, be sure that a part of our conversations will be present in this doctoral thesis.

First, I would like to thank my supervisor, Alex Redinger, who opened the doors of the University of Luxembourg so that I could start this stage of my life. Thank you for your trust in my work since the first day I arrived in Luxembourg. You gave freedom to think outside the box and still be with my feet on the ground and do science without paradigms. Thank all the teachings, attention, and dedication you have transmitted to me and all your advises. I am very proud to have been part of this group you lead. Thank you very much.

A big thanks to CET members Susanne Siebentritt and Harry Mönig for all the teachings and suggestions they gave throughout my Ph.D. I also thank Andreas Michels and Daniel Abou-Ras, who agreed to be part of my doctoral defense.

A special thanks to all the members of the LPV group, led by Susanne Siebentritt, which provided most of the samples of this doctoral thesis. Huge thanks to Omar Ramírez, who grew most of the samples used in this thesis and shared much of his expertise in many discussions. Also, thanks to Conrad and Michele, who also prepared some samples. Many thanks to all the members of the LEM group led by Phillip Dale and the joining meeting between SPM, LPV, and LEM, from where I have learned a lot.

Thanks to all the members of the SPM group, starting from our exceptional technical team, Uli, Bernd, Robert, and Nicholas, and our administrative staff Astrid. Special thanks to the Ph.D. students and postdocs of the SPM group, the ones that I spent most of the time during work and the ones that had to listen many times 'this is an artifact'. Thibaut, Christian, Jonathan, Ricardo, Joe, Himanshu, Joana, Uzair, Jeremy, Ajay, and Rukhsar.

A special thanks to those who shared the office with me, starting with Thibaut, who was already taking care to make my stay as comfortable as possible in Luxembourg since I was still in Brazil. But who also provided me with good quality samples and discussions. Thank you so much for everything you and Julie have done for me. Big thanks to Christian and Jonathan for the many and endless discussions on the whiteboard.

Thanks to Ricardo and Joana, who contributed to my critical thinking and made my stay in Luxembourg as close as possible to Brazil in a Portuguese way. Let's not talk about language issues...

Furthermore, an endless thanks to my wife Monica, who was very supportive from the very first minute of my Ph.D. until the last second. Thank you for believing and trusting in our journey to Luxembourg. I know it was not easy for you at the beginning, but I am really proud that you accepted the challenges and we won. Thank you for discussing solar cells, SPM, XPS, SIMS, artifacts... Moreover, thank you also for fixing the many issues I faced when writing the thesis.

In the same way, an endless thanks to my family in Brazil and Colombia, who supported our choices and gave us the energy to finish these challenging tasks.

Bibliography

[1] M. Powalla, S. Paetel, D. Hariskos, R. Wuerz, F. Kessler, P. Lechner, W. Wischmann, and T. M. Friedlmeier, "Advances in cost-efficient thin-film photovoltaics based on Cu(In,Ga)Se_2," *Engineering*, vol. 3, no. 4, pp. 445–451, Aug. 2017, Publisher: Elsevier Ltd. DOI: 10.1016/J.ENG.2017.04.015 (cit. on pp. 1, 7).

[2] A. Luque López and S. Hegedus, Eds., *Handbook of photovoltaic science and engineering*, Repr, Chichester: Wiley, 2009, 1138 pp. (cit. on pp. 1, 5, 9).

[3] J. Poortmans and V. Arkhipov, *Thin Film Solar Cells: Fabrication, Characterization and Applications*. John Wiley & Sons, Oct. 2, 2006, 504 pp. (cit. on pp. 1, 4–6, 58).

[4] R. Scheer and H.-W. Schock, *Chalcogenide Photovoltaics: Physics, Technologies, and Thin Film Devices*. John Wiley & Sons, Mar. 31, 2011, 328 pp. (cit. on pp. 1, 5, 58).

[5] J. Nishinaga, T. Nagai, T. Sugaya, H. Shibata, and S. Niki, "Single-crystal Cu(In,Ga)Se_2 solar cells grown on GaAs substrates," *Applied Physics Express*, vol. 11, no. 8, p. 082 302, Jul. 19, 2018. DOI: 10.7567/APEX.11.082302 (cit. on pp. 1, 10).

[6] C. Persson and A. Zunger, "Anomalous grain boundary physics in polycrystalline $CuInSe_2$: The existence of a hole barrier," *Physical Review Letters*, vol. 91, no. 26, p. 266 401, Dec. 24, 2003, Publisher: American Physical Society. DOI: 10.1103/PhysRevLett.91.266401 (cit. on pp. 1, 11, 12).

[7] C. Persson and A. Zunger, "Compositionally induced valence-band offset at the grain boundary of polycrystalline chalcopyrites creates a hole barrier," *Applied*

Physics Letters, vol. 87, no. 21, p. 211 904, Nov. 2005. DOI: 10.1063/1.2132537 (cit. on pp. 1, 12, 96).

[8] D. Abou-Ras, C. T. Koch, V. Küstner, P. A. van Aken, U. Jahn, M. A. Contreras, R. Caballero, C. A. Kaufmann, R. Scheer, T. Unold, and H. .-W. Schock, "Grain-boundary types in chalcopyrite-type thin films and their correlations with film texture and electrical properties," *Thin Solid Films*, Thin Film Chalogenide Photovoltaic Materials (EMRS, Symposium L), vol. 517, no. 7, pp. 2545–2549, Feb. 2, 2009. DOI: 10.1016/j.tsf.2008.11.044 (cit. on pp. 1, 13, 14).

[9] U. Rau, K. Taretto, and S. Siebentritt, "Grain boundaries in Cu(In,Ga)(Se,S)$_2$ thin-film solar cells," *Applied Physics A*, vol. 96, no. 1, p. 221, Jul. 1, 2009. DOI: 10.1007/s00339-008-4978-0 (cit. on pp. 1, 11, 12, 57).

[10] S. Siebentritt, M. Igalson, C. Persson, and S. Lany, "The electronic structure of chalcopyrites—bands, point defects and grain boundaries," *Progress in Photovoltaics: Research and Applications*, vol. 18, no. 6, pp. 390–410, 2010. DOI: 10.1002/pip.936 (cit. on pp. 1, 11, 57).

[11] L. Kronik, D. Cahen, and H. W. Schock, "Effects of sodium on polycrystalline Cu(In,Ga)Se$_2$ and its solar cell performance," *Advanced Materials*, vol. 10, no. 1, pp. 31–36, 1998. DOI: 10.1002/(SICI)1521-4095(199801)10:1<31::AID-ADMA31>3.0.CO;2-3 (cit. on pp. 1, 11, 19).

[12] A. Chirilă, P. Reinhard, F. Pianezzi, P. Bloesch, A. R. Uhl, C. Fella, L. Kranz, D. Keller, C. Gretener, H. Hagendorfer, D. Jaeger, R. Erni, S. Nishiwaki, S. Buecheler, and A. N. Tiwari, "Potassium-induced surface modification of Cu(In,Ga)Se$_2$ thin films for high-efficiency solar cells," *Nature Materials*, vol. 12, no. 12, pp. 1107–1111, Dec. 2013. DOI: 10.1038/nmat3789 (cit. on pp. 1, 20, 110, 115).

[13] A. Laemmle, R. Wuerz, and M. Powalla, "Efficiency enhancement of Cu(In,Ga)Se$_2$ thin-film solar cells by a post-deposition treatment with potassium fluoride," *physica status solidi (RRL) – Rapid Research Letters*, vol. 7, no. 9, pp. 631–634, 2013, _eprint: https://onlinelibrary.wiley.com/doi/pdf/10.1002/pssr.201307238. DOI: 10.1002/pssr.201307238 (cit. on pp. 1, 20).

[14] L. Mansfield, R. Noufi, C. Muzzillo, C. Dehart, K. Bowers, B. To, J. Pankow, R. Reedy, and K. Ramanathan, "Enhanced performance in Cu(In,Ga)Se_2 solar cells fabricated by the two-step selenization process with a potassium fluoride postdeposition treatment," *IEEE Journal of Photovoltaics*, vol. 4, no. 6, pp. 1650–1654, 2014. DOI: 10.1109/JPHOTOV.2014.2354259 (cit. on pp. 1, 20).

[15] P. Jackson, R. Wuerz, D. Hariskos, E. Lotter, W. Witte, and M. Powalla, "Effects of heavy alkali elements in Cu(In,Ga)Se_2 solar cells with efficiencies up to 22.6%," *physica status solidi (RRL) – Rapid Research Letters*, vol. 10, no. 8, pp. 583–586, 2016. DOI: 10.1002/pssr.201600199 (cit. on pp. 1, 19).

[16] C. P. Muzzillo, "Review of grain interior, grain boundary, and interface effects of k in CIGS solar cells: Mechanisms for performance enhancement," *Solar Energy Materials and Solar Cells*, vol. 172, pp. 18–24, C Dec. 2017, Publisher: Elsevier B.V. DOI: 10.1016/j.solmat.2017.07.006 (cit. on pp. 1, 20).

[17] S. Siebentritt, E. Avancini, M. Bär, J. Bombsch, E. Bourgeois, S. Buecheler, R. Carron, C. Castro, S. Duguay, R. Félix, E. Handick, D. Hariskos, V. Havu, P. Jackson, H.-P. Komsa, T. Kunze, M. Malitckaya, R. Menozzi, M. Nesladek, N. Nicoara, M. Puska, M. Raghuwanshi, P. Pareige, S. Sadewasser, G. Sozzi, A. N. Tiwari, S. Ueda, A. Vilalta-Clemente, T. P. Weiss, F. Werner, R. G. Wilks, W. Witte, and M. H. Wolter, "Heavy alkali treatment of Cu(In,Ga)Se_2 solar cells: Surface versus bulk effects," *Advanced Energy Materials*, vol. 10, no. 8, p. 1 903 752, 2020. DOI: 10.1002/aenm.201903752 (cit. on pp. 1, 19–21, 102, 112, 123).

[18] Becquerel, "Recherches sur les effets de la radiation chimique de la lumiere solaire au moyen des courants electriques," *Comptes Rendus de L´Academie des Sciences*, vol. 9, pp. 145–149, 1839 (cit. on p. 3).

[19] W. G. Adams and R. E. Day, "V. the action of light on selenium," *Proceedings of the Royal Society of London*, vol. 25, no. 171, pp. 113–117, Jan. 1877, Publisher: Royal Society. DOI: 10.1098/rspl.1876.0024 (cit. on p. 3).

[20] Fritts, "On a new form of selenium photocell," *American J. of Science*, vol. 26, p. 465, 1883 (cit. on p. 3).

[21] A. Einstein, "Über einen die erzeugung und verwandlung des lichtes betreffenden heuristischen gesichtspunkt," *Annalen der Physik*, vol. 322, no. 6, pp. 132–148, 1905. DOI: 10.1002/andp.19053220607 (cit. on p. 4).

[22] L. O. Grondahl, "The copper-cuprous-oxide rectifier and photoelectric cell," *Reviews of Modern Physics*, vol. 5, no. 2, pp. 141–168, Apr. 1, 1933, Publisher: American Physical Society. DOI: 10.1103/RevModPhys.5.141 (cit. on p. 4).

[23] W. Schottky, "Halbleitertheorie der Sperrschicht," *Naturwissenschaften*, vol. 26, no. 52, pp. 843–843, Dec. 1, 1938. DOI: 10.1007/BF01774216 (cit. on p. 4).

[24] M. Green, "Photovoltaics: Coming of age," in *IEEE Conference on Photovoltaic Specialists*, May 1990, 1–8 vol.1. DOI: 10.1109/PVSC.1990.111582 (cit. on pp. 4, 5).

[25] R. S. Ohl, "Light-sensitive electric device including silicon," U.S. Patent 2443542A, Jun. 15, 1948 (cit. on p. 4).

[26] W. Shockley, "The theory of p-n junctions in semiconductors and p-n junction transistors," *The Bell System Technical Journal*, vol. 28, no. 3, pp. 435–489, Jul. 1949, Conference Name: The Bell System Technical Journal. DOI: 10.1002/j.1538-7305.1949.tb03645.x (cit. on pp. 4–6).

[27] D. M. Chapin, C. S. Fuller, and G. L. Pearson, "A new silicon p-n junction photocell for converting solar radiation into electrical power," *Journal of Applied Physics*, vol. 25, no. 5, pp. 676–677, May 1954, Publisher: American Institute of Physics. DOI: 10.1063/1.1721711 (cit. on p. 4).

[28] D. C. Reynolds, G. Leies, L. L. Antes, and R. E. Marburger, "Photovoltaic effect in cadmium sulfide," *Physical Review*, vol. 96, no. 2, pp. 533–534, Oct. 15, 1954, Publisher: American Physical Society. DOI: 10.1103/PhysRev.96.533 (cit. on p. 4).

[29] D. A. Jenny, J. J. Loferski, and P. Rappaport, "Photovoltaic effect in GaAs p-n junctions and solar energy conversion," *Physical Review*, vol. 101, no. 3, pp. 1208–1209, Feb. 1, 1956, Publisher: American Physical Society. DOI: 10.1103/PhysRev.101.1208 (cit. on p. 4).

[30] M. Green, E. Dunlop, J. Hohl-Ebinger, M. Yoshita, N. Kopidakis, and X. Hao, "Solar cell efficiency tables (version 57)," *Progress in Photovoltaics: Research and Applications*, vol. 29, no. 1, pp. 3–15, Jan. 2021, Publisher: John Wiley and Sons Ltd. DOI: 10.1002/pip.3371 (cit. on pp. 4–7, 11).

[31] A. Polman, M. Knight, E. C. Garnett, B. Ehrler, and W. C. Sinke, "Photovoltaic materials: Present efficiencies and future challenges," *Science*, vol. 352, no. 6283, aad4424, Apr. 15, 2016. DOI: 10.1126/science.aad4424 (cit. on pp. 4, 6, 7).

[32] M. Powalla, S. Paetel, E. Ahlswede, R. Wuerz, C. D. Wessendorf, and T. Magorian Friedlmeier, "Thin-film solar cells exceeding 22% solar cell efficiency: An overview on CdTe-, Cu(In,Ga)Se_2-, and perovskite-based materials," *Applied Physics Reviews*, vol. 5, no. 4, p. 041 602, Dec. 2018, Publisher: American Institute of Physics. DOI: 10.1063/1.5061809 (cit. on pp. 4, 7).

[33] F. Creutzig, P. Agoston, J. C. Goldschmidt, G. Luderer, G. Nemet, and R. C. Pietzcker, "The underestimated potential of solar energy to mitigate climate change," *Nature Energy*, vol. 2, no. 9, pp. 1–9, Aug. 25, 2017, Number: 9 Publisher: Nature Publishing Group. DOI: 10.1038/nenergy.2017.140 (cit. on p. 4).

[34] H. Ritchie, M. Roser, and P. Rosado, "Energy," *Our World in Data*, Nov. 28, 2020 (cit. on pp. 4, 5).

[35] T. Kirchartz and U. Rau, "What makes a good solar cell?" *Advanced Energy Materials*, vol. 8, no. 28, p. 1 703 385, 2018. DOI: 10.1002/aenm.201703385 (cit. on pp. 4, 5, 58).

[36] J. Nelson, *The Physics of Solar Cells*. Imperial College Press, 2003, 384 pp. (cit. on p. 5).

[37] M. Yamaguchi, *High-Efficiency GaAs-Based Solar Cells*. IntechOpen, Nov. 9, 2020, Publication Title: Post-Transition Metals. DOI: 10.5772/intechopen.94365 (cit. on pp. 5, 6).

[38] K. L. Chopra and S. R. Das, *Thin Film Solar Cells*. Boston, MA: Springer US, 1983. DOI: 10.1007/978-1-4899-0418-8 (cit. on p. 6).

[39] T. Unold and C. A. Kaufmann, "1.18 - chalcopyrite thin-film materials and solar cells," in *Comprehensive Renewable Energy*, A. Sayigh, Ed., Oxford: Elsevier, Jan. 1, 2012, pp. 399–422. DOI: 10.1016/B978-0-08-087872-0.00121-9 (cit. on pp. 6, 7, 12).

[40] S. R. Kurtz and R. McConnell, "Requirements for a 20%-efficient polycrystalline GaAs solar cell," *AIP Conference Proceedings*, vol. 404, no. 1, pp. 191–205, Apr. 5, 1997, Publisher: American Institute of Physics. DOI: 10.1063/1.53447 (cit. on pp. 7, 11).

[41] K. Kumari and S. Avasthi, "Grain boundaries in thin-film polycrystalline GaAs solar cells: A simulation study," in *2017 IEEE 44th Photovoltaic Specialist Conference (PVSC)*, Jun. 2017, pp. 251–254. DOI: 10.1109/PVSC.2017.8366277 (cit. on pp. 7, 11).

[42] S. Wagner, J. L. Shay, P. Migliorato, and H. M. Kasper, "$CuInSe_2$/CdS heterojunction photovoltaic detectors," *Applied Physics Letters*, vol. 25, no. 8, pp. 434–435, Oct. 15, 1974, Publisher: American Institute of Physics. DOI: 10.1063/1.1655537 (cit. on p. 8).

[43] M. Edoff, T. Törndahl, F. Larsson, O. Stolt, N. Shariati-Nilsson, and L. Stolt, "Post deposition treatments of (Ag,Cu)(In,Ga)Se_2 thin films for solar cells," in *2019 IEEE 46th Photovoltaic Specialists Conference (PVSC)*, ISSN: 0160-8371, Jun. 2019, pp. 0618–0621. DOI: 10.1109/PVSC40753.2019.8981287 (cit. on pp. 8, 20).

[44] D. Schmid, M. Ruckh, F. Grunwald, and H. W. Schock, "Chalcopyrite/defect chalcopyrite heterojunctions on the basis of $CuInSe_2$," *Journal of Applied Physics*, vol. 73, no. 6, pp. 2902–2909, Mar. 15, 1993, Publisher: American Institute of Physics. DOI: 10.1063/1.353020 (cit. on p. 9).

[45] R. Herberholz, U. Rau, H. W. Schock, T. Haalboom, T. Gödecke, F. Ernst, C. Beilharz, K. W. Benz, and D. Cahen, "Phase segregation, cu migration and junction formation in Cu(In,Ga)Se_2," *The European Physical Journal Applied Physics*, vol. 6, no. 2, pp. 131–139, May 1, 1999, Number: 2 Publisher: EDP Sciences. DOI: 10.1051/epjap:1999162 (cit. on pp. 9, 99, 116, 120, 123).

[46] M. Nakamura, K. Yamaguchi, Y. Kimoto, Y. Yasaki, T. Kato, and H. Sugimoto, "Cd-free Cu(In,Ga)(Se,S)$_2$ thin-film solar cell with record efficiency of 23.35%," *IEEE Journal of Photovoltaics*, vol. 9, no. 6, pp. 1863–1867, Nov. 2019, Conference Name: IEEE Journal of Photovoltaics. DOI: 10.1109/JPHOTOV.2019.2937218 (cit. on pp. 10, 19).

[47] D. Liao and A. Rockett, "Epitaxial growth of Cu(In,Ga)Se$_2$ on GaAs (110)," *Journal of Applied Physics*, vol. 91, no. 4, pp. 1978–1983, Jan. 29, 2002. DOI: 10.1063/1.1434549 (cit. on pp. 10, 92, 98, 115, 123).

[48] S. Siebentritt, N. Papathanasiou, J. Albert, and M. C. Lux-Steiner, "Stability of surfaces in the chalcopyrite system," *Applied Physics Letters*, vol. 88, no. 15, p. 151 919, Apr. 10, 2006, Publisher: American Institute of Physics. DOI: 10.1063/1.2192638 (cit. on pp. 10, 63, 78, 80, 82, 92).

[49] D. Regesch, "Photoluminescence and solar cell studies of chalcopyrites - comparison of Cu-rich vs Cu-poor and polycrystalline vs epitaxial material," Ph.D. dissertation, University of Luxembourg, Luxembourg, Jan. 28, 2014 (cit. on pp. 10, 78).

[50] T. I. Kamins, "Hall mobility in chemically deposited polycrystalline silicon," *Journal of Applied Physics*, vol. 42, no. 11, pp. 4357–4365, Oct. 1971, Publisher: American Institute of Physics. DOI: 10.1063/1.1659780 (cit. on p. 11).

[51] M. E. Cowher and T. O. Sedgwick, "Chemical vapor deposited polycrystalline silicon," *Journal of The Electrochemical Society*, vol. 119, no. 11, p. 1565, Nov. 1, 1972, Publisher: IOP Publishing. DOI: 10.1149/1.2404043 (cit. on p. 11).

[52] A. L. Fripp and L. H. Slack, "Resistivity of doped polycrystalline silicon films," *Journal of The Electrochemical Society*, vol. 120, no. 1, p. 145, Jan. 1, 1973, Publisher: IOP Publishing. DOI: 10.1149/1.2403390 (cit. on p. 11).

[53] W. Siegel, G. Kühnel, and H. A. Schneider, "On the determination of the carrier concentration in large-grain polycrystalline InP, GaAs, and GaP by hall effect measurements," *physica status solidi (a)*, vol. 87, no. 2, pp. 673–681, 1985. DOI: 10.1002/pssa.2210870232 (cit. on p. 11).

[54] Y. Lo, J. Hong, M. Wu, and S. Wang, "The transport and isolation properties of polycrystalline GaAs selectively grown by molecular beam epitaxy," *IEEE Electron Device Letters*, vol. 7, no. 10, pp. 586–588, Oct. 1986, Conference Name: IEEE Electron Device Letters. DOI: 10.1109/EDL.1986.26482 (cit. on p. 11).

[55] M. K. Sharma and D. P. Joshi, "Electrical conduction model for polycrystalline GaAs films," *Journal of Applied Physics*, vol. 102, no. 3, p. 033 704, Aug. 2007, Publisher: American Institute of Physics. DOI: 10.1063/1.2736269 (cit. on p. 11).

[56] M. Hafemeister, S. Siebentritt, J. Albert, M. C. Lux-Steiner, and S. Sadewasser, "Large neutral barrier at grain boundaries in chalcopyrite thin films," *Physical Review Letters*, vol. 104, no. 19, p. 196 602, May 14, 2010. DOI: 10.1103/PhysRevLett.104.196602 (cit. on p. 11).

[57] B. Idris, Z. Rafik, D. Kamal, B. Abdessalam, and G. Faouzi, "Size and grain-boundary effects on the performance of polycrystalline CIGS-based solar cells," in *IREC2015 The Sixth International Renewable Energy Congress*, Mar. 2015, pp. 1–5. DOI: 10.1109/IREC.2015.7110920 (cit. on p. 11).

[58] S. Siebentritt, S. Sadewasser, M. Wimmer, C. Leendertz, T. Eisenbarth, and M. C. Lux-Steiner, "Evidence for a neutral grain-boundary barrier in chalcopyrites," *Physical Review Letters*, vol. 97, no. 14, Oct. 2, 2006. DOI: 10.1103/PhysRevLett.97.146601 (cit. on pp. 11, 18, 96).

[59] M. Gloeckler, J. R. Sites, and W. K. Metzger, "Grain-boundary recombination in Cu(In,Ga)Se_2 solar cells," *Journal of Applied Physics*, vol. 98, no. 11, p. 113 704, Dec. 1, 2005. DOI: 10.1063/1.2133906 (cit. on pp. 11, 12).

[60] G. Hanna, T. Glatzel, S. Sadewasser, N. Ott, H. Strunk, U. Rau, and J. Werner, "Texture and electronic activity of grain boundaries in Cu(In,Ga)Se_2 thin films," *Applied Physics A*, vol. 82, no. 1, pp. 1–7, Jan. 1, 2006. DOI: 10.1007/s00339-005-3411-1 (cit. on pp. 11, 13).

[61] D. Fuertes Marrón, S. Sadewasser, A. Meeder, T. Glatzel, and M. C. Lux-Steiner, "Electrical activity at grain boundaries of Cu(InGa)Se_2 thin films,"

Physical Review B, vol. 71, no. 3, p. 033 306, Jan. 6, 2005, Publisher: American Physical Society. DOI: 10.1103/PhysRevB.71.033306 (cit. on p. 11).

[62] R. Baier, J. Lehmann, S. Lehmann, T. Rissom, C. Alexander Kaufmann, A. Schwarzmann, Y. Rosenwaks, M. C. Lux-Steiner, and S. Sadewasser, "Electronic properties of grain boundaries in Cu(In,Ga)Se_2 thin films with various ga-contents," *Solar Energy Materials and Solar Cells*, vol. 103, pp. 86–92, Aug. 1, 2012. DOI: 10.1016/j.solmat.2012.04.002 (cit. on p. 11).

[63] R. Baier, C. Leendertz, M. C. Lux-Steiner, and S. Sadewasser, "Toward quantitative kelvin probe force microscopy of nanoscale potential distributions," *Physical Review B*, vol. 85, no. 16, p. 165 436, Apr. 19, 2012. DOI: 10.1103/PhysRevB.85.165436 (cit. on p. 11).

[64] H. Mönig, Y. Smith, R. Caballero, C. A. Kaufmann, I. Lauermann, M. C. Lux-Steiner, and S. Sadewasser, "Direct evidence for a reduced density of deep level defects at grain boundaries of Cu(InGa)Se_2 thin films," *Physical Review Letters*, vol. 105, no. 11, p. 116 802, Sep. 8, 2010, Publisher: American Physical Society. DOI: 10.1103/PhysRevLett.105.116802 (cit. on pp. 11, 15, 16, 123).

[65] D. Abou-Ras, M. A. Contreras, R. Noufi, and H. .-W. Schock, "Impact of the se evaporation rate on the microstructure and texture of Cu(In,Ga)Se_2 thin films for solar cells," *Thin Solid Films*, Thin Film Chalogenide Photovoltaic Materials (EMRS, Symposium L), vol. 517, no. 7, pp. 2218–2221, Feb. 2, 2009. DOI: 10.1016/j.tsf.2008.10.133 (cit. on p. 11).

[66] Y. Yan, C.-S. Jiang, R. Noufi, S.-H. Wei, H. R. Moutinho, and M. M. Al-Jassim, "Electrically benign behavior of grain boundaries in polycrystalline $CuInSe_2$ films," *Physical Review Letters*, vol. 99, no. 23, p. 235 504, Dec. 7, 2007, Publisher: American Physical Society. DOI: 10.1103/PhysRevLett.99.235504 (cit. on p. 11).

[67] L. Kronik, U. Rau, J.-F. Guillemoles, D. Braunger, H.-W. Schock, and D. Cahen, "Interface redox engineering of Cu(In,Ga)Se_2 – based solar cells: Oxygen, sodium, and chemical bath effects," *Thin Solid Films*, vol. 361-362, pp. 353–359, Feb. 21, 2000. DOI: 10.1016/S0040-6090(99)00768-3 (cit. on pp. 11, 19, 20).

[68] D. Cahen and R. Noufi, "Defect chemical explanation for the effect of air anneal on CdS/$CuInSe_2$ solar cell performance," *Applied Physics Letters*, vol. 54, no. 6, pp. 558–560, Feb. 6, 1989, Publisher: American Institute of Physics. DOI: 10.1063/1.100930 (cit. on p. 11).

[69] K. Taretto and U. Rau, "Numerical simulation of carrier collection and recombination at grain boundaries in Cu(In,Ga)Se_2 solar cells," *Journal of Applied Physics*, vol. 103, no. 9, p. 094 523, May 1, 2008. DOI: 10.1063/1.2917293 (cit. on p. 12).

[70] D. Abou-Ras, B. Schaffer, M. Schaffer, S. S. Schmidt, R. Caballero, and T. Unold, "Direct insight into grain boundary reconstruction in polycrystalline Cu(In,Ga)Se_2 with atomic resolution," *Physical Review Letters*, vol. 108, no. 7, p. 075 502, Feb. 15, 2012. DOI: 10.1103/PhysRevLett.108.075502 (cit. on p. 13).

[71] D. Abou-Ras, J. Dietrich, J. Kavalakkatt, M. Nichterwitz, S. S. Schmidt, C. T. Koch, R. Caballero, J. Klaer, and T. Rissom, "Analysis of Cu(In,Ga)$(S,Se)_2$ thin-film solar cells by means of electron microscopy," *Solar Energy Materials and Solar Cells*, Special Issue : Thin film and nanostructured solar cells, vol. 95, no. 6, pp. 1452–1462, Jun. 1, 2011. DOI: 10.1016/j.solmat.2010.11.008 (cit. on p. 13).

[72] M. Krause, A. Nikolaeva, M. Maiberg, P. Jackson, D. Hariskos, W. Witte, J. A. Márquez, S. Levcenko, T. Unold, R. Scheer, and D. Abou-Ras, "Microscopic origins of performance losses in highly efficient Cu(In,Ga)Se_2 thin-film solar cells," *Nature Communications*, vol. 11, no. 1, p. 4189, Aug. 21, 2020, Number: 1 Publisher: Nature Publishing Group. DOI: 10.1038/s41467-020-17507-8 (cit. on p. 13).

[73] D. Abou-Ras, S. S. Schmidt, R. Caballero, T. Unold, H.-W. Schock, C. T. Koch, B. Schaffer, M. Schaffer, P.-P. Choi, and O. Cojocaru-Mirédin, "Confined and chemically flexible grain boundaries in polycrystalline compound semiconductors," *Advanced Energy Materials*, vol. 2, no. 8, pp. 992–998, 2012. DOI: 10.1002/aenm.201100764 (cit. on p. 13).

[74] O. Cojocaru-Mirédin, P.-P. Choi, D. Abou-Ras, S. S. Schmidt, R. Caballero, and D. Raabe, "Characterization of grain boundaries in Cu(In,Ga)Se_2 films using atom-probe tomography," *IEEE Journal of Photovoltaics*, vol. 1, no. 2, pp. 207–212, Oct. 2011. DOI: 10.1109/JPHOTOV.2011.2170447 (cit. on p. 13).

[75] T. Schwarz, A. Lomuscio, S. Siebentritt, and B. Gault, "On the chemistry of grain boundaries in CuInS films," *Nano Energy*, vol. 76, p. 105 081, Oct. 2020, Publisher: Elsevier Ltd. DOI: 10.1016/j.nanoen.2020.105081 (cit. on pp. 13, 15).

[76] J. Keller, R. Schlesiger, I. Riedel, J. Parisi, G. Schmitz, A. Avellan, and T. Dalibor, "Grain boundary investigations on sulfurized Cu(In,Ga)$(S,Se)_2$ solar cells using atom probe tomography," *Solar Energy Materials and Solar Cells*, Dye Sensitized Solar Cells, Organic, Hybrid Solar Cells and New Concepts, vol. 117, pp. 592–598, Oct. 1, 2013. DOI: 10.1016/j.solmat.2013.07.034 (cit. on pp. 13, 15).

[77] C. Spindler, F. Babbe, M. H. Wolter, F. Ehré, K. Santhosh, P. Hilgert, F. Werner, and S. Siebentritt, "Electronic defects in Cu(In,Ga)Se_2: Towards a comprehensive model," *Physical Review Materials*, vol. 3, no. 9, p. 90 302, Sep. 2019, Publisher: American Physical Society. DOI: 10.1103/PhysRevMaterials.3.090302 (cit. on pp. 13, 43).

[78] D. W. DeQuilettes, W. Zhang, V. M. Burlakov, D. J. Graham, T. Leijtens, A. Osherov, H. J. Snaith, D. S. Ginger, and S. D. Stranks, "Photo-induced halide redistribution in organic–inorganic perovskite film," *Nature Communications*, vol. 7, p. 11 683, May 2016. DOI: 10.1038/ncomms11683 (cit. on p. 13).

[79] S. Sadewasser, D. Abou-Ras, D. Azulay, R. Baier, I. Balberg, D. Cahen, S. Cohen, K. Gartsman, K. Ganesan, J. Kavalakkatt, W. Li, O. Millo, T. Rissom, Y. Rosenwaks, H. .-W. Schock, A. Schwarzman, and T. Unold, "Nanometer-scale electronic and microstructural properties of grain boundaries in Cu(In,Ga)Se_2," *Thin Solid Films*, Proceedings of the EMRS 2010 Spring Meeting Symposium M: Thin Film Chalcogenide Photovoltaic Materials, vol. 519, no. 21, pp. 7341–7346, Aug. 31, 2011. DOI: 10.1016/j.tsf.2010.12.227 (cit. on p. 13).

[80] J. Hieulle, C. Stecker, R. Ohmann, L. K. Ono, and Y. Qi, "Scanning probe microscopy applied to organic–inorganic halide perovskite materials and solar cells," *Small Methods*, vol. 2, no. 1, p. 1 700 295, Jan. 1, 2018. DOI: 10.1002/smtd.201700295 (cit. on p. 13).

[81] O. Neumann, R. Brüggemann, D. Hariskos, W. Witte, and G. H. Bauer, "Photoluminescence studies of polycrystalline Cu(In,Ga)Se_2: Lateral inhomogeneities beyond abbe's diffraction limit," *Journal of Applied Physics*, vol. 118, no. 18, p. 185 311, Nov. 2015, Publisher: American Institute of Physics Inc. DOI: 10.1063/1.4935627 (cit. on p. 13).

[82] C. K. Boumenou, F. Babbe, A. Elizabeth, M. Melchiorre, C. Spindler, J. Guillot, H. Mönig, S. Siebentritt, and A. Redinger, "Passivation of the $CuInSe_2$ surface via cadmium pre-electrolyte treatment," *Physical Review Materials*, vol. 4, no. 4, p. 045 405, Apr. 15, 2020, Publisher: American Physical Society. DOI: 10.1103/PhysRevMaterials.4.045405 (cit. on pp. 13, 80, 96).

[83] S. Bröker, D. Kück, A. Timmer, I. Lauermann, B. Ümsür, D. Greiner, C. A. Kaufmann, and H. Mönig, "Correlating the local defect-level density with the macroscopic composition and energetics of chalcopyrite thin-film surfaces," *ACS Applied Materials and Interfaces*, vol. 7, no. 23, pp. 13 062–13 072, Jun. 2015, Publisher: American Chemical Society. DOI: 10.1021/acsami.5b03260 (cit. on p. 13).

[84] S. Sadewasser, T. Glatzel, M. Rusu, A. Jäger-Waldau, and M. C. Lux-Steiner, "High-resolution work function imaging of single grains of semiconductor surfaces," *Applied Physics Letters*, vol. 80, no. 16, pp. 2979–2981, Apr. 16, 2002. DOI: 10.1063/1.1471375 (cit. on pp. 13, 57, 82, 92).

[85] S. Sadewasser and T. Glatzel, Eds., *Kelvin Probe Force Microscopy: Measuring and Compensating Electrostatic Forces*, Springer Series in Surface Sciences, Berlin Heidelberg: Springer-Verlag, 2012. DOI: 10.1007/978-3-642-22566-6 (cit. on pp. 13, 40, 57, 61).

[86] C.-S. Jiang, R. Noufi, K. Ramanathan, J. A. AbuShama, H. R. Moutinho, and M. M. Al-Jassim, "Does the local built-in potential on grain boundaries of Cu(In,Ga)Se_2 thin films benefit photovoltaic performance of the device?"

Applied Physics Letters, vol. 85, no. 13, pp. 2625–2627, Sep. 27, 2004. DOI: 10.1063/1.1793346 (cit. on pp. 13, 57, 92).

[87] C.-S. Jiang, R. Noufi, J. A. AbuShama, K. Ramanathan, H. R. Moutinho, J. Pankow, and M. M. Al-Jassim, "Local built-in potential on grain boundary of Cu(In,Ga)Se_2 thin films," *Applied Physics Letters*, vol. 84, no. 18, pp. 3477–3479, Apr. 23, 2004. DOI: 10.1063/1.1737796 (cit. on pp. 17, 18, 92).

[88] N. Nicoara, T. Lepetit, L. Arzel, S. Harel, N. Barreau, and S. Sadewasser, "Effect of the KF post-deposition treatment on grain boundary properties in Cu(In,Ga)Se_2 thin films," *Scientific Reports*, vol. 7, p. 41 361, Jan. 27, 2017. DOI: 10.1038/srep41361 (cit. on pp. 19, 57, 92).

[89] N. Nicoara, R. Manaligod, P. Jackson, D. Hariskos, W. Witte, G. Sozzi, R. Menozzi, and S. Sadewasser, "Direct evidence for grain boundary passivation in Cu(In,Ga)Se_2 solar cells through alkali-fluoride post-deposition treatments," *Nature Communications*, vol. 10, no. 1, pp. 1–8, Sep. 4, 2019. DOI: 10.1038/s41467-019-11996-y (cit. on pp. 19, 57, 92).

[90] M. Chugh, T. D. Kühne, and H. Mirhosseini, "Diffusion of alkali metals in polycrystalline $CuInSe_2$ and their role in the passivation of grain boundaries," *ACS Applied Materials & Interfaces*, vol. 11, no. 16, pp. 14 821–14 829, Apr. 24, 2019, Publisher: American Chemical Society. DOI: 10.1021/acsami.9b02158 (cit. on p. 19).

[91] P. Jackson, D. Hariskos, R. Wuerz, W. Wischmann, and M. Powalla, "Compositional investigation of potassium doped Cu(In,Ga)Se_2 solar cells with efficiencies up to 20.8%," *physica status solidi (RRL) – Rapid Research Letters*, vol. 8, no. 3, pp. 219–222, 2014. DOI: 10.1002/pssr.201409040 (cit. on p. 19).

[92] J. Dye and F. Tepper. (Nov. 6, 2020). "Alkali metal," Encyclopedia Britanica. Acessed 27 Apr 2022, [Online]. Available: https://www.britannica.com/science/alkali-metal (visited on 05/25/2022) (cit. on p. 19).

[93] L. Stolt, J. Hedström, J. Kessler, M. Ruckh, K.-O. Velthaus, and H.-W. Schock, "ZnO/CdS/$CuInSe_2$ thin-film solar cells with improved performance," *Applied Physics Letters*, vol. 62, no. 6, pp. 597–599, Feb. 8, 1993, Publisher: American Institute of Physics. DOI: 10.1063/1.108867 (cit. on p. 19).

[94] J. Holz, F. Karg, and H. Von Philipsborn, "The effect of substrate impurities on the electronic conductivity in CIS thin films," in *Proceedings of the 12th european photovoltaic solar energy conference*, 1994, pp. 1592–1595 (cit. on p. 19).

[95] T. Walter, D. Hariskos, R. Herberholz, V. Nadenau, R. Schäffler, and H. W. Schock, "On the role of oxidation for the performance of Cu(In,Ga)$(S,Se)_2$ polycrystalline thin film solar cells," in *Proceedings 13th European Photovoltaic Solar Energy Conference, Nice*, 1995, pp. 1999–2002 (cit. on p. 19).

[96] C. Heske, R. Fink, E. Umbach, W. Riedl, and F. Karg, "Na-induced effects on the electronic structure and composition of Cu(In,Ga)Se_2 thin-film surfaces," *Applied Physics Letters*, vol. 68, no. 24, pp. 3431–3433, Jun. 10, 1996, Publisher: American Institute of Physics. DOI: 10.1063/1.115783 (cit. on pp. 19, 50).

[97] D. J. Schroeder and A. A. Rockett, "Electronic effects of sodium in epitaxial $CuIn_{1-x}Ga_xSe_2$," *Journal of Applied Physics*, vol. 82, no. 10, pp. 4982–4985, Nov. 15, 1997, Publisher: American Institute of Physics. DOI: 10.1063/1.366365 (cit. on p. 19).

[98] I. Khatri, H. Fukai, H. Yamaguchi, M. Sugiyama, and T. Nakada, "Effect of potassium fluoride post-deposition treatment on Cu(In,Ga)Se_2 thin films and solar cells fabricated onto sodalime glass substrates," *Solar Energy Materials and Solar Cells*, vol. 155, pp. 280–287, Oct. 1, 2016. DOI: 10.1016/j.solmat.2016.06.023 (cit. on p. 20).

[99] H. Elanzeery, F. Babbe, M. Melchiorre, A. Zelenina, and S. Siebentritt, "Potassium fluoride ex situ treatment on both Cu-rich and Cu-poor $CuInSe_2$ thin film solar cells," *IEEE Journal of Photovoltaics*, vol. 7, no. 2, pp. 684–689, Mar. 2017. DOI: 10.1109/JPHOTOV.2017.2651802 (cit. on p. 20).

[100] M. Malitckaya, H.-P. Komsa, V. Havu, and M. J. Puska, "Effect of alkali metal atom doping on the $CuInSe_2$-based solar cell absorber," *The Journal of Physical Chemistry C*, vol. 121, no. 29, pp. 15 516–15 528, Jul. 27, 2017, Publisher: American Chemical Society. DOI: 10.1021/acs.jpcc.7b03083 (cit. on pp. 20, 115).

[101] N. Taguchi, S. Tanaka, and S. Ishizuka, "Direct insights into $RbInSe_2$ formation at Cu(In,Ga)Se_2 thin film surface with RbF postdeposition treatment," *Applied Physics Letters*, vol. 113, no. 11, p. 113 903, Sep. 10, 2018, Publisher: American Institute of Physics. DOI: 10.1063/1.5044244 (cit. on p. 20).

[102] E. Handick, P. Reinhard, R. G. Wilks, F. Pianezzi, T. Kunze, D. Kreikemeyer-Lorenzo, L. Weinhardt, M. Blum, W. Yang, M. Gorgoi, E. Ikenaga, D. Gerlach, S. Ueda, Y. Yamashita, T. Chikyow, C. Heske, S. Buecheler, A. N. Tiwari, and M. Bär, "Formation of a k—in—se surface species by NaF/KF postdeposition treatment of Cu(In,Ga)Se_2 thin-film solar cell absorbers," *ACS Applied Materials & Interfaces*, vol. 9, no. 4, pp. 3581–3589, Feb. 1, 2017, Publisher: American Chemical Society. DOI: 10.1021/acsami.6b11892 (cit. on p. 20).

[103] J. Bombsch, E. Avancini, R. Carron, E. Handick, R. Garcia-Diez, C. Hartmann, R. Félix, S. Ueda, R. G. Wilks, and M. Bär, "NaF/RbF-treated Cu(In,Ga)Se_2 thin-film solar cell absorbers: Distinct surface modifications caused by two different types of rubidium chemistry," *ACS Applied Materials & Interfaces*, vol. 12, no. 31, pp. 34 941–34 948, Aug. 5, 2020, Publisher: American Chemical Society. DOI: 10.1021/acsami.0c08794 (cit. on pp. 20, 115).

[104] P. Reinhard, B. Bissig, F. Pianezzi, E. Avancini, H. Hagendorfer, D. Keller, P. Fuchs, M. Döbeli, C. Vigo, P. Crivelli, S. Nishiwaki, S. Buecheler, and A. N. Tiwari, "Features of KF and NaF postdeposition treatments of Cu(In,Ga)Se_2 absorbers for high efficiency thin film solar cells," *Chemistry of Materials*, vol. 27, no. 16, pp. 5755–5764, Aug. 25, 2015, Publisher: American Chemical Society. DOI: 10.1021/acs.chemmater.5b02335 (cit. on p. 20).

[105] E. Handick, P. Reinhard, J.-H. Alsmeier, L. Köhler, F. Pianezzi, S. Krause, M. Gorgoi, E. Ikenaga, N. Koch, R. G. Wilks, S. Buecheler, A. N. Tiwari, and M. Bär, "Potassium postdeposition treatment-induced band gap widening at Cu(In,Ga)Se_2 surfaces – reason for performance leap?" *ACS Applied Materials & Interfaces*, vol. 7, no. 49, pp. 27 414–27 420, Dec. 16, 2015, Publisher: American Chemical Society. DOI: 10.1021/acsami.5b09231 (cit. on p. 20).

[106] S. Karki, P. Paul, G. Rajan, T. Ashrafee, K. Aryal, P. Pradhan, R. Collins, A. Rockett, T. Grassman, S. Ringel, A. Arehart, and S. Marsillac, "In situ and

ex situ investigations of KF postdeposition treatment effects on CIGS solar cells," *IEEE Journal of Photovoltaics*, vol. 7, no. 2, pp. 665–669, 2017. DOI: 10.1109/JPHOTOV.2016.2637659 (cit. on p. 20).

[107] F. Pianezzi, P. Reinhard, A. Chirilă, B. Bissig, S. Nishiwaki, S. Buecheler, and A. N. Tiwari, "Unveiling the effects of post-deposition treatment with different alkaline elements on the electronic properties of CIGS thin film solar cells," *Physical Chemistry Chemical Physics*, vol. 16, no. 19, pp. 8843–8851, Apr. 16, 2014, Publisher: The Royal Society of Chemistry. DOI: 10.1039/C4CP00614C (cit. on p. 20).

[108] H. Mönig, C.-H. Fischer, A. Grimm, B. Johnson, C. A. Kaufmann, R. Caballero, I. Lauermann, and M. C. Lux-Steiner, "Surface cu-depletion of Cu(In,Ga)Se_2 thin films: Further experimental evidence for a defect-induced surface reconstruction," *Journal of Applied Physics*, vol. 107, no. 11, p. 113 540, Jun. 2010, Publisher: American Institute of Physics. DOI: 10.1063/1.3427539 (cit. on pp. 20, 115).

[109] H. Mönig, C. .-H. Fischer, R. Caballero, C. A. Kaufmann, N. Allsop, M. Gorgoi, R. Klenk, H. .-W. Schock, S. Lehmann, M. C. Lux-Steiner, and I. Lauermann, "Surface cu depletion of Cu(In,Ga)Se_2 films: An investigation by hard x-ray photoelectron spectroscopy," *Acta Materialia*, vol. 57, no. 12, pp. 3645–3651, Jul. 1, 2009. DOI: 10.1016/j.actamat.2009.04.029 (cit. on pp. 20, 115).

[110] D. Shin, J. Kim, T. Gershon, R. Mankad, M. Hopstaken, S. Guha, B. T. Ahn, and B. Shin, "Effects of the incorporation of alkali elements on Cu(In,Ga)Se_2 thin film solar cells," *Solar Energy Materials and Solar Cells*, vol. 157, pp. 695–702, Dec. 1, 2016. DOI: 10.1016/j.solmat.2016.07.015 (cit. on p. 20).

[111] A. Laemmle, R. Wuerz, and M. Powalla, "Investigation of the effect of potassium on Cu(In,Ga)Se_2 layers and solar cells," *Thin Solid Films*, E-MRS 2014 Spring Meeting, Symposium A, Thin-Film Chalcogenide Photovoltaic Materials, vol. 582, pp. 27–30, May 1, 2015. DOI: 10.1016/j.tsf.2014.10.088 (cit. on p. 20).

[112] T. Lepetit, "Influence of KF post deposition treatment on the polycrystalline Cu(In,Ga)Se_2/CdS heterojunction formation for photovoltaic application," Theses, Université de nantes, Nov. 2015 (cit. on p. 20).

[113] P. Reinhard, B. Bissig, F. Pianezzi, H. Hagendorfer, G. Sozzi, R. Menozzi, C. Gretener, S. Nishiwaki, S. Buecheler, and A. Tiwari, "Alkali-templated surface nanopatterning of chalcogenide thin films: A novel approach toward solar cells with enhanced efficiency," *Nano Letters*, vol. 15, no. 5, pp. 3334–3340, 2015. DOI: 10.1021/acs.nanolett.5b00584 (cit. on p. 20).

[114] P. Schöppe, S. Schönherr, P. Jackson, R. Wuerz, W. Wisniewski, M. Ritzer, M. Zapf, A. Johannes, C. S. Schnohr, and C. Ronning, "Overall distribution of rubidium in highly efficient Cu(In,Ga)Se_2 solar cells," *ACS Applied Materials & Interfaces*, vol. 10, no. 47, pp. 40 592–40 598, Nov. 28, 2018, Publisher: American Chemical Society. DOI: 10.1021/acsami.8b16040 (cit. on p. 22).

[115] T. Kodalle, M. D. Heinemann, D. Greiner, H. A. Yetkin, M. Klupsch, C. Li, P. A. van Aken, I. Lauermann, R. Schlatmann, and C. A. Kaufmann, "Elucidating the mechanism of an RbF post deposition treatment in CIGS thin film solar cells," *Solar RRL*, vol. 2, no. 9, p. 1 800 156, 2018. DOI: 10.1002/solr.201800156 (cit. on p. 22).

[116] C. Jiang, B. To, S. Glynn, H. Mahabaduge, T. Barnes, and M. M. Al-Jassim, "Recent progress in nanoelectrical characterizations of CdTe and Cu(In,Ga)Se_2," in *2016 IEEE 43rd Photovoltaic Specialists Conference (PVSC)*, Jun. 2016, pp. 3675–3680. DOI: 10.1109/PVSC.2016.7750361 (cit. on p. 22).

[117] D. Abou-Ras, A. Nikolaeva, S. Caicedo Dávila, M. Krause, H. Guthrey, M. Al-Jassim, M. Morawski, and R. Scheer, "No evidence for passivation effects of na and k at grain boundaries in polycrystalline Cu(In,Ga)Se_2 thin films for solar cells," *Solar RRL*, vol. 3, no. 8, p. 1 900 095, Aug. 2019, Publisher: Wiley-VCH Verlag. DOI: 10.1002/solr.201900095 (cit. on p. 23).

[118] O. Ramírez, M. Bertrand, A. Debot, D. Siopa, N. Valle, J. Schmauch, M. Melchiorre, and S. Siebentritt, "The effect of potassium fluoride postdeposition treatments on the optoelectronic properties of Cu(In,Ga)Se_2 single crystals,"

Solar RRL, vol. 5, no. 4, p. 2 000 727, 2021. DOI: 10.1002/solr.202000727 (cit. on pp. 23, 111, 112).

[119] G. Binnig, H. Rohrer, C. Gerber, and E. Weibel, "Tunneling through a controllable vacuum gap," *Applied Physics Letters*, vol. 40, no. 2, pp. 178–180, Jan. 1982. DOI: 10.1063/1.92999 (cit. on p. 24).

[120] G. Binnig, H. Rohrer, C. Gerber, and E. Weibel, "Surface Studies by Scanning Tunneling Microscopy," *Physical Review Letters*, vol. 49, no. 1, pp. 57–61, Jul. 1982. DOI: 10.1103/PhysRevLett.49.57 (cit. on p. 24).

[121] G. Binnig, C. F. Quate, and C. Gerber, "Atomic force microscope," *Physical Review Letters*, vol. 56, no. 9, pp. 930–933, Mar. 3, 1986. DOI: 10.1103/PhysRevLett.56.930 (cit. on p. 25).

[122] J. E. Stern, B. D. Terris, H. J. Mamin, and D. Rugar, "Deposition and imaging of localized charge on insulator surfaces using a force microscope," *Applied Physics Letters*, vol. 53, no. 26, pp. 2717–2719, Dec. 26, 1988. DOI: 10.1063/1.100162 (cit. on p. 25).

[123] B. D. Terris, J. E. Stern, D. Rugar, and H. J. Mamin, "Contact electrification using force microscopy," *Physical Review Letters*, vol. 63, no. 24, pp. 2669–2672, 1989. DOI: 10.1103/PhysRevLett.63.2669 (cit. on p. 25).

[124] M. Nonnenmacher, M. P. O'Boyle, and H. K. Wickramasinghe, "Kelvin probe force microscopy," *Applied Physics Letters*, vol. 58, no. 25, p. 2921, 1991. DOI: 10.1063/1.105227 (cit. on pp. 25, 35, 38).

[125] Y. Martin, D. W. Abraham, and H. K. Wickramasinghe, "High-resolution capacitance measurement and potentiometry by force microscopy," *Applied Physics Letters*, vol. 52, no. 13, p. 1103, 1988. DOI: 10.1063/1.99224 (cit. on pp. 25, 35).

[126] Y. Martin and H. K. Wickramasinghe, "Magnetic imaging by ''force microscopy'' with 1000 Å resolution," *Applied Physics Letters*, vol. 50, no. 20, pp. 1455–1457, May 18, 1987. DOI: 10.1063/1.97800 (cit. on p. 25).

[127] D. Rugar, H. J. Mamin, P. Guethner, S. E. Lambert, J. E. Stern, I. McFadyen, and T. Yogi, "Magnetic force microscopy: General principles and application to longitudinal recording media," *Journal of Applied Physics*, vol. 68, no. 3, pp. 1169–1183, Aug. 1, 1990. DOI: 10.1063/1.346713 (cit. on p. 25).

[128] D. W. Abraham, "Lateral dopant profiling in semiconductors by force microscopy using capacitive detection," *Journal of Vacuum Science & Technology B: Microelectronics and Nanometer Structures*, vol. 9, no. 2, p. 703, Mar. 1991. DOI: 10.1116/1.585536 (cit. on p. 25).

[129] U. Dürig, D. W. Pohl, and F. Rohner, "Near-field optical-scanning microscopy," *Journal of Applied Physics*, vol. 59, no. 10, pp. 3318–3327, May 15, 1986. DOI: 10.1063/1.336848 (cit. on p. 25).

[130] C. Davisson and L. H. Germer, "Diffraction of electrons by a crystal of nickel," *Physical Review*, vol. 30, no. 6, pp. 705–740, Dec. 1, 1927, Publisher: American Physical Society. DOI: 10.1103/PhysRev.30.705 (cit. on p. 25).

[131] J. Tersoff and D. R. Hamann, "Theory and application for the scanning tunneling microscope," *Physical Review Letters*, vol. 50, no. 25, pp. 1998–2001, Jun. 20, 1983, Publisher: American Physical Society. DOI: 10.1103/PhysRevLett.50.1998 (cit. on p. 28).

[132] J. Bardeen, "Tunnelling from a many-particle point of view," *Physical Review Letters*, vol. 6, no. 2, pp. 57–59, Jan. 15, 1961, Publisher: American Physical Society. DOI: 10.1103/PhysRevLett.6.57 (cit. on p. 28).

[133] C. Wagner, R. Franke, and T. Fritz, "Evaluation of I(V) curves in scanning tunneling spectroscopy of organic nanolayers," *Physical Review B*, vol. 75, no. 23, p. 235 432, Jun. 21, 2007, Publisher: American Physical Society. DOI: 10.1103/PhysRevB.75.235432 (cit. on p. 28).

[134] T. R. Albrecht and C. F. Quate, "Atomic resolution imaging of a nonconductor by atomic force microscopy," *Journal of Applied Physics*, vol. 62, no. 7, pp. 2599–2602, Oct. 1987, Publisher: American Institute of Physics. DOI: 10.1063/1.339435 (cit. on p. 30).

[135] F. Ohnesorge and G. Binnig, "True atomic resolution by atomic force microscopy through repulsive and attractive forces," *Science*, vol. 260, no. 5113, pp. 1451–1456, Jun. 4, 1993, Publisher: American Association for the Advancement of Science. DOI: 10.1126/science.260.5113.1451 (cit. on p. 30).

[136] H. Hölscher and U. D. Schwarz, "Theory of amplitude modulation atomic force microscopy with and without Q-Control," *International Journal of Non-Linear Mechanics*, Special Issue Micro-and Nanoscale Beam Dynamics, vol. 42, no. 4, pp. 608–625, May 1, 2007. DOI: 10.1016/j.ijnonlinmec.2007.01.018 (cit. on p. 31).

[137] O. E. Dagdeviren, J. Götzen, H. Hölscher, E. I. Altman, and U. D. Schwarz, "Robust high-resolution imaging and quantitative force measurement with tuned-oscillator atomic force microscopy," *Nanotechnology*, vol. 27, no. 6, p. 065 703, Jan. 2016, Publisher: IOP Publishing. DOI: 10.1088/0957-4484/27/6/065703 (cit. on p. 31).

[138] T. R. Albrecht, P. Grütter, D. Horne, and D. Rugar, "Frequency modulation detection using high-Q cantilevers for enhanced force microscope sensitivity," *Journal of Applied Physics*, vol. 69, no. 2, pp. 668–673, Jan. 15, 1991, Publisher: American Institute of Physics. DOI: 10.1063/1.347347 (cit. on p. 33).

[139] M. Saint Jean, S. Hudlet, C. Guthmann, and J. Berger, "Van der waals and capacitive forces in atomic force microscopies," *Journal of Applied Physics*, vol. 86, no. 9, pp. 5245–5248, Nov. 1, 1999, Publisher: American Institute of Physics. DOI: 10.1063/1.371506 (cit. on pp. 35, 64).

[140] J. M. R. Weaver and D. W. Abraham, "High resolution atomic force microscopy potentiometry," *Journal of Vacuum Science & Technology B: Microelectronics and Nanometer Structures Processing, Measurement, and Phenomena*, vol. 9, no. 3, pp. 1559–1561, May 1991, Publisher: American Institute of Physics. DOI: 10.1116/1.585423 (cit. on p. 35).

[141] O. A. Castañeda-Uribe, R. Reifenberger, A. Raman, and A. Avila, "Depth-sensitive subsurface imaging of polymer nanocomposites using second harmonic kelvin probe force microscopy," *ACS Nano*, vol. 9, no. 3, pp. 2938–2947, Mar. 24, 2015. DOI: 10.1021/nn507019c (cit. on p. 36).

[142] W. Melitz, J. Shen, A. C. Kummel, and S. Lee, "Kelvin probe force microscopy and its application," *Surface Science Reports*, vol. 66, no. 1, pp. 1–27, Jan. 2011. DOI: 10.1016/j.surfrep.2010.10.001 (cit. on p. 36).

[143] A. Axt, I. M. Hermes, V. W. Bergmann, N. Tausendpfund, and S. A. L. Weber, "Know your full potential: Quantitative kelvin probe force microscopy on nanoscale electrical devices," *Beilstein Journal of Nanotechnology*, vol. 9, pp. 1809–1819, Jun. 15, 2018. DOI: 10.3762/bjnano.9.172 (cit. on pp. 38, 40, 59, 61).

[144] H. Jacobs, H. Knapp, S. Müller, and A. Stemmer, "Surface potential mapping: A qualitative material contrast in SPM," *Ultramicroscopy*, vol. 69, no. 1, pp. 39–49, Aug. 1997. DOI: 10.1016/S0304-3991(97)00027-2 (cit. on pp. 38, 71).

[145] J. Colchero, A. Gil, and A. M. Baró, "Resolution enhancement and improved data interpretation in electrostatic force microscopy," *Physical Review B*, vol. 64, no. 24, p. 245 403, Nov. 28, 2001. DOI: 10.1103/PhysRevB.64.245403 (cit. on pp. 38, 39, 59, 61).

[146] T. Wagner, H. Beyer, P. Reissner, P. Mensch, H. Riel, B. Gotsmann, and A. Stemmer, "Kelvin probe force microscopy for local characterisation of active nanoelectronic devices," *Beilstein Journal of Nanotechnology*, vol. 6, no. 1, pp. 2193–2206, Nov. 2015, Publisher: Beilstein-Institut Zur Forderung der Chemischen Wissenschaften. DOI: 10.3762/bjnano.6.225 (cit. on pp. 38, 56, 69, 71).

[147] U. Dürig, O. Züger, and A. Stalder, "Interaction force detection in scanning probe microscopy: Methods and applications," *Journal of Applied Physics*, vol. 72, no. 5, pp. 1778–1798, Sep. 1992, Publisher: American Institute of Physics. DOI: 10.1063/1.352348 (cit. on p. 39).

[148] U. Zerweck, C. Loppacher, T. Otto, S. Grafström, and L. M. Eng, "Accuracy and resolution limits of kelvin probe force microscopy," *Physical Review B*, vol. 71, no. 12, p. 125 424, Mar. 25, 2005. DOI: 10.1103/PhysRevB.71.125424 (cit. on pp. 40, 59, 61, 71).

[149] J. L. Garrett and J. N. Munday, "Fast, high-resolution surface potential measurements in air with heterodyne kelvin probe force microscopy," *Nanotech-*

nology, vol. 27, no. 24, p. 245 705, May 2016, Publisher: IOP Publishing. DOI: 10.1088/0957-4484/27/24/245705 (cit. on p. 39).

[150] E. Meyer, J. H. Hans, and R. Bennewitz, *Scanning Probe Microscopy - The Lab on a Tip*, 1st ed., 1439-2674. Springer-Verlag Berlin Heidelberg, 2004, 210 pp. (cit. on pp. 40, 83).

[151] C. Julian Chen, *Introduction to Scanning Tunneling Microscopy: Second Edition - Oxford Scholarship*, 2nd, ser. Monographs on the physics and chemistry of materials 64. Oxford Univ. Press, 2007 (cit. on p. 40).

[152] B. Bhushan, *Scanning Probe Microscopy in Nanoscience and Nanotechnology 2*, 1st ed. Springer-Verlag Berlin, 2011, vol. 116, 956 pp., ISSN: 14344904 Publication Title: NanoScience and Technology (cit. on p. 40).

[153] C. Spindler, "Optical detection of deep defects in Cu(In,Ga)Se_2," Ph.D. dissertation, University of Luxembourg, Luxembourg, Luxembourg, Jun. 7, 2018 (cit. on p. 43).

[154] T. Gallet, "Co-evaporation and scanning probe microscopy characterizations of hybrid halide perovskite thin films for solar cells," Ph.D. dissertation, University of Luxembourg, Luxembourg, Luxembourg, Nov. 26, 2021 (cit. on p. 43).

[155] "User operation manual EA-15 energy analyser rev. 1.1," 1070142, Jun. 2018 (cit. on pp. 48–50).

[156] C. J. Powell and A. Jablonski, "Surface and microanalysis science division national institute of standards and technology gaithersburg, MD, USA," p. 47, 2010 (cit. on pp. 47, 107).

[157] J. F. Moulder, *Handbook of X-ray Photoelectron Spectroscopy: A Reference Book of Standard Spectra for Identification and Interpretation of XPS Data*. Physical Electronics Division, Perkin-Elmer Corporation, 1992, 261 pp. (cit. on pp. 47, 98).

[158] E. M. Lanzoni, O. Ramírez, H. Phirke, A. Elizabeth, H. Mönig, and A. Redinger, "Impact of metallic potassium post-deposition treatment on epitaxial Cu(In,Ga)Se_2," *Thin Solid Films*, vol. 741, p. 139 002, Jan. 1, 2022. DOI: 10.1016/j.tsf.2021.139002 (cit. on pp. 54, 102, 111).

[159] T. Wirtz, O. De Castro, J.-N. Audinot, and P. Philipp, "Imaging and analytics on the helium ion microscope," *Annual Review of Analytical Chemistry*, vol. 12, no. 1, pp. 523–543, 2019, _eprint: https://doi.org/10.1146/annurev-anchem-061318-115457. DOI: 10.1146/annurev-anchem-061318-115457 (cit. on p. 55).

[160] E. M. Lanzoni, T. Gallet, C. Spindler, O. Ramírez, C. K. Boumenou, S. Siebentritt, and A. Redinger, "The impact of kelvin probe force microscopy operation modes and environment on grain boundary band bending in perovskite and Cu(In,Ga)Se_2 solar cells," *Nano Energy*, vol. 88, p. 106 270, 2021. DOI: https://doi.org/10.1016/j.nanoen.2021.106270 (cit. on pp. 57, 59, 60, 62, 66–68, 70, 73, 74).

[161] N. Adhikari, A. Dubey, D. Khatiwada, A. F. Mitul, Q. Wang, S. Venkatesan, A. Iefanova, J. Zai, X. Qian, M. Kumar, and Q. Qiao, "Interfacial study to suppress charge carrier recombination for high efficiency perovskite solar cells," *ACS Applied Materials & Interfaces*, vol. 7, no. 48, pp. 26 445–26 454, Dec. 9, 2015. DOI: 10.1021/acsami.5b09797 (cit. on p. 57).

[162] N. Nicoara, S. Harel, T. Lepetit, L. Arzel, N. Barreau, and S. Sadewasser, "Impact of KF post-deposition treatment on aging of the Cu(In,Ga)Se_2 surface and its interface with CdS," *ACS Applied Energy Materials*, vol. 1, no. 6, pp. 2681–2688, Jun. 25, 2018. DOI: 10.1021/acsaem.8b00365 (cit. on p. 57).

[163] N. D. Lang and W. Kohn, "Theory of metal surfaces: Work function," *Physical Review B*, vol. 3, no. 4, pp. 1215–1223, Feb. 15, 1971, Publisher: American Physical Society. DOI: 10.1103/PhysRevB.3.1215 (cit. on pp. 60, 103, 113).

[164] H. Sugimura, Y. Ishida, K. Hayashi, O. Takai, and N. Nakagiri, "Potential shielding by the surface water layer in kelvin probe force microscopy," *Applied Physics Letters*, vol. 80, no. 8, pp. 1459–1461, 2002. DOI: 10.1063/1.1455145 (cit. on pp. 61, 64).

[165] F. C. Salomão, E. Lanzoni, C. Costa, C. Deneke, and E. B. Barros, "Determination of high frequency dielectric constant and surface potential of graphene oxide and influence of humidity by KPFM.," *Langmuir*, Sep. 22, 2015. DOI: 10.1021/acs.langmuir.5b01786 (cit. on pp. 61, 64).

[166] T. A. d. L. Burgo, C. A. Rezende, S. Bertazzo, A. Galembeck, and F. Galembeck, "Electric potential decay on polyethylene: Role of atmospheric water on electric charge build-up and dissipation," *Journal of Electrostatics*, vol. 69, no. 4, pp. 401–409, Aug. 2011. DOI: 10.1016/j.elstat.2011.05.005 (cit. on pp. 61, 64).

[167] T. Glatzel, S. Sadewasser, and M. C. Lux-Steiner, "Amplitude or frequency modulation-detection in kelvin probe force microscopy," *Applied Surface Science*, 5th International Conference on non-contact AFM in Montreal, Canada, vol. 210, no. 1, pp. 84–89, Mar. 31, 2003. DOI: 10.1016/S0169-4332(02)01484-8 (cit. on pp. 61, 71).

[168] J. E. Jaffe and A. Zunger, "Defect-induced nonpolar-to-polar transition at the surface of chalcopyrite semiconductors," *Physical Review B*, vol. 64, no. 24, p. 241 304, Nov. 29, 2001. DOI: 10.1103/PhysRevB.64.241304 (cit. on pp. 63, 80, 82, 92, 98, 123).

[169] L. F. Zagonel, M. Bäurer, A. Bailly, O. Renault, M. Hoffmann, S.-J. Shih, D. Cockayne, and N. Barrett, "Orientation-dependent work function of in situ annealed strontium titanate," *Journal of Physics: Condensed Matter*, vol. 21, no. 31, p. 314 013, 2009. DOI: 10.1088/0953-8984/21/31/314013 (cit. on p. 67).

[170] E. M. Lanzoni, C. Spindler, O. Ramirez, S. Siebentritt, and Alex Redinger, "Surface characterization of epitaxial Cu-rich $CuInSe_2$ absorbers," in *2019 46th IEEE Photovoltaic Specialists Conference*, (In press), 2019 (cit. on pp. 76, 79, 81).

[171] P. Fons, S. Niki, A. Yamada, and H. Oyanagi, "Direct observation of the Cu_2-xSe phase of Cu-rich epitaxial $CuInSe_2$ grown on GaAs (001)," *Journal of Applied Physics*, vol. 84, no. 12, pp. 6926–6928, Nov. 25, 1998. DOI: 10.1063/1.368991 (cit. on p. 78).

[172] R. D. Heyding and R. M. Murray, "The crystal structures of Cu1.8Se, Cu_3Se_2, alpha- and gamma-CuSe, $CuSe_2$, and $CuSe_2$II," *Canadian Journal of Chemistry*, vol. 54, no. 6, pp. 841–848, Mar. 15, 1976, Publisher: NRC Research Press. DOI: 10.1139/v76-122 (cit. on p. 78).

[173] Y. Aida, V. Depredurand, J. K. Larsen, H. Arai, D. Tanaka, M. Kurihara, and S. Siebentritt, "Cu-rich $CuInSe_2$ solar cells with a Cu-poor surface," *Progress in Photovoltaics: Research and Applications*, vol. 23, no. 6, pp. 754–764, 2015. DOI: 10.1002/pip.2493 (cit. on p. 78).

[174] Y. Hashimoto, N. Kohara, T. Negami, M. N. M. Nishitani, and T. W. T. Wada, "Surface characterization of chemically treated $Cu(In,Ga)Se_2$ thin films," *Japanese Journal of Applied Physics*, vol. 35, no. 9, p. 4760, Sep. 1, 1996, Publisher: IOP Publishing. DOI: 10.1143/JJAP.35.4760 (cit. on p. 78).

[175] H. Elanzeery, M. Melchiorre, M. Sood, F. Babbe, F. Werner, G. Brammertz, and S. Siebentritt, "Challenge in Cu-rich $CuInSe_2$ thin film solar cells: Defect caused by etching," *Physical Review Materials*, vol. 3, no. 5, p. 055 403, May 16, 2019. DOI: 10.1103/PhysRevMaterials.3.055403 (cit. on p. 80).

[176] L.-C. Yang, G. S. Chen, and A. Rockett, "Surface polarities of sputtered epitaxial $CuInSe_2$ and $Cu_1In_3Se_5$ thin films grown on GaAs (001) substrates," *Applied Physics Letters*, vol. 86, no. 20, p. 201 907, May 16, 2005. DOI: 10.1063/1.1929071 (cit. on p. 80).

[177] D. Nečas, M. Valtr, and P. Klapetek, "How levelling and scan line corrections ruin roughness measurement and how to prevent it," *Scientific Reports*, vol. 10, p. 15 294, Sep. 17, 2020. DOI: 10.1038/s41598-020-72171-8 (cit. on p. 83).

[178] D. Yi, J. Li, and P. Zhu, "Study of nanoscratching process of GaAs using molecular dynamics," *Crystals*, vol. 8, no. 8, p. 321, Aug. 2018, Number: 8 Publisher: Multidisciplinary Digital Publishing Institute. DOI: 10.3390/cryst8080321 (cit. on p. 85).

[179] R. Hunger, C. Pettenkofer, and R. Scheer, "Surface properties of (111), (001), and (110)-oriented epitaxial $CuInS_2$/Si films," *Surface Science*, vol. 477, no. 1, pp. 76–93, Apr. 10, 2001. DOI: 10.1016/S0039-6028(01)00707-5 (cit. on p. 92).

[180] A. Kahn, "Fermi level, work function and vacuum level," *Materials Horizons*, vol. 3, no. 1, pp. 7–10, 2016. DOI: 10.1039/C5MH00160A (cit. on p. 96).

[181] H. Mönig, D. Lockhorn, N. Aghdassi, A. Timmer, C. A. Kaufmann, R. Caballero, H. Zacharias, and H. Fuchs, "Heat induced passivation of $CuInSe_2$ surfaces: A strategy to optimize the efficiency of chalcopyrite thin film solar cells?" *Advanced Materials Interfaces*, vol. 1, no. 2, p. 1 300 040, 2014. DOI: 10.1002/admi.201300040 (cit. on p. 96).

[182] L. Zhang, D. Zhuang, M. Zhao, Q. Gong, L. Guo, L. Ouyang, R. Sun, Y. Wei, and S. Zhan, "The effects of annealing temperature on CIGS solar cells by sputtering from quaternary target with Se-free post annealing," *Applied Surface Science*, vol. 413, pp. 175–180, Aug. 15, 2017. DOI: 10.1016/j.apsusc.2017.03.289 (cit. on p. 98).

[183] S. B. Zhang and S.-H. Wei, "Reconstruction and energetics of the polar (112) and $(1\bar{1}\bar{2})$ versus the nonpolar (220) surfaces of $CuInSe_2$," *Physical Review B*, vol. 65, no. 8, p. 081 402, Feb. 8, 2002, Publisher: American Physical Society. DOI: 10.1103/PhysRevB.65.081402 (cit. on p. 98).

[184] A. Loubat, S. Béchu, M. Bouttemy, J. Vigneron, D. Lincot, J.-F. Guillemoles, and A. Etcheberry, "Cu depletion on $Cu(In,Ga)Se_2$ surfaces investigated by chemical engineering: An x-ray photoelectron spectroscopy approach," *Journal of Vacuum Science and Technology A*, vol. 37, no. 4, Jul. 2019. DOI: 10.1116/1.5097353 (cit. on p. 98).

[185] R. E. Honig, *Vapor pressure data for the solid and liquid elements,* RCA Laboratories, David Sarnoff Research Center, Jan. 1, 1969 (cit. on p. 104).

[186] R. Saniz, J. Bekaert, B. Partoens, and D. Lamoen, "Structural and electronic properties of defects at grain boundaries in $CuInSe_2$," *Physical Chemistry Chemical Physics*, vol. 19, no. 22, pp. 14 770–14 780, Jun. 7, 2017, Publisher: The Royal Society of Chemistry. DOI: 10.1039/C7CP02033C (cit. on p. 115).

[187] C. S. Fuller, K. B. Wolfstirn, and H. W. Allison, "Defects in GaAs produced by copper," *Applied Physics Letters*, vol. 4, no. 3, pp. 48–49, Feb. 1964, Publisher: American Institute of Physics. DOI: 10.1063/1.1753957 (cit. on p. 117).

[188] G. Greczynski and L. Hultman, "X-ray photoelectron spectroscopy: Towards reliable binding energy referencing," *Progress in Materials Science*, vol. 107,

p. 100 591, Jan. 1, 2020. DOI: 10.1016/j.pmatsci.2019.100591 (cit. on pp. 117, 129).

[189] D. R. Baer, K. Artyushkova, H. Cohen, C. D. Easton, M. Engelhard, T. R. Gengenbach, G. Greczynski, P. Mack, D. J. Morgan, and A. Roberts, "XPS guide: Charge neutralization and binding energy referencing for insulating samples," *Journal of Vacuum Science & Technology A*, vol. 38, no. 3, p. 031 204, May 2020, Publisher: American Vacuum Society. DOI: 10.1116/6.0000057 (cit. on pp. 117, 129).

[190] W. M. Lau, "Use of surface charging in x-ray photoelectron spectroscopic studies of ultrathin dielectric films on semiconductors," *Applied Physics Letters*, vol. 54, no. 4, pp. 338–340, Jan. 23, 1989, Publisher: American Institute of Physics. DOI: 10.1063/1.101450 (cit. on pp. 117, 129).

[191] I. Doron-Mor, A. Hatzor, A. Vaskevich, T. van der Boom-Moav, A. Shanzer, I. Rubinstein, and H. Cohen, "Controlled surface charging as a depth-profiling probe for mesoscopic layers," *Nature*, vol. 406, no. 6794, pp. 382–385, Jul. 2000, Number: 6794 Publisher: Nature Publishing Group. DOI: 10.1038/35019025 (cit. on pp. 117, 129).

[192] C. Xue, D. Papadimitriou, Y. S. Raptis, W. Richter, N. Esser, S. Siebentritt, and M. C. Lux-Steiner, "Micro-raman study of orientation effects of Cu_xSe-crystallites on Cu-rich $CuGaSe_2$ thin films," *Journal of Applied Physics*, vol. 96, no. 4, pp. 1963–1966, Aug. 15, 2004, Publisher: American Institute of Physics. DOI: 10.1063/1.1772885 (cit. on p. 133).

[193] S. M. Peiris, T. T. Pearson, and D. L. Heinz, "Compression of klockmannite, CuSe," *The Journal of Chemical Physics*, vol. 109, no. 2, pp. 634–636, Jul. 8, 1998, Publisher: American Institute of Physics. DOI: 10.1063/1.476601 (cit. on p. 133).